University of Cincinnati

Date: 7/18/2022

I, Peter D Grimm Jr., hereby submit this original work as part of the requirements for the degree of Master of Science in Electrical Engineering.

It is entitled:

Real-time control of radiofrequency thermal ablation using three-dimensional ultrasound echo decorrelation imaging feedback

Student's name: **Peter D Grimm Jr.**

This work and its defense approved by:

Committee chair: T. Douglas Mast, Ph.D.

Committee member: Mehdi Norouzi, Ph.D.

Committee member: Xuefu Zhou, Ph.D.

UNIVERSITY OF
Cincinnati

44235

Real-time control of radiofrequency thermal ablation using three-dimensional ultrasound echo decorrelation imaging feedback

A thesis submitted to the Graduate School of the

University of Cincinnati

in partial fulfillment of the degree of Master of Science

in the

Department of Electrical Engineering and Computing Systems

of the College of Engineering and Applied Science

by

Peter Grimm

Thesis Committee:

T. Douglas Mast, Ph.D. (Committee Chair)

Department of Biomedical Engineering, College of Engineering and Applied Science

Xuefu Zhou, Ph.D.

Department of Electrical Engineering, College of Engineering and Applied Science

Mehdi Norouzi, Ph.D.

Department of Electrical Engineering, College of Engineering and Applied Science

Abstract

Liver cancer is a significant public health burden; as of 2020, it is the second leading cause of cancer-related mortality worldwide. Hepatic resection is considered the gold standard for the treatment of liver malignancies. However, this procedure is only possible in a minority of patients, necessitating treatment modalities with comparatively worse performance, such as thermal ablation. Thermal ablation generally results in poorer clinical outcomes relative to resection, with a higher rate of recurrence and the potential for complications related to damage to healthy tissue near the ablation zone. Medical imaging techniques can improve thermal ablation procedures via assistance in preoperative planning, probe placement and postoperative evaluation, but clinicians lack a method to monitor and control thermal ablation while the procedure is ongoing.

Echo decorrelation imaging is a pulse-echo ultrasound imaging technique that measures stochastic variations in echo signals arising from thermal treatment. The method has been shown to accurately predict thermal lesioning in *in vivo* and *ex vivo* studies of thermal ablation using conventional 2D ultrasound imaging. This thesis aims to apply the echo decorrelation methodology to volumetric ultrasound data to control RFA procedures in real-time. Feedback control is implemented as a bang-bang type controller that automatically stops thermal treatment if the spatial mean of the cumulative decorrelation map exceeds a set threshold.

3D echo decorrelation-based control was evaluated through a series of feedback-controlled and uncontrolled ablation trials on *ex vivo* bovine liver tissue using a clinical RFA system. The RFA system was set to target a 15 mm radius spherical region of tissue while decorrelation maps were computed from captured volumetric ultrasound data; if the control criterion was met, the procedure was automatically stopped using a custom-designed microcontroller circuit. Trials were divided into two groups, a preliminary group, which was used to evaluate the efficacy of the method in predicting local thermal lesioning as well as to inform parameter selection for later trials, and a final group, which was used

to gauge the performance of the method in optimizing the size and geometry of the ablated region.

In our feedback-controlled trials, we found moderately better conformance to the targeted region as measured by the Sorenson-Dice coefficient between the targeted region and sectioned tissue histology. A statistically significant difference in ablated volume was found between the uncontrolled and controlled groups, but no difference was found in the variance of ablated volume or the ablation rate. We found that 3D echo decorrelation imaging performed similarly to 2D echo decorrelation imaging in monitoring and controlling thermal lesioning, despite using a lower frame rate, lower number of samples and forgoing stochastic averaging. Overall, we have demonstrated a feedback control methodology for *ex vivo* radiofrequency ablation using 3D ultrasound echo decorrelation imaging that resulted in better conformance to our desired ablation region. This result shows promise for the utility of echo decorrelation imaging in optimizing thermal ablation procedures, which could potentially result in better clinical outcomes for patients with liver cancer.

Acknowledgements

I want to thank the faculty at the University of Cincinnati for their support in the research and creation of this thesis. I deeply appreciate the support, knowledge and patience of my advisor Dr. T. Douglas Mast, who sacrificed a great deal to assist me throughout the years on this project. He tirelessly supported my research despite the many setbacks and frustrations, and I could not be thankful enough. I'd also like to thank my colleagues at the Biomedical Acoustics Laboratory, Elmira Ghahramani, Sunethra Dayavansha, Bahar Saremi and Michael Swearengen, for their invaluable help in bringing this research to fruition and in making the lab a wonderful and inviting place. I am also grateful for the assistance of Dr. Marepalli Rao for graciously lending his time and statistics expertise to the project.

I also could not have done this without the time and support of Dr. Vasant Salgaonkar and the engineers at Siemens ultrasound, whose advice and technical assistance were crucial to the implementation of this research.

Additionally, I could not have done it without the support of my parents and siblings, all of whom supported me through thick and thin through this entire process. Even through my lowest points, they were always unconditionally supportive.

Contents

List of Figures

List of Tables

List of Abbreviations

AASLD American Association for the Study and Treatment of Liver Disease. 17

ADT Arterially directed therapies. 18

AUC Area under the curve. 59

BCLC Barcelona clinic liver cancer. 5, 17, 18

CA Chemical ablation. 18

GUI Graphical user interface. 43

HCC Hepatocellular carcinoma. 15

HIFU High-intensity focused ultrasound. 19, 21

HR Hepatic resection. 17

IQ In-phase and quadrature. 40

LT Liver transplantation. 17

LUT Look up table. 49

MWA Microwave ablation. 19

NCCN National Comprehensive Cancer Network. 17

OS Overall survival. 17

PBS Phosphate-buffered saline. 50

PLA Polylactic acid. 50

RFA Radiofrequency ablation. 19

ROI Region of interest. 32

TA Thermal ablation. 18

TACE Transarterial chemoembolization. 18

TARE Transarterial radioembolization. 18

XOR Exclusive or. 49

Chapter I

Introduction

1.1 Background

1.1.1 Clinical background

In 2020, an estimated 905,677 patients were diagnosed with primary liver cancer, and 830,180 deaths were attributed to the disease worldwide, making it the second leading cause of cancer-related mortality [1]. The high human toll is in large part due to liver cancer's mortality rate; the estimated combined 5-year survival rate for all stages in the united states is 18%, the second lowest behind only pancreatic cancer [2]. Hepatocellular carcinoma (HCC) is the most common primary liver cancer, accounting for an estimated 75% of diagnoses in 2020 [2]. Epidemiologically, the causes of HCC are multifaceted, with primary risk factors varying by region and population group. In developing nations, the foremost risk factors are hepatitis B (HBV), hepatitis C (HCV), and aflatoxin exposure, while in developed nations, these factors have been largely mitigated by wide-scale vaccination and strict food safety laws [3, 4]. In these countries, the development of HCC is primarily associated with obesity, alcoholism, and type 2 diabetes, while less common risk factors include hemophilia, non-alcoholic fatty liver disease, hemochromatosis, and congenital diseases such as Alpha 1-antitrypsin deficiency and Wilson's disease [3, 5–7]. Recent projections based on epidemiological models of these risk factors, particularly obesity and type 2 diabetes, have suggested that the overall incidence of liver cancer will increase by 2030 [8]. Even with global efforts for more equitable distribution of hepatitis

vaccinations, the rise in obesity- and type 2 diabetes-mediated liver cancer diagnoses are expected to outpace these mitigation efforts in developing nations [8]. Additionally, the liver is a frequent site for metastasis of other cancers, which is associated with significantly worse clinical outcomes and higher rates of recurrence, particularly when originating from the lungs, pancreas, colon or stomach [9].

Prognosis and treatment methods vary widely by the stage at which the disease is diagnosed, with early detection being the most substantial predictor of long-term survival [5, 6, 10]. Unfortunately, early-stage liver cancer is often symptomatically indistinguishable from generalized chronic liver disease, resulting in most patients going undiagnosed until the disease has progressed [7, 10]. Curative treatment approaches, such as hepatic resection (HR), liver transplantation (LT), and thermal ablation (TA) are often only available in early-stage cases, while systemic chemotherapy and palliative care are typically the only treatment options available for late-stage disease with metastasization [5, 6]. Chemotherapy often results in a relatively limited prolongation of life, with the standard first-line treatments such as Sorafenib, Lenvatinib and Nivolumab only providing an additional three months for the patient while also causing debilitating side effects [7]. As later-stage disease is nearly always fatal, screening, early intervention, and improvement in treatment methodologies for early-stage disease are essential for effective treatment of HCC and metastatic liver disease [7]. There are numerous treatment methodologies in current clinical use for patients diagnosed in earlier stages of the disease; these will be discussed in the following section.

1.2   Current liver cancer treatment approaches

1.2.1   Clinical standards

Results from a meta-analysis of liver cancer treatment modalities completed by Tan et al. in 2018 suggested that hepatic resection (HR) offers superior clinical outcomes when compared to percutaneous ablation procedures such as thermal ablation and chemical ablation [11]. Studies have found that in patients satisfying the Milan criteria ($\leq$ 3 lesions,

≤ 3 cm each or a single lesion ≤ 5 cm [12]) the overall survival (OS) rate for patients undergoing HR is between 60–70% [7]. By contrast, percutaneous ablation procedures have an OS rate between 38–60% depending on treatment method [7]. These are both generally inferior to liver transplantation (LT) which has an OS rate of 65–78%, but due to the finite availability of donor organs, this treatment approach is often limited to patients with comorbid liver cirrhosis or later-stage disease without metastasization, for whom LT is the only curative approach [7]. This analysis is reflected in authoritative clinical recommendations for the treatment of liver cancer, such as those published by the American Association for the Study and Treatment of Liver Disease (AASLD) [6] and the National Comprehensive Cancer Network (NCCN) [5], both of which conditionally recommend hepatic resection over ablative procedures in patients where it is applicable. A diagram detailing recommended treatment courses given Barcelona Clinic Liver Cancer (BCLC) stage can be seen in figure 1.1. Unfortunately, despite being the
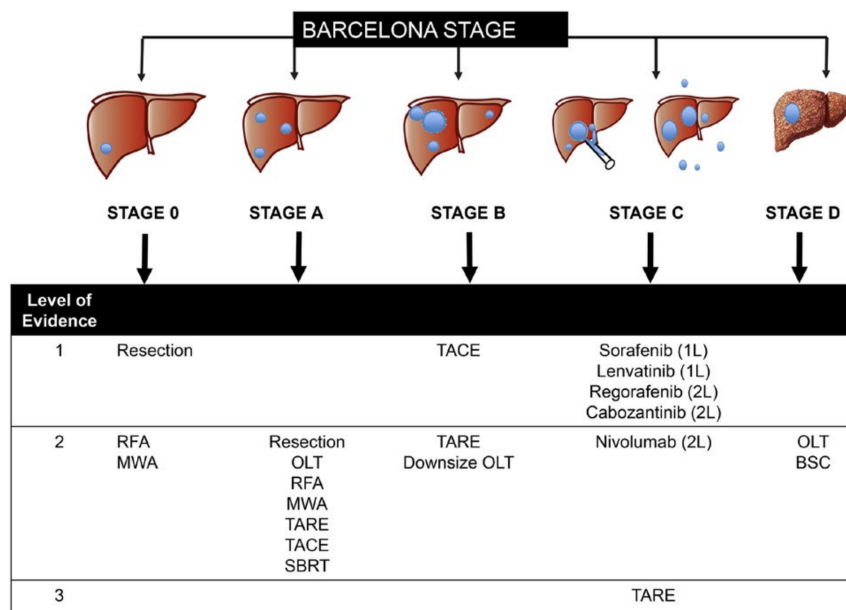
Figure 1.1: Diagram of treatment guidelines provided by Heimblech et al. for clinical recommendations published by AASLD per BCLC stage 0-D, with rows 1, 2 and 3 representing first-line, second-line, and third-line treatment respectively [6].

recommended first-line treatment, as many as 70% of patients are ineligible for hepatic resection [13]. Exclusionary criteria for HR include general systemic risks for invasive surgery, anatomical features of the tumor itself, and insufficient hepatic reserves [14, 15].

For patients with early stage disease (BCLC 0–A) who are ineligible for surgical resection there are numerous locoregional treatments in current use; including thermal ablation (TA), chemical ablation (CA) and arterially directed therapies (ADT). Of these, thermal ablation has become the *de facto* standard for treatment of early stage disease, replacing older methodologies such as chemical ablation in general clinical practice [16, 17]. Arterially direct therapies, such as transarterial radioembolization (TARE) and transarterial chemoembolization (TACE) are generally recommended for patients with intermediate stage disease (BCLC stage B-C) [6, 7, 10] or in combination with thermal ablation for early stage disease (BCLC A) [7, 18]. As the procedure is indicated for later stage disease, it is intended to prolong survival while waiting for a suitable donor, rather than to be curative in itself [7].

1.2.2 Thermal ablation

Thermal ablation is the clinical standard for early-stage primary liver cancer in patients who are ineligible for hepatic resection [6, 7]. The principal of operation in all thermal ablation procedures is to apply a *thermal dose* to the afflicted tissue in order to raise its temperature above 60°, inducing coagulative necrosis within a targeted region [19]. Thermal energy can be delivered via radiofrequency electric current as in radiofrequency ablation (RFA) [20], microwave electromagnetic radiation as in microwave ablation (MWA) [21], or acoustic waves as in high intensity focused ultrasound ablation (HIFU) [7]. In cases where the tumor is < 2 cm in diameter, ablation has similar efficacy to HR [13, 22], but in the general case ablation has a higher recurrence rate, as well as the potential for additional complications from damage to surrounding healthy tissue [7, 11, 13, 22, 23].

To ensure full treatment, physicians are advised to ablate a margin of 2–5 mm around the tumor [24]. This margin then serves as the clinical target for evaluation of treatment efficacy [25]. Although a large margin can substantially decrease the odds of recurrence, it is also associated with an increased risk of serious complications [25]. For cases where the tumor's location precludes hepatic resection, it is especially pertinent that these tumors

are accurately ablated, with minimal damage to surrounding tissue, while also ensuring full necrosis of the diseased tissue [13, 25–27].

1.2.2.a Radiofrequency ablation

Radiofrequency ablation accounts for the bulk of thermal ablation procedures in the United States and worldwide [7]. The principle of operation in RFA consists of passing radiofrequency AC electric current (400–500 kHz) from a needle inserted directly into the tumor to a dispersive grounding pad situated on the skin of the patient [11]. The resultant electric field agitates ions at the frequency of the applied potential, transducing electrical energy into heat via friction [20]. As the field lines disperse widely through the tissue, thermal lesioning is limited to a small, roughly spherical region near the needle tip [20]. Electrical conductivity is the primary limiting factor for lesion size, which is further compounded by the formation of 'charred' high electrical impedance regions of ablated tissue [19]. Tissue vaporization, coagulation, and vascular perfusion-induced heat sinks also affect electrical and thermal conductivity, resulting in highly non-linear heat propagation characteristics [11, 20, 28]. Larger lesions can be achieved with saline infusion, which regularizes ion concentration and cools the tissue to prevent charring-induced impedance spikes, and by using multiple electrodes [13, 29].

RFA has a comparatively poor survival rate when compared to HR, with a 5-year OS rate between 39.9–68.5% [7], and tumor recurrence occurring in 15–20% of patients [13, 30]. Recurrence is strongly associated with overall tumor size and proximity to surrounding vital anatomical features [13]. A study by Ayav et al. found that the best predictor for recurrence in ablation procedures is a tumor size > 3 cm, which they posited was due to the high heterogeneity of the tumor causing uneven treatment throughout the ablation zone [13, 29]. RFA is generally recognized as a low-risk procedure, but complications can include damage to adjacent organs, liver failure, cancer seeding and peritoneal hemorrhaging in a minority of patients [27]. Complications related to inaccurate treatment and ablation of healthy tissue can result in significantly worsened clinical outcomes [27, 31],

with a strong correlation between ischemic complications as a result of overtreatment and patient mortality [26].

1.2.2.b Microwave ablation

Microwave ablation (MWA) is an increasingly popular alternative to RFA and is indicated for the same stage and manifestations of the disease (ineligible for hepatic resection, tumor size < 5 cm) [7]. In MWA, tissue is heated via microwave-frequency (900–2450 MHz) electromagnetic radiation emitted from a dipole antenna placed within the targeted tumor. Dipole molecules, primarily water, oscillate at the applied frequency, heating tissue via friction in a manner similar to RFA [21]. MWA is less dependent on local tissue conductivity than RFA and, as such, is not as affected by vaporization-induced changes in tissue impedance, allowing for greater power delivery and thus shorter ablation times [32]. Additionally, MWA is less susceptible to undesired cooling from local arterial perfusion [11, 21, 32]. MWA has been found to perform similarly to RFA in clinical practice, with a comparable 5-years OS rate of 43.1–60% [7]. A meta-analysis by Tan *et al.* did not find a statistically significant difference in clinical outcomes or incidence of complications between the two methods [11] and concluded there was no substantial evidence for the superiority of MWA over RFA. Despite its seemingly negligible improvements in treatment outcomes compared with RFA, MWA has become a popular modality among physicians due to lower procedure times, and perceived improvements in ablation accuracy [7, 12].

1.2.2.c High intensity focused ultrasound ablation

High intensity focused ultrasound (HIFU) ablation utilizes focused acoustic energy to induce coagulative necrosis at a precise focal depth [20]. Unlike percutaneous ablation methods such as RFA or MWA, HIFU can deliver a thermal dose to a targeted region without direct contact. This offers clear benefits in reducing the risk of complications from a surgical incision, such as tumor seeding [33]. Despite the many benefits offered by a minimally invasive procedure, HIFU adoption has been relatively slow in the United

States [34]. However, HIFU ablation is a very active area of research and is being studied for the treatment of liver [35], breast [36], pancreatic [37], prostate [38, 39] and brain cancer [40].

1.2.2.d   Combination therapies

Combination therapies of ablative procedures with TACE and TARE have been proposed to address the shortcomings of either method. The techniques can be administered concurrently to compensate for heat loss due to perfusion-mediated tissue cooling or sequentially to ensure complete treatment of potentially unablated tissue [41, 42]. This combination has shown promising results in some clinical studies and meta-analyses, with some reporting significant improvements from combination HIFU-TACE therapy [43], RFA-TACE therapy [44, 45] and MWA-TACE therapy. but this increase in efficacy is limited to more severe disease with > 5 cm tumors, which is consistent with the clinical recommendation for TARE/TACE alone [46].

1.2.3   Clinical need: monitoring and control of thermal ablation procedures

Thermal ablation procedures are considered a second-line treatment modality due to comparatively poor performance relative to hepatic resection in both metastatic [47] and primary cases [7, 11] of liver cancer. Despite being the first-line treatment, HR is only applicable in 20–30% of patients, necessitating the application of treatment modalities with relatively poor performance, such as thermal ablation [7]. This poor performance can be attributed to a lack of precise targeting of cancerous tissue relative to the precision of surgical resection [13, 30]. Inaccurate targeting has two potential adverse effects: cancer recurrence if the tissue is undertreated and damage to vital, healthy tissue if the tumor is overtreated. Recurrence as a result of undertreatment occurs in 15–20% of patients [13, 30] and will require additional rounds of therapy to assure long-term disease-free survival. Overtreatment can worsen clinical outcomes through damage to vital supportive tissue, such as the hepatic artery or portal vein [13]. Therefore, a method that can improve the

accuracy of thermal ablation procedures to be closer to the precision of clinical resection could reduce the incidence of complications arising from tumor overtreatment and undertreatment [48].

1.3   Image guided thermal ablation

The standard operating procedure for thermal ablation involves medical imaging technologies for localization of malignancies, probe placement and postoperative evaluation of the ablated region [49]. This can be done with magnetic resonance (MR), computed tomography (CT) [50, 51], and/or ultrasound (US) [49] based imaging methods. MR [47] and CT [51] can generate high-resolution scans delineating tumor boundaries more consistently than US alone, but face numerous practical limitations for use in real-time targeting of cancerous tissue. Exposure to ionizing radiation limits the continual use of CT, and the need for highly specialized non-magnetic equipment limits MR [47]. Thus these modalities are generally limited to pre- and postoperative imaging, where they are used to determine the volume and location of a tumor and thermal lesion, respectively [51]. Probe placement is typically guided by B-mode ultrasound imaging with reference to the images generated by CT and MR [25].

Notably, standard clinical methods are almost entirely limited to post- and preoperative evaluation of tumor margins, with no way of verifying complete ablation during the procedure. Clinicians thus cannot stop the procedure early to minimize lesioning of healthy tissue, nor can they continue an incomplete ablation without first viewing medical images taken after the procedure. A real-time imaging modality that can inform clinicians of the status of the targeted tumor could thus minimize the need for additional procedures and minimize the amount of ablated healthy tissue.

1.3.1   Real-time monitoring and control of RFA

Numerous real-time imaging techniques have been proposed for improving tissue targeting in thermal ablation procedures, including magnetic resonance imaging (MRI)

[52–54] and ultrasound-based (US) [55, 56] methods. As ablation procedures already feature one or more imaging modalities for tumor localization and lesioning evaluation, real-time monitoring methods would not add a high degree of complexity to existing clinical standards.

MR is capable of accurately predicting thermal lesioning in real-time via T1 [57, 58], T2 [59, 60] and proton resonance frequency [61, 62] based thermometric methods. MR monitoring of RFA and MWA has been found to offer promising performance in predicting necrotic lesions and incomplete tumor ablation in some clinical studies [59, 63]. MR monitoring of HIFU has seen particularly well studied [64], and is becoming more common in clinical practice. However, MR devices are costly, non-portable, require extensive training and can only be used in conjunction with specialized non-magnetic tools [7].

In contrast with MR, ultrasound imaging is portable, inexpensive, and can be used with standard equipment [7]. Thermal lesioning results in measurable changes in the acoustic properties of tissue such as the elastic modulus [65] and attenuation coefficient [66, 67], as such these quantities can be measured to estimate local tissue necrosis. Proposed methods include echo-strain imaging [68], integrated backscatter mapping [69], attenuation imaging [66, 67], elastography [65], radiation-force elasticity [70], block-matching [71], and harmonic motion imaging [55, 72]. Many of these methods rely on cross-correlation of adjacent echo-frames for computation, which can be distorted by stochastic variation in echo signals arising from structural deformation, shadowing from bubbles and changes in blood flow. Broadly, these effects can be described as 'echo signal decorrelation'.

The underlying physical mechanisms of echo-signal decorrelation were analyzed by Hooi *et al.* [73] who found that decorrelation arose out of intrinsic structural changes as well as noise- and motion-induced artifacts. Local tissue heating affects the strain of the scattering medium through thermal expansion or changes in the speed of sound, causing decoherence between successive pulse-echo signals [73]. Additionally, tissue vaporization above 100 °C results in transient bubble activity within the heated tissue, causing rapid

random motion that is detectable in echo signals [74]. Echo signal decorrelation is the basis of the echo decorrelation imaging technique, as will be discussed in the next chapter.

1.4   3D ultrasound imaging

Real-time volumetric ultrasound imaging has become practical in recent years as a result of advances in piezoelectric material manufacturing, and efficient parallel computing devices [75]. Matrix array transducers are state-of-the-art in volumetric ultrasound imaging, offering far superior volume rates compared to previous methods based on mechanical motion of conventional 2D linear arrays [75]. Matrix arrays utilize a 2D grid of imaging elements cut from a single piezoelectric crystal, each of which is capable of transmission and reception of pulsed ultrasound signals [76, 77]. The principle of operation of matrix arrays is similar to linear phased arrays; a phased pulse is applied to each individually addressable grid element, and the received echos are beam-formed into a composite image [76]. In linear phased arrays, beam steering is limited to the azimuthal imaging plane. In contrast, a matrix array can steer along the azimuthal imaging plane and the orthogonal elevational imaging plane, enabling the acquisition of true real-time 3D pulse-echo volumes. These devices have found use in fetal imaging [78], renal monitoring [79] and breast cancer screening [48] among other applications [75].

As mentioned in section 1.2, the clinical benchmark used for evaluation of thermal lesioning is the 3D margin enclosing the tumor [23]. Previously, a 2D linear array was limited to evaluating a single plane and could not track the entire margin. With matrix arrays, it becomes possible to image the full ablation zone at volume rates high enough for real-time imaging. Thus, if an accurate method of determining thermal lesioning with ultrasound imaging can be established, true real-time prediction of the total ablation margin is possible.

Chapter II

Echo decorrelation imaging

2.0.1 Introduction

Previous ultrasound-based monitoring and control methods were found to be hampered by the phenomenon of local echo signal decorrelation around the region of interest, limiting the accuracy of estimated tissue properties such as the elastic modulus and attenuation coefficient [80]. While these ultrasound methods can often accurately measure changes in tissue elasticity due to thermal lesioning, their accuracy during the procedure is greatly limited. However, since local decorrelation occurs consistently in areas of thermal activity, this limitation could be repurposed into a predictor of local thermal lesioning.

Echo decorrelation imaging is a pulse-echo ultrasound imaging technique that spatially maps millisecond-timescale echo-signal decorrelation due to thermal lesioning. The method provides a computationally inexpensive method of measuring local spectral decoherence in the scattering medium and, accordingly, changes in tissue arising from thermal lesioning. The theory behind echo decorrelation and previous work related to its use in both real-time monitoring and control of thermal ablation procedures will be explored in this chapter.

2.0.1.a Theory

Let $I(\mathbf{r}, t)$ be a complex beamformed pulse-echo frame (Hilbert transformed analytic or in-phase/quadrature demodulated) recorded at time t, where $\mathbf{r}$ is a coordinate vector

in Cartesian space. Let $I(\mathbf{r}, t + \tau)$ be a second frame recorded at time $t + \tau$, where τ is the inter-frame time. The spatially windowed zero-lag cross-correlation between the two frames is computed as

$$R_{01}(\mathbf{r}) = \langle I(\mathbf{r}, t) \cdot I(\mathbf{r}, t + \tau)^* \rangle \tag{2.1}$$

where * denotes complex conjugation and $\langle \cdot \rangle$ is windowed spatial integration. Spatial integration over a finite window is equivalent to convolution of the frame with the windowing function, defined as follows:

$$\langle I(\mathbf{r}, t) \rangle = \int_{\mathcal{S}} w(\mathbf{r} - \mathbf{r}') I(\mathbf{r}, t) \mathbf{dr}' = I(\mathbf{r}, t) * w \tag{2.2}$$

where w is the windowing function and $\mathcal{S}$ is the coordinate space of the echo frame over which the quantity is integrated. This allows for efficient computation of decorrelation maps using FIR filter- or FFT-based convolution, which is necessary for use in real-time imaging.

The windowed zero-lag autocorrelation of each frame is computed similarly,

$$R_{00}(\mathbf{r}) = \langle |I(\mathbf{r}, t)|^2 \rangle$$
$$R_{11}(\mathbf{r}) = \langle |I(\mathbf{r}, t + \tau)|^2 \rangle \tag{2.3}$$

and can be regarded as a smoothed map of local backscatter energy magnitudes for each echo frame [74]. The elementwise geometric mean of the autocorrelation functions is then defined as the *integrated backscatter map*, $\beta(\mathbf{r})$

$$\beta(\mathbf{r}) = \sqrt{R_{11} \cdot R_{00}} \tag{2.4}$$

which is an approximation of local tissue backscatter energy between the two frames.

A simplified *locally normalized decorrelation* [81] map can be defined as the normalized correlation coefficient between the echo frames subtracted from unity [73]

$$\Delta(\mathbf{r})_{\text{local}} = 1 - \frac{|R_{01}(\mathbf{r})|^2}{|R_{11}(\mathbf{r})| \cdot |R_{00}(\mathbf{r})|} = 1 - \frac{|R_{01}(\mathbf{r})|^2}{\beta^2(\mathbf{r})} \tag{2.5}$$

12

Hooi *et al.* demonstrated that this expression is an approximation of local spectral decoherence in the scattering medium. As such, echo decorrelation imaging provides a computationally inexpensive method of measuring changes in the scattering medium induced by thermal lesioning

Mast *et al.* proposed normalization by the spatial average of backscattered energies, $\overline{R_{00}}$, to account for artifactual decorrelation in regions of both high and low echogenicity [74]. The quantity is then divided by the interframe time to account for greater variation within a larger time window. The final decorrelation map as used in this study was defined by Subramanian *et al.* [82] as

$$\Delta(\mathbf{r}) = 2 \cdot \left[\frac{\beta^2(\mathbf{r}) - |R_{01}(\mathbf{r})|^2}{\tau \cdot [\beta^2(\mathbf{r}) + \overline{\beta^2}]} \right] \tag{2.6}$$

where the term $\overline{\beta^2}$ is the spatial mean of the integrated backscatter map over the entire echo-frame. This is used in place of normalization by $\overline{R_{00}}$ to account for the backscatter energies of both echo-frames.

In the decorrelation formula, the term in the numerator $\beta^2(x, y, z, t) - |R_{01}^2(x, y, z, t)|$ measures transient heat-induced changes in the pulse-echo frame at each voxel, such that at regions where the signal has diverged decorrelation is larger, and in regions where the signal is similar, decorrelation is smaller. An illustration of decorrelation on a single scan line can be seen in figure 2.1. To account for stochastic variation within a given adjacent pair of echo-frames, instantaneous decorrelation maps can be computed from an ensemble average of multiple echo-frame pairs. Ensemble averaged instantaneous decorrelation, $\overline{\Delta}(\mathbf{r}, t)$, is computed as

$$\overline{\Delta}(\mathbf{r}, t) = \frac{1}{K-1} \sum_{k=1}^{K-1} \Delta(\mathbf{r}, k\tau) \tag{2.7}$$

where K is the number of frames over which the ensemble average is computed and k is the index of each frame.

Numerical analysis of the effect of ensemble averaging was completed by Cox *et al.*, who found that RMS error between echo decorrelation imaging and scatterer reflectivity
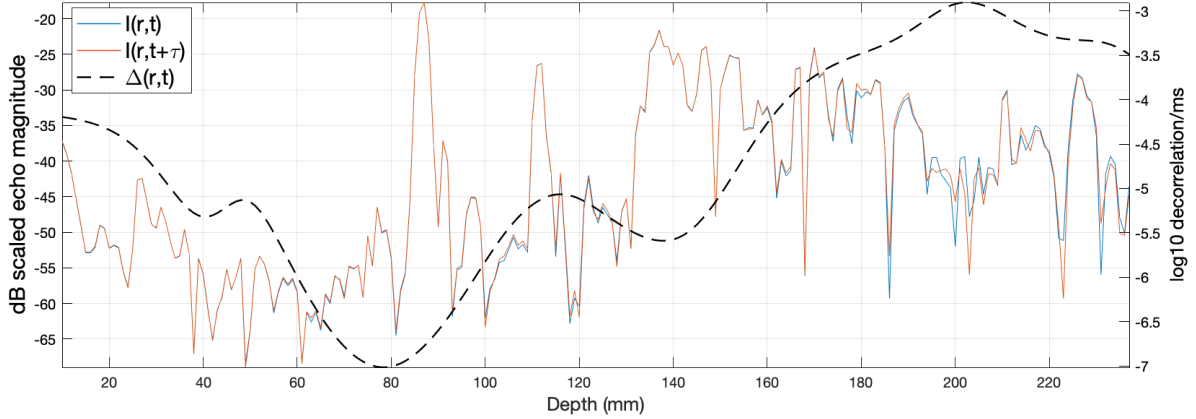
Figure 2.1: Example of locally and globally normalized echo decorrelation on a single scan line. The solid red and blue lines represent two sequential dB scaled I/Q scan line magnitudes at times t and $t + \tau$ imaging to a depth of 255 mm. The dotted black line is echo decorrelation per millisecond. Decorrelation increases as the echo signals diverge, reaching a maximum at approximately 205 mm where the two signals have diverged to the greatest degree within the Gaussian window ($\sigma = 3$ mm).

decoherence was proportional to $1/\sqrt{N}$ for small windows, where N is the number of ensemble-averaged frames [83]. As such, ensemble averaging can significantly reduce the effect of random variation on echo decorrelation maps. Using a larger spatial window also improves resilience to stochastic variation. For 3D echo decorrelation, where the large size of the data limits ensemble averaging, a larger window can be used to account for stochastic variation. This comes at the cost of spatial resolution, as windowing will introduce statistical dependence to the computed echo decorrelation maps. This will be discussed further in section 3.2.3.d.

2.0.1.b   Thermal ablation monitoring using echo-decorrelation imaging

Monitoring of thermal ablation procedures is accomplished via computation of a cumulative echo-decorrelation map from a series of instantaneous echo-decorrelation maps. B-mode images are captured at a set interval and their instantaneous decorrelation is computed from equation 2.6 and ensemble averaged as defined in equation 2.7. The cumulative map is then computed as the element-wise maximum of all instantaneous decorrelation maps

$$\Delta_{\text{cum}}(\mathbf{r}) = \max(\Delta(\mathbf{r}, 0), \Delta(\mathbf{r}, 1), ..., \Delta(\mathbf{r}, N)) \tag{2.8}$$

14

where N is the number of instantaneous decorrelation maps computed thus far and n is the index of the instantaneous decorrelation map.

This cumulative maximum echo decorrelation map is hypothesized to measure the total heat-induced echo signal decorrelation at a given voxel, giving an estimate of local tissue necrosis due to thermal treatment. Multiple studies have shown that decorrelation mapping offers better predictive power for measurement of thermal lesioning than backscatter mapping [74, 82, 84, 85].

2.0.1.c   Noise and motion compensation

A procedure developed by Hooi *et al* [73] can be used to isolate thermally induced signal decorrelation from artifactual decorrelation arising from motion and noise. Total decorrelation is modeled as a linear combination

$$\Delta(\mathbf{r}, t) \approx 1 - \rho(\mathbf{r}, t)(1 - \Delta(\mathbf{r}, t)_{\text{artifactual}}) \tag{2.9}$$

where ρ represents the expected contribution of artifactual decorrelation sources as a function of position [73].

The parameter ρ can be estimated by recording a set of echo-frames prior to ablation and computing a sham decorrelation map, Δ_{sham}, from the cumulative decorrelation map generated by those echo-frames. The final derived quantity as used in *in vivo* studies of echo decorrelation by Fosnight et al. [84] and Abbass et al. [86] was

$$\Delta_{\text{corrected}}(\mathbf{r}, t) = \frac{\Delta_{\text{uncorrected}}(\mathbf{r}, \mathbf{t}) - \Delta_{\text{sham}}(\mathbf{r}, \mathbf{t})}{1 - \Delta_{\text{sham}}(\mathbf{r}, \mathbf{t})} \tag{2.10}$$

where $\Delta_{\text{corrected}}$ is the component of decorrelation attributed primarily to changes in the scattering medium and Δ_{sham} is a decorrelation map computed from echo frames recorded prior to ablation.

This method was found to accurately isolate ablation induced decorrelation from other deorrelation sources in studies of *in vivo* ablation of rabbit liver with an implanted

VX2 tumor [84, 87], providing evidence for echo decorrelation's potential utility in a clinical setting.

2.0.2 Echo decorrelation based control

Abbass et al. [85, 87] proposed a real-time closed-loop feedback control method using a scalar control criterion derived from cumulative echo decorrelation maps. The control criterion is updated upon recomputation of cumulative echo decorrelation and compared to a set threshold. If that threshold is exceeded, the treatment is stopped.

In their trials on control in *ex vivo* bovine liver, they captured a set of 20 B-mode images per HIFU sonication cycle. Ensemble averaged decorrelation maps were then computed from the set of of B-mode images and a cumulative decorrelation map was formed. The control parameter, $\hat{\Delta}$, is derived from the cumulative maximum decorrelation map as either the spatial mean of all pixels within a selected region of interest (ROI)

$$\hat{\Delta}_{\text{avg}} = \frac{1}{|\mathcal{R}|} \sum_{\mathbf{r} \in \mathcal{R}} \Delta_{\text{cum}}(\mathbf{r}, n) \tag{2.11}$$

or the minimum pixel value within a ROI

$$\hat{\Delta}_{\text{min}} = \min(\overline{\Delta}(\mathbf{r}, n)), \mathbf{r} \in \mathcal{R} \tag{2.12}$$

where $\mathcal{R}$ denotes the set of pixels within the targeted ROI, and $|\mathcal{R}|$ is the number of pixels within that ROI.

Ablation was stopped if the decorrelation criterion exceeded a predetermined threshold, denoted Δ_{thresh}. The control behavior can be summarized as

$$\begin{cases} \hat{\Delta}(N) < \Delta_{\text{thresh}} & \text{Continue} \\ \hat{\Delta}(N) \geq \Delta_{\text{thresh}} & \text{Stop treatment} \end{cases} \tag{2.13}$$

where the value of the threshold is determined by analyzing decorrelation maps of trials without feedback control. The decorrelation value which resulted in a true positive rate

(specificity) exceeding 90% for prediction of local ablation was one criterion for selection of a control parameter. Further optimization of the control parameter was carried out through analysis of the entire ablated area. Trials were classified into two groups; trials where the targeted ROI was fully ablated and trials where the targeted ROI was not fully ablated. The minimum decorrelation within the ROI in each case was used as a predictor of full ablation of the targeted ROI, and the control parameter was selected to achieve high specificity and reasonable sensitivity for ablation of the full ROI.

In their *ex vivo* trials of this method, it was found that echo decorrelation feedback control improved the ability of echo decorrelation to predict local ablation, but did not result in more uniform lesions [85]. The authors concluded that echo decorrelation imaging-based control showed promise, but was limited by its inability to image the entire ablation margin.

This methodology was then used in a model of *in-vivo* rabbit liver with an induced VX2 tumor. The motion compensation described in section 2.0.1.b was applied to account for motion due to the breath of the anesthetized animal. Feedback-based control was found to perform similarly to the *ex vivo* trials. Little effect was found on the uniformity of the ablated region, but prediction of local ablation was found to be superior in the controlled group [87].

2.0.3   3D echo decorrelation imaging

Previous studies have shown promising results for predicting local tissue ablation with echo decorrelation imaging, but have been limited to a single 2D plane of tissue. This research aims to extend that methodology to 3D, using the now widely available matrix-array probe technology described in Section 1.4.

A study completed in our lab prior to this thesis explored the use of 3D echo decorrelation imaging for monitoring thermal ablation in ex-vivo bovine liver [81]. In this study, *ex vivo* bovine liver was treated using a clinical RFA system while volumetric ultrasound data was recorded using a matrix array probe. The RFA needle was set to ablate a 2 cm diameter region with a maximum delivered power of 150 W, temperature target of

$110\,^{\circ}\mathrm{C}$ and a treatment time at the target temperature of 5 minutes. Echo decorrelation imaging was found to be an effective predictor of local tissue ablation, outperforming backscatter based imaging by a significant margin, as measured by the AUC of the ROC curve (described in more detail in section 3.2.6).

This study also explored alternative normalization schemes. Echo decorrelation maps were computed as described in equation 2.6, referred to as *combined normalization*, in addition to only local normalization (equation 2.5) and only global normalization by the spatial average of integrated backscatter. The performance of global and combined normalization, as measured by the AUC of the ROC curve, was found to be significantly better than local normalization. No significant difference was found between combined and global normalization in this study.

Prediction of total ablation volume was assessed via a procedure based on K-means clustering. Voxels were classified as predicted-ablated and predicted-unablated based on weighted k-means clustering on their decorrelation value and distance from the ablation needle tip. Performance in prediction of local ablation was then evaluated via the RMS error between predicted volumes and segmented tissue histology, as well as the Dice coefficient between predicted-ablated voxels and observed ablated voxels. The results were similar to the results with ROC analysis, with global and combined decorrelation significantly outperforming locally normalized decorrelation and integrated backscatter. Correlation between predicted volume and observed volume was found to be greatest for globally normalized decorrelation ($R^2 = .333$) and least for IBS ($R^2 = .110$).

The overall viability of the method was in line with previous studies, where its performance in measuring local ablation was found to be comparable to 2D echo decorrelation imaging. Notably, this performance was achieved without ensemble averaging and with a significantly lower frame rate (10 FPS) than was used in previous studies. This study provided preliminary evidence for 3D echo decorrelation's viability as a real-time monitoring methodology for thermal ablation procedures.

2.1 Hypothesis and specific aims

2.1.1 Research hypothesis

This research aims to provide an ultrasound imaging-based feedback control scheme for radiofrequency ablation procedures. Such a method could result in improved treatment outcomes for the patient due to reduced damage to healthy tissue while ensuring complete ablation of malignant tissue. The central hypothesis of this research is that 3D echo decorrelation imaging can serve as a suitable control parameter for precisely targeted ablation, improving the regularity of the ablation zone and full ablation of a desired margin.

2.1.2 Specific Aim 1: Evaluation of 3D echo decorrelation as a predictor of thermal lesioning and determination of a control parameter

Before the proposed method of echo decorrelation-based control could be applied, a suitable control parameter needed to be determined. This was accomplished via a set of preliminary trials in ex-vivo bovine liver using a clinical RFA system. Pulse-echo volumes were acquired using a 3D matrix-array probe during the ablation procedure and used to construct a cumulative 3D echo decorrelation map. Ablated bovine liver tissue was then sectioned into azimuth-depth planes and scanned via an optical scanner. The optical scans were then segmented into 2D binary masks and combined into a 3D mask. A viable control parameter was then found from analysis of echo decorrelation's performance as a predictor of local ablation as well as through evaluation of total ablation size and geometry.

2.1.3 Specific Aim 2: Evaluations of three-dimensional echo decorrelation based control in ex-vivo bovine liver

3D echo decorrelation's performance in improving the uniformity and conformance to the targeted ablation zone was evaluated through a set of trials with echo decorrelation feedback control and an 'uncontrolled' set, which only uses the RF generator's temperature control functionality. Ablation trials were carried out with the same RFA system and imaged with a matrix array probe. Uncontrolled trials were carried out identically to the preliminary trials, while controlled trials were automatically halted upon satisfying the control criterion. The relative performance between controlled and uncontrolled trials was then evaluated by comparing total ablation volume, conformance to the desired ablation geometry via the Sorenson-Dice coefficient, and the rate of ablation.

Chapter III

Real time monitoring and control of ex-vivo radiofrequency thermal ablation using echo decorrelation imaging

3.1 Introduction

To use 3D echo decorrelation imaging's favorable performance in the prediction of local tissue necrosis to optimize the size and geometry of the ablated region, a closed-loop feedback control algorithm was designed. This algorithm was based on previous work by Abbass *et al* [85, 87] on control of HIFU ablation using 2D echo-decorrelation imaging described in section 2.0.2, with necessary adaptations for use with volumetric data and RF ablation. Volumetric pulse-echo pairs were acquired as IQ demodulated pulse-echo data via a matrix array probe connected to a clinical ultrasound system. Received volumes were then used to create a 3D cumulative echo decorrelation map, and a scalar control criterion derived from this map was used to control treatment duration via a bang-bang type controller.

Trials were divided into two groups, a preliminary group, which was used to evaluate the efficacy of the method in predicting local thermal lesioning as well as to determine an effective control criterion for feedback-controlled trials, and a final group, which was used to gauge the performance of echo decorrelation feedback control in optimizing the size and geometry of the ablated region. Real-time control required several additional com-

putational optimizations over the monitoring study, where decorrelation was computed entirely post-hoc. It also required the creation of software and hardware to coordinate image acquisition, decorrelation computation, and automatic control of the RF generator. This chapter will outline the materials, methods, and results of our feedback control system.

3.2   Materials and methods

3.2.1   3D echo decorrelation feedback control algorithm

Real-time feedback control using 3D echo decorrelation imaging was implemented via a closed loop feedback control system, where treatment duration was controlled by a bang-bang type controller. Treatment was stopped when the control criterion, derived from the cumulative echo decorrelation map computed from 3D pulse-echo frames acquired throughout the procedure, exceeds a given threshold. Trials were said to have been 'successfully controlled' if the treatment was stopped early due to the control condition being satisfied.

Pulse-echo volume pairs were acquired by a clinical ultrasound system and sent for processing as quickly as the device allowed. Instantaneous decorrelation maps were then computed from the received volume pairs via the definition of echo decorrelation described in section 2.0.2 and formed into a cumulative decorrelation map. After each new echo volume pair was acquired, the cumulative map was updated, and the control parameter was recomputed. If the control criterion exceeded a set threshold, Δ_{thresh}, the treatment was stopped; The process can be summarized as

$$\begin{cases} \hat{\Delta}(N) < \Delta_{\text{thresh}} & \text{Continue} \\ \hat{\Delta}(N) \geq \Delta_{\text{thresh}} & \text{Stop treatment} \end{cases} \tag{3.1}$$

where the control criterion, $\hat{\Delta}$, was chosen as the spatial average of all voxels within a 15 mm spherical ROI centered at the needle tip. This approach is similar to the method

proposed by Abbass *et al* [85], as discussed in in section 2.0.2, with the exception that we chose to only use the average decorrelation feedback criterion. Abbass *et al.* found that the minimum and average based control criteria performed similarly in their trials [85], so it was decided to use only the average-based method.
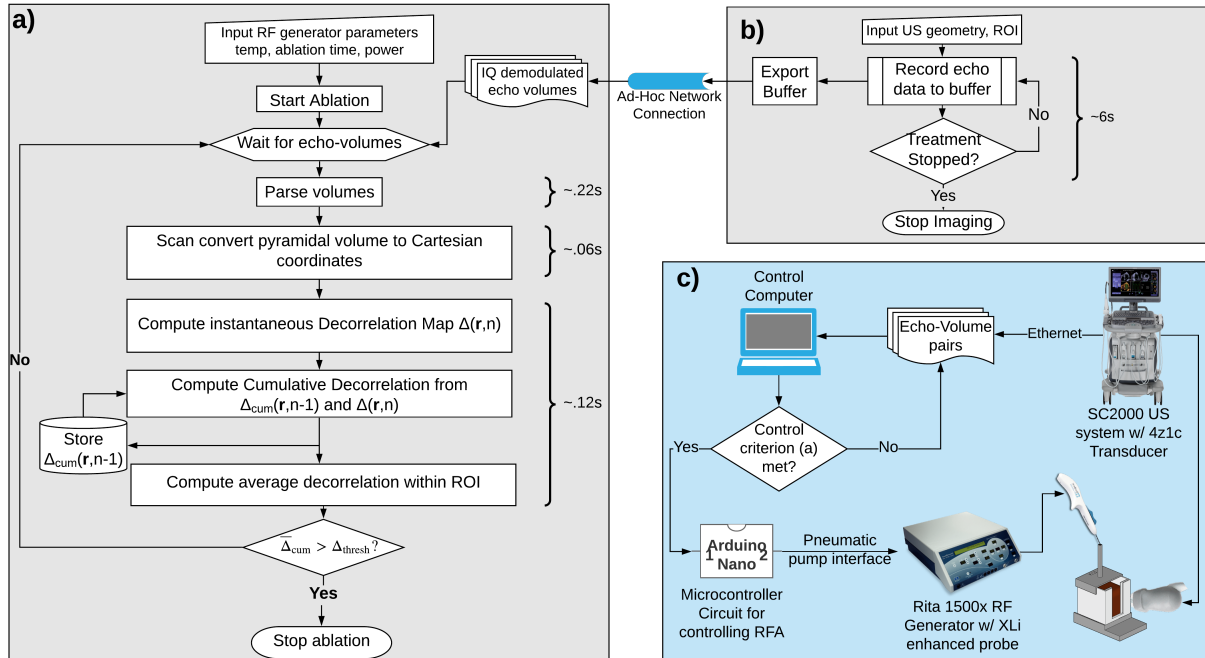
Figure 3.1: Flow chart showing the real-time echo decorrelation feedback control algorithm. Subfigures (a) and (b) show the control algorithm, where the portion marked (a) occurs on the control computer and the portion marked (b) occurs on the ultrasound scanner. Subfigure (c) shows a higher-level view of the setup, illustrating the overall data-flow among the devices used.

A block diagram of the control algorithm and related devices can be seen in Figure 3.1, which shows the main feedback control algorithm in subfigures 3.1a and 3.1b, and a high-level block diagram of the devices used in subfigure 3.1c. The portion running on the scanner, seen in 3.1b, is completed asynchronously with the portion running on the control computer, seen in subfigure 3.1a. Time taken to complete each operation is marked with curly braces. A detailed account of our implementation of this algorithm is given in section 3.2.3.

3.2.2   Image processing

3.2.2.a   Acquisition and scan conversion

Ultrasound pulse-echo volumes were recorded using a Siemens SC2000 imaging system with a 4Z1c matrix array probe (active aperture 19.2×14.4 mm^2; 48×36 elements; bandwidth 1.5–3.5 MHz) as in-phase/quadrature (IQ) demodulated 3D matrices of complex fixed-point numbers in a pyramidal (frustum-like) coordinate system. Datapoints are indexed by their depth along each scan line r, and the angle between the origin xy and xz planes denoted θ (azimuthal) and ϕ (azimuthal), respectively. Scan lines are spaced in equal increments of $\sin(\theta)$ and $\sin(\phi)$. The device was set to use a 2.8 MHz center frequency and 2.5 MHz sampling rate for IQ demodulated echo signals, the lowest spatial resolution allowed by the scanner to maximize temporal resolution.

Imaging depth and scan angles were adjusted throughout the parameter determination process, which will be described in sections 3.2.9 and 3.2.7. Earlier trials used an elevational and azimuthal scan angle range of 78° and a nominal depth of 110 mm (true recorded depths extended to 117 mm). In this mode, the size of the pyramidal space volumes was $376 \times 55 \times 54 \times 2$ ($r \times \theta \times \phi \times$ frames), with a frame rate of 55 VPS and a time-between acquisitions of approximately 16 seconds. For better time resolution, this was reduced to the minimal possible geometry to image our ablation region with additional padding of at minimum 4σ points isotropically around the region to account for edge effects at the boundaries of the frustum. The chosen geometry for the final set of trials was selected as 56° × 56° azimuth and elevation scan angles with a nominal depth of 70 mm (actual volumes extended to 80 mm). Received matrix sizes for this setting were $255 \times 45 \times 42 \times 2$, with a frame rate of 117 VPS and a volume export rate of once every 6 seconds.

Exported volumes were scan converted onto a Cartesian grid of isotropic step size 1 mm using trilinear interpolation. The grid was defined to fully enclose the imaging frustum, where the dimension z is the distance from the origin in the depth direction, and y and x are the distance along the elevational and azimuthal directions centered

24

at the origin. Each point on the Cartesian grid, $\hat{\mathbf{x}}_i$, was sampled and its corresponding location in pyramidal space was determined using the formulae

$$r = \sqrt{x^2 + y^2 + z^2} \tag{3.2}$$

$$\sin(\theta) = \frac{y}{\sqrt{y^2 + z^2}} \tag{3.3}$$

$$\sin(\phi) = \frac{x}{\sqrt{x^2 + z^2}} \tag{3.4}$$

where r is depth, θ is the azimuthal angle and ϕ is the elevational angle.

The location of each Cartesian point, $\mathbf{x}_i$, in pyramidal space was determined ($\hat{\mathbf{r}}_i = (r_i, \theta_i, \phi_i)$) and the closest 8 points in a cubic lattice surrounding the sampled point are weighted by their distance and summed

$$I_{\text{cart}}(\mathbf{x}_i) = \sum_{n=1}^{8} c_n(\mathbf{r}_n, \hat{\mathbf{r}}_i) \cdot I_{\text{pyram}}(\mathbf{r}_n) \tag{3.5}$$

where I_{pyram} is the echo frame in pyramidal coordinates, I_{pyram} is the echo frame in Cartesian coordinates, and c_i is the coefficient of each pyramidal space voxel, determined by its distance from the sampled point $\hat{\mathbf{r}}_i$.

As each point in the 3D grid requires multiple floating-point operations, scan-conversion was implemented as efficient compiled code, described in more detail in section 3.2.3.d.

3.2.2.b   Decorrelation implementation

Echo decorrelation maps were computed via the definition of decorrelation described in section 2.0.1. As discussed in that section, spatially averaged quantities within a window can be computed via convolution, allowing for efficient discrete computation of decorrelation with FIR filtering- or FFT-based methods. We found that spatial frequency domain convolution offered better performance for our particular setup, and as such the convolution operations were completed in the frequency domain.

Explicitly, for each zero-padded correlation term $R[\mathbf{x}]$ in a discrete 3D Cartesian coordinate system

$$\langle R[\mathbf{x}]\rangle = \sum_{\mathbf{x}\in\mathcal{V}} R[\mathbf{x}]\cdot w[\mathbf{x}-\mathbf{x}_0] = R[\mathbf{x}]\circledast w[\mathbf{x}]$$
$$= \mathcal{F}^{-1}\left[\mathcal{F}[R[\mathbf{x}]]\circ\mathcal{F}[w[\mathbf{x}]]\right] \tag{3.6}$$

where $\mathbf{x}$ is the coordinate vector in discrete cartesian space, $\circledast$ is circular convolution, $\circ$ is the elementwise product and w is a 3D Gaussian kernel with width parameter $\sigma = 3$ mm, defined with its Fourier transform pair as

$$w[\mathbf{x}] = \frac{1}{\sigma^3(2\pi)^{\frac{3}{2}}}\cdot\exp\left(-\frac{|\mathbf{x}^2|}{2\sigma^2}\right)\xleftrightarrow{FT}\exp\left(-\frac{\sigma^2|\mathbf{k}^2|}{2}\right) \tag{3.7}$$

where $\mathbf{k}$ corresponds to the frequency bin vector in the 3D spatial frequency domain.

A 3D Gaussian kernel with width parameter $\sigma = 3$ mm was selected for the windowing function as a compromise between spatial resolution of the computed echo decorrelation maps and reduction of the effects of stochastic variation. As we are not using ensemble averaging, we chose a larger smoothing window relative to some previous 2D echo decorrelation studies, which used values in the range of $\sigma =$1–2.5 mm [82, 84, 85]).

Each correlation term R_{01}, R_{00} and R_{11} as defined in equation 2.1 is transformed into the frequency domain using MATLAB's built-in fftn package. They are then pointwise multiplied with the Gaussian window defined in the frequency domain, transformed back to the spatial domain and used in the definition of decorrelation. We found that decorrelation could be computed reasonably quickly on commodity hardware. On the laptop used for our experiments (Dell Precision 5510 with an Intel Core-i7 6820HQ processor) the time to process full decorrelation maps from received raw ultrasound echo frames was approximately 526 ms for the larger echo-volume setting and approximately 9–10 ms for the smaller volume setting.

3.2.3　Software and device interoperation

3.2.3.a　Real-time control software

Controlled trials required intercommunication between the scanner, RF generator and a central-control computer responsible for data processing and coordinating the other devices. For this purpose, a custom-designed MATLAB graphical user interface (GUI) was designed. Computation, file I/O and other processing tasks were carried out by a set of MATLAB classes with a GUI-independent application interface. The interface provided a standard way of accessing data from all devices, which could then be used for real-time computation and post-hoc analysis.

A screenshot of the MATLAB GUI can be seen in figure 3.2. The GUI is divided into three panels, one for setting image and device interoperation parameters, another for real-time operation of the device, and a third for reviewing the results of a given trial. The 'setup panel', shown in subfigure 3.2a, is used to initialize connections between the devices and set parameters for imaging geometry, ROI placement and settings related to device interoperation. To visualize the 3D volumetric ultrasound data and locate important features within the scan converted B-mode volumes, the GUI displays three orthogonal 2D planes of B-mode data, corresponding to the elevation-azimuth, depth-azimuth and depth-elevation planes. A slider can be used to pan through the volume along any of the three orthogonal directions. Additionally, each slice image displays the location of the imaging ROI as a green circle.

The 'imaging panel', shown in Figure 3.2b, is used for real-time monitoring of the B-mode ultrasound data, cumulative decorrelation maps, and RF generator output data during the treatment. The feedback control threshold is entered into a text field and the treatment is started via the 'automatic imaging' subpanel. The GUI displays 3 2D planes of the most recent volumetric ultrasound data, in the same manner as the 'setup panel' with the addition of the current cumulative decorrelation overlaid over the B-mode ultrasound data. A time series plot of log10-scaled cumulative decorrelation within the entire echo volume, as well as the average decorrelation within just the targeted ROI, is

(a) Setup panel
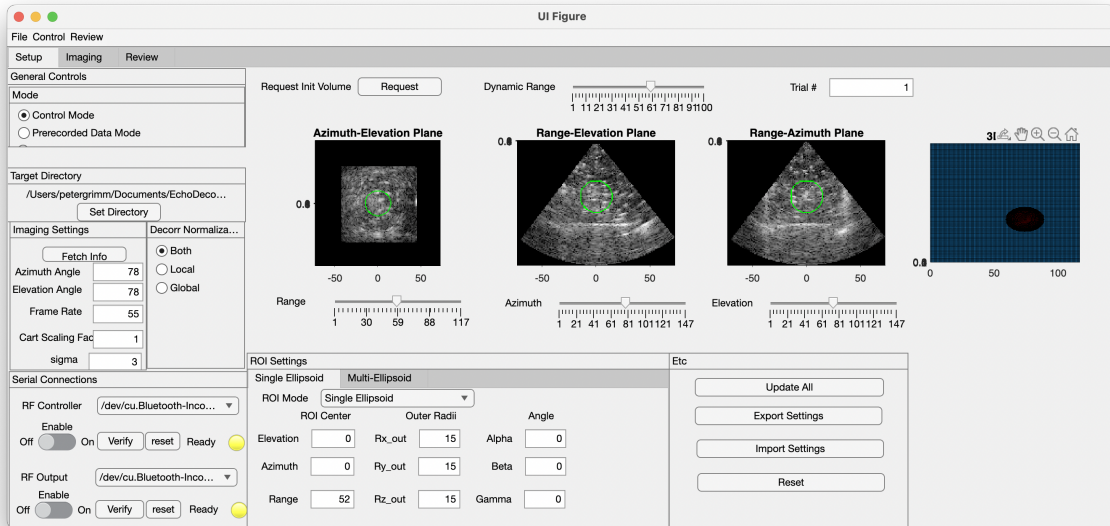
(b) Imaging panel
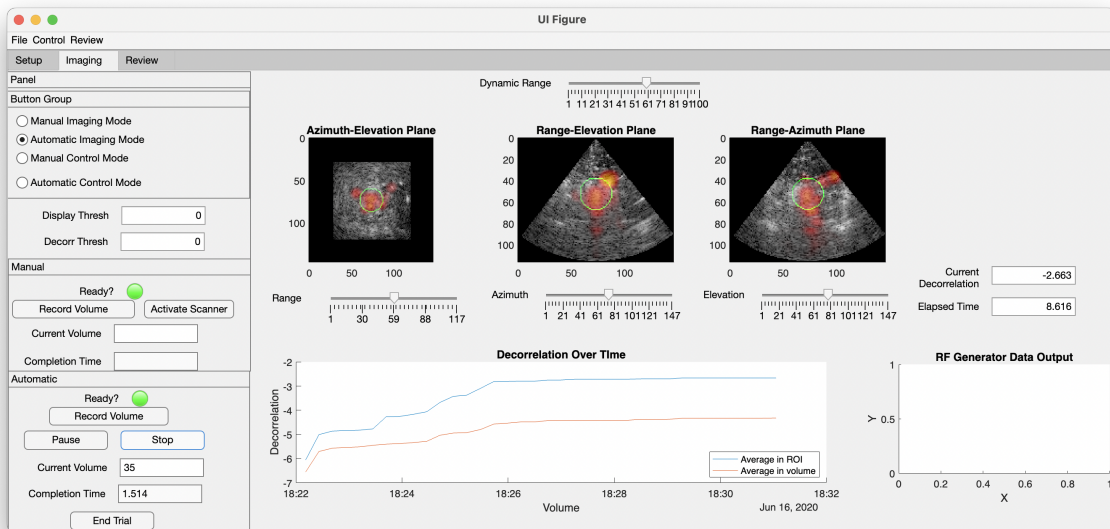
Figure 3.2: Imaging panel of real-time control GUI. This panel is used to set parameters for the ultrasound volume geometry, treatment ROI, device connections and decorrelation maps.

shown in the bottom left plot. The bottom right plot displays the current temperature at the RF needle's thermocouples. A Python script was designed to interface with the scanner's internal imaging system via a network socket originally intended for debugging the device. The script records volumetric ultrasound data to a buffer and exports it to a solid-state drive shared via an ad-hoc wired network connection between the scanner and control laptop. The script then packages the recorded raw data files into folders with a timestamp and metadata file containing geometric parameters of the recorded volume. Validation was also performed on the recorded data, as earlier trials of the device resulted in numerous errors. Particularly, the devices would often hold on to a particular buffer and continuously export the same information. To account for this, a subset of values are taken from each data set in a standard manner and hashed, and each subsequent frame's partial hash is compared to a list of all previous frames to verify correct operation. Other errors were sometimes present in the received ultrasound data, such as the device outputting seemingly random data, which was detected using the control GUI. If present, these volumes were excluded from our analysis.

Upon starting the script, the user is prompted to enter geometry information for the ablation trial and to select a directory from the shared drive on the scanner. The Python script then exports files over the network connection to the control laptop asynchronously. Data is packaged as time-stamped folders containing all necessary image data and geometry information. The MATLAB classes then provide a separate interface for managing the generated data files, scan-converting the volumes to a Cartesian grid and computing echo decorrelation maps.

3.2.3.b RF generator control

The RF generator's (RITA 1500x RF generator, AngioDynamics, Queensbury, NY) built-in control methodology uses temperature readings pulled from the average of the 3 thermocouples within the targeted ablation zone to maintain a specified target temperature for a set amount of time. The RF generator's power delivery can be toggled via a button on its front panel or via a pneumatic switch intended to be used with a

foot pedal, but does not have an interface for digitally controlling the device's state or other operating parameters. Therefore, decorrelation based control was implemented by toggling the power delivery using the device's built-in pneumatic switch interface.
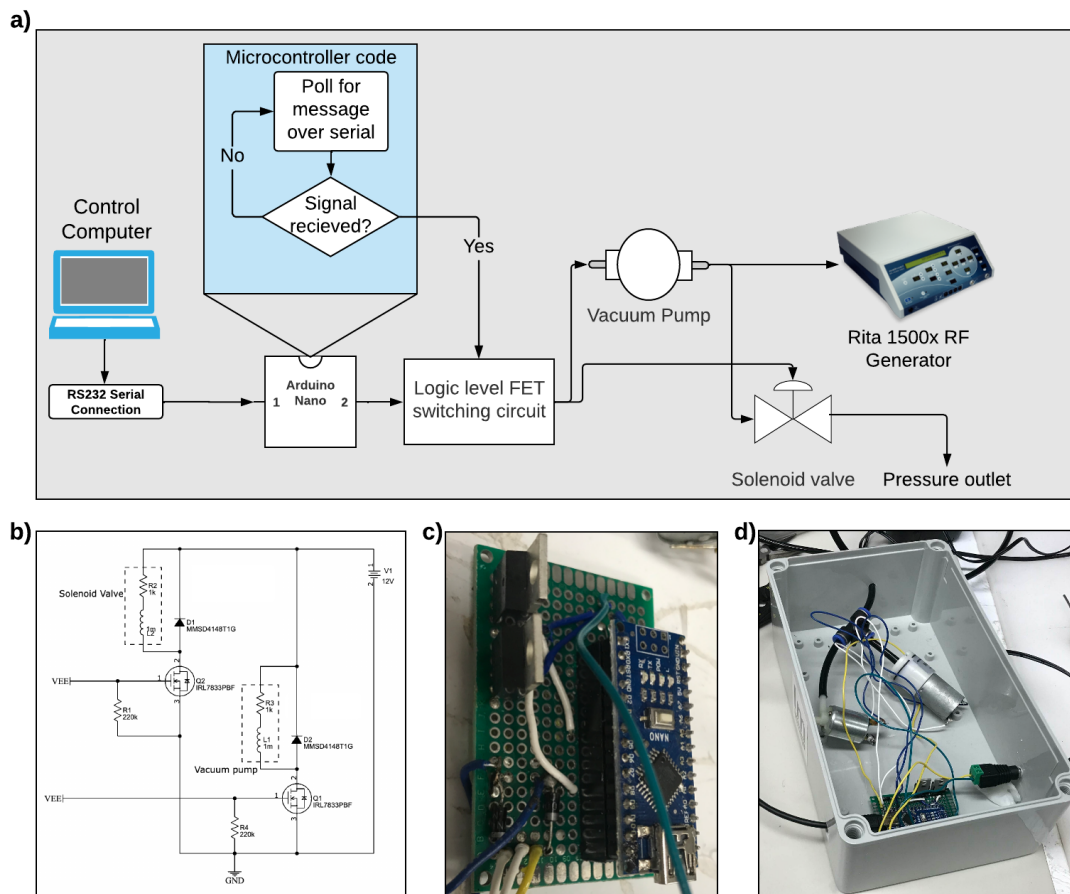
Figure 3.3: Device designed to control the RF generator via the built-in pneumatic switch automatically. (a) Block diagram of the device. (b) Logic-level MOSFET switching circuit that controls the vacuum pump and solenoid valve. (c) Image of the physical circuit soldered to a prototyping board. (d) Image of the entire device.

The action of the foot pedal was replicated in a computer-controllable manner via a microcontroller circuit connected to a vacuum pump and solenoid valve. These were off-the-shelf parts used for aquarium maintenance (vacuum pump) and coffee machines (solenoid valve). The vacuum pump simulated the action of the foot pedal being pressed while the solenoid valve released pressure from the tube. These devices were powered by a 12V DC power adapter and activated via a simple N-channel logic level MOSFET switching circuit connected to digital pins of a microcontroller. An Arduino Nano (Arduino NANO, Interaction Design Institute Ivrea, Ivrea, Italy) microcontroller connected

to the central control computer via an RS232 serial connection through USB performed logic for switching the vacuum pump and solenoid valve. The microcontroller was programmed to poll for a signal over the serial stream and activate the vacuum pump via the logic level MOSFET once the signal was received. Upon receiving a start signal, the device immediately switches on the pump to trigger the pneumatic switch. After a short 50 ms delay, the valve is switched to release built up pressure between the pump and pneumatic switch.

A block diagram of the device used for automatic control of the RF generator can be seen in Figure 3.3a, the circuit for driving the vacuuum pump and solenoid valve can be seen in Figure 3.3b and the physical implementation of the device can be seen in Figures 3.3c and 3.3d.

3.2.3.c   RF generator data output

The RITA 1500x's front panel displays critical operating parameters of the device, such as the instantaneous power, total ablation time and current temperature measured at the ablation needle's thermocouples. Unfortunately, Angiodynamics did not provide an off-the-shelf interface for programmatic monitoring of the device's internal parameters, nor could we find any relevant documentation to aid in doing so. Through suggestions in the manual, we could determine that one of the device's RS232 serial ports can be used to interface with an obsolete in-house proprietary software package, which the manufacturer was also unwilling to provide.

Failing to find solutions via normal channels, the serial stream needed to be reverse-engineered. The suspected serial output port was connected to a laptop via a USB RS232 adapter and sniffed with a C++ program utilizing Microsoft Windows's built-in serial communications API. The raw output was analyzed to determine the stream's baud rate, packet delimiters and packet polling period, which were determined to be 9600 baud, a carriage return and 100 ms, respectively. The program was then modified to parse out bitstreams within each packet and export it to a file for further analysis. To determine how the information was encoded in each packet, a series of ablation trials were conducted

using beef round sourced from a local supermarket. During these trials, the front panel's displayed parameters were logged while the C++ program captured raw packets from the serial port. The timing of changes in the displayed parameters was compared with the timing of changes in the bitstream to determine which bits corresponded to each parameter.

After extensive trial and error, we determined that the values were encoded as 14-bit integers composed of the 7 least significant bits of every two adjacent bytes. Further testing was carried out to verify the units of the parameters, which were determined to be decidegree Celsius, ohms, seconds and watts for temperature, impedance, time and power quantities, respectively. A MATLAB class was then written to parse the serial stream and integrated into the rest of the codebase.

3.2.3.d   Optimization

Limitations of the Siemens SC2000 scanner's ability to export raw ultrasound data necessitated a series of optimizations to minimize latency for real-time control. Siemens provided various helpful tools for retrieving and reading raw data from the device's internal buffers. However, these tools were designed for debugging the system and, as such, were not optimized for real-time external image formation. Using the minimum viable imaging geometry, which would fully encompass our region of interest as described in section 3.2.2.b, we could only achieve a volume export rate of approximately every 6 seconds. Unfortunately, little could be done to remedy this due to the internal topology of the system. The latency between data acquisition and updating the control parameter thus had to be reduced at later stages in the pipeline.

Data from the debugging console is written to disk as non-standard signed hexadecimal 17-bit fixed-point numbers encoded as UTF-8 text. The text, therefore, needed to be scanned, parsed and recast into standard floating-point numbers before use. Siemens provided an interpreted MATLAB script to read these files, but it required an additional 6 seconds per volume pair. The provided function used computationally expensive interpreted formatted text reads for parsing the file and floating-point operations to recast

the fixed-point numbers, both of which introduced unnecessary latency. An improved version of the data parsing script was written as a compiled C++ binary implementing the MATLAB Executable (MEX) interface. File I/O was expedited through memory mapping the data file and indexing it based on its regular structure rather than string formatting. Typecasting was implemented as a series of bitwise operations to form the 17-bit fixed-point number into a standard 32-bit float. Briefly, the steps it performs are: signing the integer, bitshifting the data portion to the first bit of the fraction section of a standard IEEE 32-bit float, XORing the result with an integer designed such that the mantissa is equivalent to the magnitude of the fixed-point number, dereferencing the integer pointer, and pointing a float towards the memory address. This substantially improved computation time over the interpreted method, requiring approximately 0.22 seconds for the entire file, contrasted to 6 seconds in the original implementation.

It was also found that 3D scan conversion with trilinear interpolation was costly in interpreted code, so an additional set of C++ MEX files was written to optimize this process. As ablation geometry was standard between volumes, a look-up table of coefficients could be computed once and applied to each successive trial. Most floating-point operations are identical for a given geometry, so they can be separated from the rest of the floating-point operations and stored as a set of coefficients in a look-up table (LUT). The coefficients are stored as a list of structures pointing to specific indices within the provided serialized echo data. The LUT-based compiled code can convert both volumes in approximately .06 seconds, while the naive interpreted code required approximately 4 seconds per set. This could be further optimized with parallelization, but it was found unnecessary as the scanner was only capable of writing data every 6 seconds.

These limitations were largely artificial; a much higher time-resolution implementation of echo decorrelation would be feasible on standard ultrasound scanners equipped with modern parallel processing capabilities. As the scanner can output scan converted volumes at a rate of 117 VPS or higher with the resultant volumetric data passing through multiple linear filters before being displayed, theoretically an integrated version of echo

decorrelation imaging could be performed at near the same volume rate that B-mode images can be recorded.

3.2.4 RFA experiment design

3.2.4.a Tissue Handling

Bovine liver tissue was acquired from a local butcher less than 24 hours postmortem and kept refrigerated until approximately 30 minutes before experiments. Once the tissue had acclimated to room temperature (20 to 25 °C), it was sectioned into roughly cubic pieces ($70 \times 80 \times 80$ mm^3), taking care to avoid large arteries or other inhomogeneous portions within each piece. A custom polylactic acid (PLA) 3D printed apparatus, pictured in Figure 3.4(b), consisting of a cuvette, stand, and lid was designed to ensure repeatable exposure conditions between trials. Each sectioned tissue piece was placed within an individual cuvette with a dimension of $100 \times 82 \times 82$ mm^3. The top of the cuvette is exposed for placement of the ablation needle and a rectangular window on its anterior face is exposed for imaging. The cuvette's imaging window was then covered with an adhesive Tegaderm film (3M Health Care, St. Paul, MN, USA) before being filled with phosphate-buffered saline solution (PBS) (0.01 M, pH 7.4 at 25°C, Sigma Life Science P3813, St. Louis, MO, USA) and agitated to remove any air pockets. Once each cuvette had been prepared, it was placed on the guiding stand and secured to the lab bench via a mechanical arm.

3.2.4.b Thermal ablation experiments

RFA was performed using a Rita 1500x RF generator with an XLi enhanced needle with saline infusion (AngioDynamics, Latham, NY, USA). Before each trial, the saline infusion needles were purged with phosphate buffered saline (PBS) solution (0.01 M, pH 7.4 at 25 °C, Sigma Life Science P3813, St. Louis, MO) until they presented a steady flow. A grounding pad cut from a standard dispersive electrode (RITA Thermopads, AngioDynamics, Manchester, GA, USA) was attached to the RF generator's ground terminal and inserted between the tissue and cuvette on its posterior face. A lid fit with

a)

b)
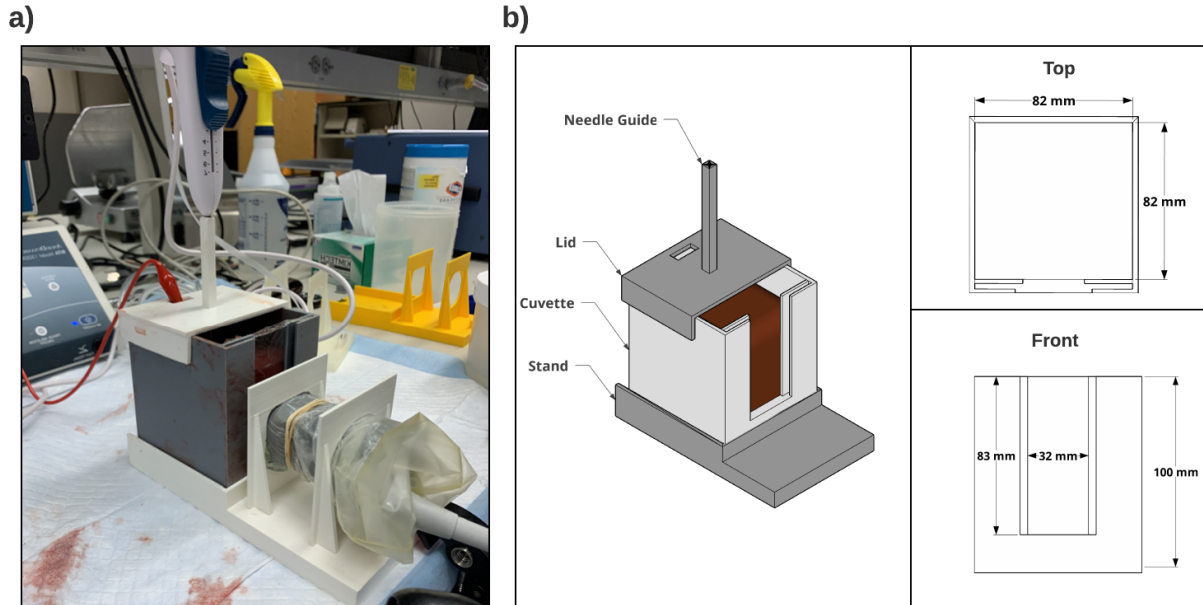
Figure 3.4: Experimental setup used for RFA trials. (a) Image of the physical setup where the 3D printed cuvette, stand, and lid are affixed to the benchtop via a mechanical arm. A roughly cubic sample of bovine liver was placed within the cuvette and imaged with a 4Z1c matrix array transducer; the XLi enhanced probe was then placed through the needle track and connected to the RF generator's ground terminal. (b) Illustration of the 3D printed parts with their corresponding dimensions.

an integrated needle guide, designed such that the needle's tip would be 40 mm from the bottom of the box, 52 mm from the imaging window and centered in the azimuthal direction, was then affixed to the top of the cuvette. Actual needle placement measured from segmented tissue histology was found to vary between 52–54 mm in depth. The ablation needle was inserted into the tissue through the needle guide and left unplugged to reduce any undesired heating before the trial. The cuvette was then filled with PBS solution and agitated to remove any remaining air pockets.

Ultrasound imaging was performed using a Siemens 4Z1c matrix array transducer connected to an SC2000 ultrasound imaging system (Acuson SC2000 and 4Z1c matrix array, Siemens, Erlangen, Germany). The transducer was placed within a latex probe cover and acoustically coupled to the tissue via Aquasonic ultrasound transmission gel (Parker Laboratories, NJ, USA) on the inside and outside of the body. A set of guiding rails affixed to the stand, pictured in figure 3.2.4.b(a), hold the ultrasound probe against the imaging window of the cuvette. The probe was set to record with an azimuthal and elevational scan angle range of 56° and a nominal depth of 70 mm (recorded data extended

slightly further to approximately 81 mm). These settings were selected to minimize the inter-volume time while still imaging the entire ablation zone with a margin equal to at minimum 3× the Gaussian window's σ parameter isotropically around the ablation zone to ensure minimal boundary effects within the ROI.

Ablation exposure conditions were set to 7 minutes of treatment time, a target temperature of 110°C, and a maximum power output of 50 W. The RF generator utilized its built-in temperature control functionality to heat the tissue to the targeted temperature and maintain that temperature for the set treatment time. A plot of the device's temperature control behavior can be seen in Figures 3.5a and 3.5b. The RF generator adjusts its power delivery based on impedance and temperature readings integrated into the ablation needle to achieve a roughly linear increase in temperature. Once the mean temperature among all integrated thermocouples overshoots the target temperature, it maintains that temperature for the set treatment time. Upon completing the treatment cycle, it enters a cooldown phase before indicating that it can be removed.

An initial set of 5 pulse-echo volumes were recorded prior to ablation to form the sham decorrelation map. The RF generator was then activated by the control computer and allowed to run through the entire treatment time while pulse-echo volumes (set to the same parameters as the initial volumes) were recorded every 6 seconds and transferred to a connected laptop to compute decorrelation maps.

3.2.5   Sectioning and segmentation

The relationship between echo decorrelation and thermal lesioning was assessed via direct comparison of computed cumulative decorrelation maps with segmented tissue histology. The method we employed was similar to previous studies of ultrasound-based ablation monitoring [74, 84, 85] using linear arrays, but required some modifications to ensure proper registration of volumetric tissue data. Specifically, each specimen was sectioned into multiple parallel lateral slices, each of which was used to create a 2D segmented binary mask. These masks are then combined into a 3D mask of tissue ablation.

36
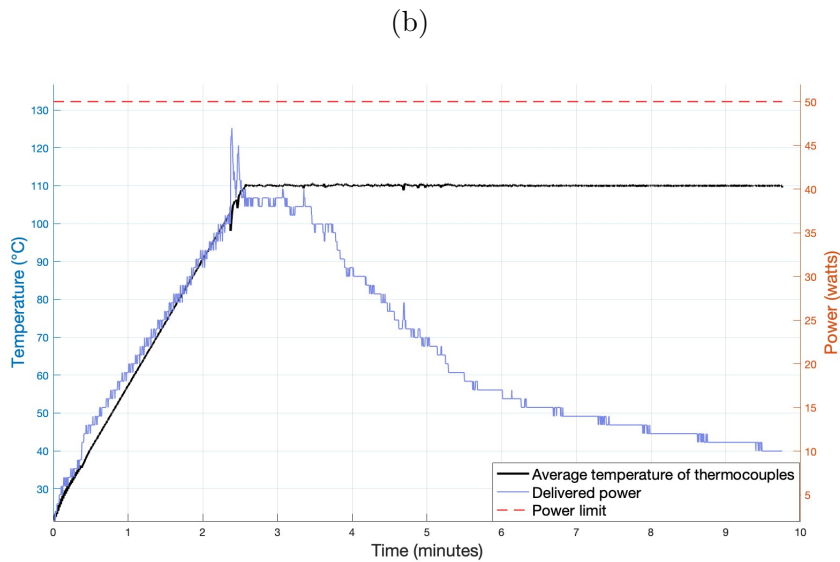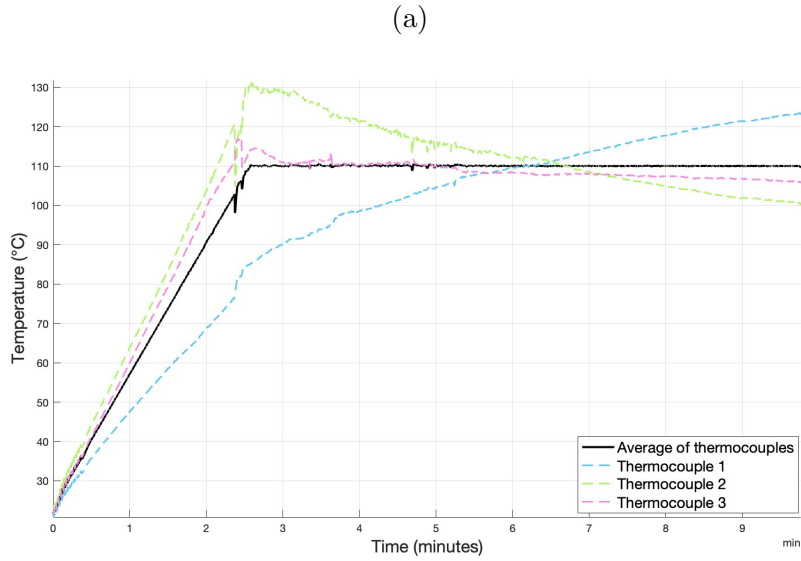
Figure 3.5: Representative example of the RITA 1500x RF generator's default temperature-controlled ablation behavior. (a) Plot of temperature across thermocouples 1–3 for the entire duration of an uncontrolled ablation trial. The mean temperature across all thermocouples, shown in black, is used as the control parameter for temperature-based control of the device. (b) Delivered power and average temperature across all thermocouples in the same trial. The device attempts to increase temperature linearly based on the mean temperature of the thermocouples and current delivered power. At minute 2.3 of the trial, the temperature falls below the target and power is rapidly increased to maintain the target. Once the mean temperature across all thermocouples overshoots the target, the delivered power is regulated to maintain the current temperature.

To minimize geometric deformation during sectioning, ablated tissue was left within the imaging cuvette and transferred to a -80 °C temperature-controlled freezer for a minimum of 24 hours. Once frozen, the tissue was removed from the freezer and partially thawed in a warm water bath. Shallow incisions were cut into the sagittal plane at a regular interval of 5 mm to restrict the height of each slice. The tissue was then sectioned into azimuth-depth planes with a width of approximately 3.5 mm using a commodity deli slicer. The elevational bounds of the ablated region were recorded based on the cuts along the elevational face; the needle tip's location was also registered to account for any deformation resulting from freezing. Each plane was imaged using an optical scanner (V550, Epson America, Inc. Long Beach, CA, USA) with an imaging resolution of 660 DPI.
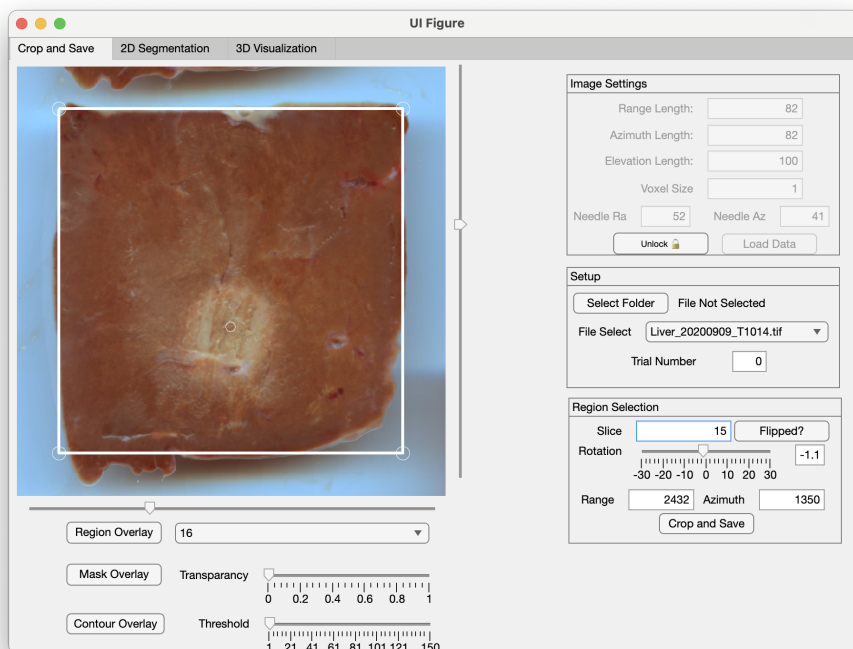
Figure 3.6: Alignment and file selection panel of the MATLAB image segmentation GUI. Each scanned plane of tissue was aligned with a square corresponding to the cuvette's inner (depth × azimuth) area via sliders which translated and rotated the image. Once aligned, the image was cropped and saved for later segmentation. For sections where the boundaries of the box are unclear, the GUI can display multiple additional landmarks (outer edge contours, previous slice with transparency) based on previously segmented sections to aid in registration.

(a)
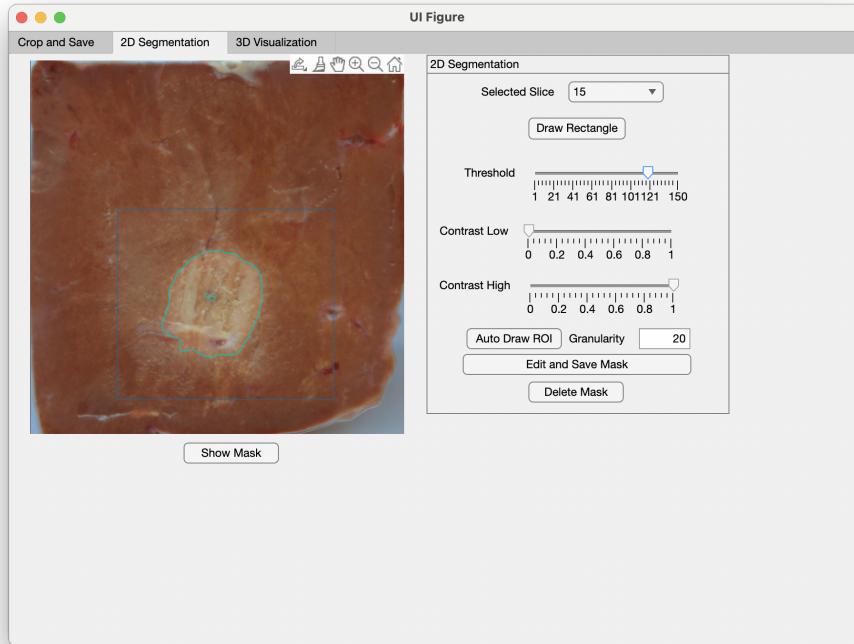
(b)
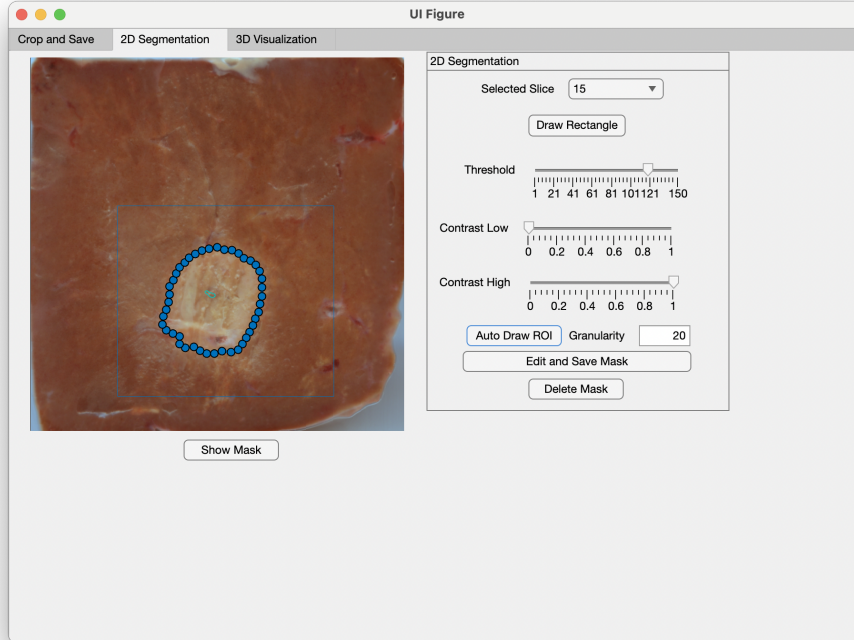
Figure 3.7: Segmentation panel of the MATLAB image segmentation GUI. (a) Depth-azimuth tissue slice with a user-defined contour line overlaid on the ablated region. (b) Automatically generated polygonal region overlaid on the contour, where each vertex can be adjusted to account for inaccuracies in the automatically generated region.
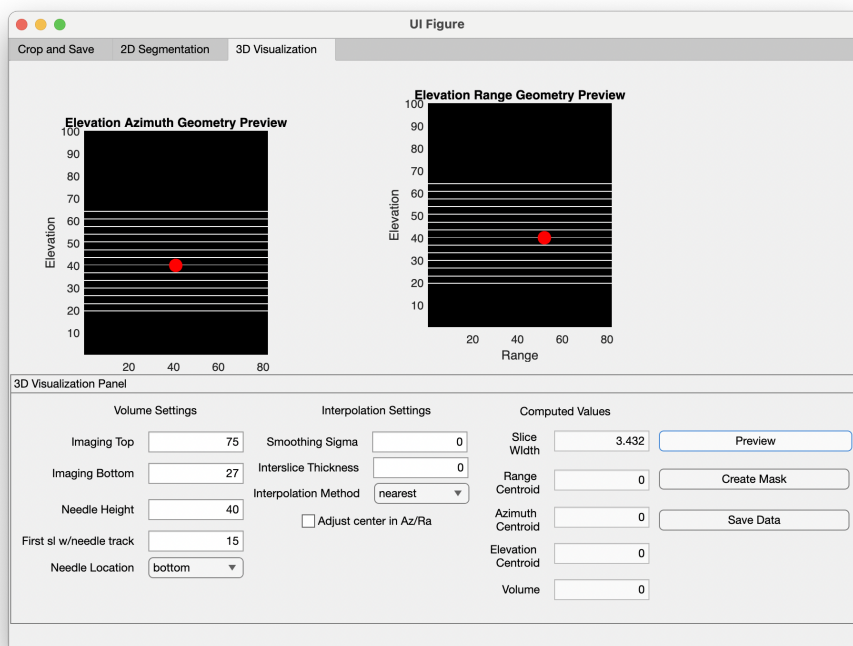
Figure 3.8: Volumetric mask generation panel of the MATLAB image segmentation GUI. Parameters for the recorded ablation start height, end height and needle tip height were used to generate a 3D mask from a series of 2D masks. The two panels on the top of the GUI are used to verify registration along the elevational (orthogonal to 2D slices) plane. Each white line is a single 2D plane, shown in its room-scale location according to parameters entered in the 'volume settings' panel. A red dot is placed at the location of the needle tip to correct any deformation in the elevational plane.

The optical scans of azimuth-range planes were segmented into 2D binary images where 1 represents ablated tissue and 0 represents unablated tissue. A custom-designed semi-automated MATLAB GUI was used to accurately register the tissue scans to their position in the cuvette. The GUI cycles through each optical scan and allows the user to translate and rotate the image to align with a square representing the cuvette's inner walls. A contour is then overlaid on the tissue scan around the borders of the ablation zone based on an adjustable isoline of average pixel intensities across all channels. Once a suitable contour representing the boundary of the ablated region is found, a polygonal region is placed along the contour, which can be manually adjusted to account for any irregularities in pixel intensity that distort the automatically generated region.

The 2D masks are combined into a sparse 3D volume corresponding to their room-scale location as indicated by the measured start and end of the ablation zone. The image is then adjusted based on the measured location of the needle tip to account for any deformation in the elevational plane. Values between slices in the elevational direction are computed via nearest-neighbor interpolation based on the nearest two parallel tissue sections. The mask is then smoothed using a 3D Gaussian filter, rounded to form a 3D binary mask and scaled to match the recorded ultrasound data. A screenshot of the program used for segmenting 2D images can be seen in figures 3.6, 3.7a and 3.7b, while the GUI panel for combining the 2D masks into a 3D matrix can be seen in figure 3.8. Trials were excluded if the scanned tissue histology did not clearly show the entire 3D ablated region. Two trials were excluded because, in these trials, part of the ablated region could not be imaged, due to a large portion of the region becoming detached from the tissue before sectioning.

3.2.6   Prediction of local ablation

Prediction of local ablation was evaluated through ROC analysis of the computed 3D cumulative decorrelation map and 3D ablation masks derived from segmented tissue histology. ROC curves provide a measure of the strength of a predictor under a varying threshold. In ROC analysis, the threshold for the predictor is allowed to vary and the
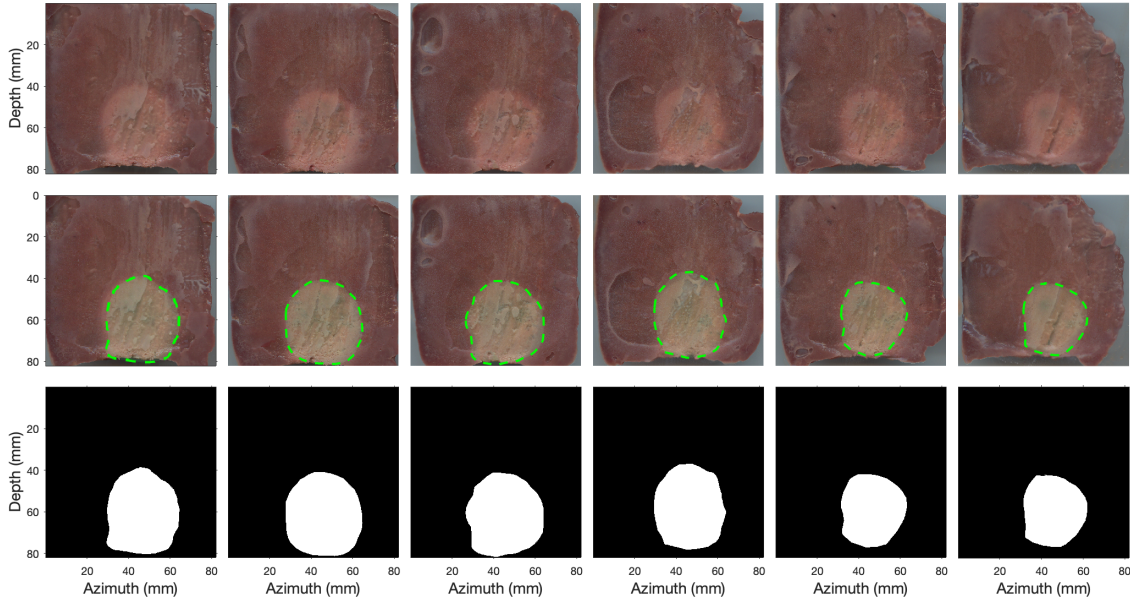
Figure 3.9: Representative tissue histology of 6 azimuth-elevation planes. (a) Optical scans of azimuth-depth (82×82 mm) sectioned tissue histology with a slice width of 3—3.5 mm. The top row shows optical images fit to an 82×82 mm square representing the inner dimension of the cuvette. The middle row shows the same images with a green dotted line overlaid around the ablated region, and the bottom row shows the final 2D binary mask for each 2D section.

false-positive rate (1 − Specificity) and true-positive rate (Sensitivity) are computed for each threshold. A curve is then constructed as the false-positive rate vs. the true-positive rate. These terms are computed as

$$\text{Sensitivity} = \frac{\text{TP}}{\text{TP} + \text{FN}} \tag{3.8}$$

$$1 - \text{Specificity} = \frac{\text{FP}}{\text{FP} + \text{TN}} \tag{3.9}$$

where TP is the number of correctly predicted ablated voxels, FP is the number of incorrectly predicted ablated voxels, TN is the number of correctly predicted unablated voxels, and FN is the number of incorrectly predicted unablated voxels.

The area under the curve (AUC) of the ROC curve provides a measure of the strength of the predictor; a value of 1 indicates perfect predictive ability, while a value of .5 indicates that the predictor is no better than chance [88]. This value is computed using numerical integration via the trapezoid rule on the computed ROC plot.

The statistical significance of the resultant AUC is assessed via the computation of a sample size adjusted Z-score. The windowing function in the definition of echo decorrelation introduces statistical dependence in geometrically nearby voxels, necessitating an adjustment of the sample size to only the number of statistically independent voxels. As the window impacts nearby voxels isotropically, the number of sufficiently independent samples can be determined by the maximal sphere packing density within the volume. The effective number of points N_{eff} is then computed as

$$N_{\text{eff}} = \frac{N \delta_{\text{v}}^3}{\rho_{\text{sph}} d^3} \tag{3.10}$$

where δ_{v} is the voxel step size, N is the number of voxels within the tested region, d is the diameter of each sphere and $\rho_{\text{sph}} = \frac{\pi}{3\sqrt{2}}$ is the maximum close hexagonal packing density of equal radii spheres, defined as the number of unit diameter spheres per unit length cube. An illustration of close sphere packing can be seen in Figure 3.10, where each sphere represents a single effectively independent point, and the spheres are packed in close hexagonal spacing. The diameter chosen for the sphere is the full width at half
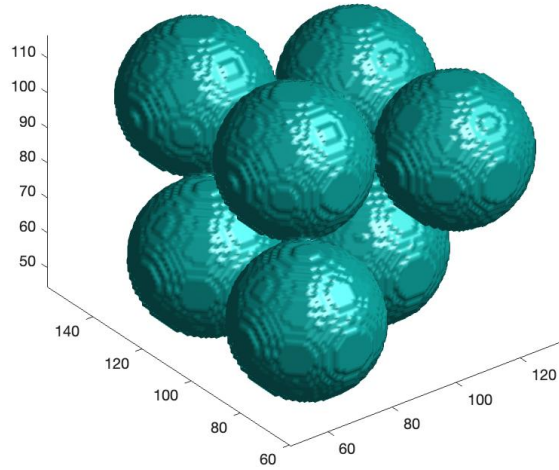
Figure 3.10: Illustration of sphere packing for determination of an effective sample size with sufficiently low statistical dependence.

maximum (FWHM) of the windowing function. For a Gaussian window this is

$$d = 2\sqrt{2\log(2)}\sigma \qquad (3.11)$$

The adjustment for sample size effectively limits the spatial resolution of echo decorrelation maps to the diameter of the sphere, as only voxels occurring at minimum d mm away from other voxels are considered independent measurements.

Standard error for the uncorrected ROC curve was computed using MATLAB and the total sample and statistical significance was determined via a sample size adjusted Z-statistic (Z_{eff}), which is computed as

$$Z_{\mathrm{eff}} = \frac{Z}{\sqrt{\frac{N_{\mathrm{total}}}{N_{\mathrm{eff}}}}} \qquad (3.12)$$

where Z_{eff} is the Z-score calculated from the ROC curve, N_{total} is the number of samples within the tested region and N_{eff} is the number of effectively independent samples. A two-tailed effective significance value, p_{eff}, for the sample size adjusted AUC Z-score, Z_{eff}, is then computed as

$$p_{\mathrm{effective}} = 2 \cdot (1 - \mathrm{cdf}(Z_{\mathrm{eff}})) \qquad (3.13)$$

Rejection of the null hypothesis is assumed if $p < .05$, indicating that the sample size adjusted AUC is significantly different from the value expected by chance (AUC=.5).

Differences in AUC values between groups is assessed similarly to difference between the AUC and random chance (AUC=.5). The value for standard error of the ROC curve is used to determine an adjusted Z-score for the difference between each compared ROC curve, and the $p-$value is computed from equation 3.13.

3.2.7   Preliminary trials

3.2.7.a   Initial RFA trials without feedback-control

Initial assessment of 3D echo decorrelation's performance as a predictor of local tissue lesioning in *ex-vivo* bovine liver was carried out through a preliminary series of trials

($N = 9$) without the use of echo decorrelation feedback control following the procedure outlined in section 3.2.4. For 'uncontrolled' trials, ablation time and power delivery were controlled by the RF generator's built-in temperature-controlled mode, which modulates delivered power in order to keep the targeted region at a set temperature as signaled by its built-in thermocouples. The RFA probe was set to target a 3 cm diameter region of tissue, with a maximum power output of 50 W, target temperature of 110° C and a treatment time of 7 minutes at the target temperature. Following each ablation, treated tissue was frozen, sectioned and segmented as described in section 3.2.5. Performance in prediction of local ablation was evaluated via ROC analysis between computed cumulative echo decorrelation maps and segmented tissue histology. The results of ROC analysis in these trials was used as a preliminary estimate for an appropriate decorrelation threshold.

The log10-scaled spatially averaged mean decorrelation within the targeted ablation zone, $\hat{\Delta}_{\mathrm{avg}}$, was computed for each of the initial uncontrolled trials and used to inform an initial threshold for feedback-controlled trials. The initial threshold for feedback control was selected to maximize the likelihood of successful control by choosing a value lower than the minimum post-hoc computed values for $\hat{\Delta}$ in the initial set. Additionally, the relationship between $\hat{\Delta}_{\mathrm{avg}}$ and total ablation volume was evaluated using linear regression to determine if there was a relationship between the prospective control criterion and total ablation volume.

3.2.7.b   Preliminary RFA trials with feedback control

A series of preliminary echo decorrelation feedback-controlled trials ($N = 8$) were then performed at varying thresholds covering log10-scaled decorrelation per millisecond values between $\log_{10} \Delta_{\mathrm{thresh}} = -3.5$ and -3. Multiple thresholds were used to evaluate the relationship between thermal lesioning and the control criterion and to provide data points at different ablation sizes in relation to the control parameter. The preliminary feedback-controlled trials were performed in tandem with an additional set of uncontrolled trials ($N = 10$) to account for any differences in tissue samples. Trials were completed with identical RFA exposure conditions (50 W, 110° C temperature target, 7 minute

ablation time, 3 cm diameter) to the initial uncontrolled group. The same analysis of local lesioning prediction completed in the initial set was also completed on the preliminary set of feedback-controlled and uncontrolled trials.

Following the first set of feedback-controlled trials, an additional set of preliminary trials were completed with saline infusion ($N = 11$), of which the majority were feedback-controlled ($N = 7$) with some additional uncontrolled trials ($N = 4$). Control threshold values for this group were between $\Delta_{\text{thresh}} = -2.8$ and -2.2, a range which was informed by the results of the preliminary trials without saline infusion. Saline infusion was used to increase the total diameter of ablation by ensuring adequate cooling in the targeted region and thereby reducing the likelihood of charring-induced electrical impedance spikes. The use of saline infusion would also more closely match the typical clinical practice for ablation procedures and would therefore provide lesioning characteristics closer to what would be expected in a real clinical setting.

Post-hoc analysis was completed on all preliminary trials combined, as well as on each of the constituent groups to evaluate local ablation prediction performance as well as to evaluate the relationship between the control parameter and the total ablated volume. Local ablation was evaluated using ROC analysis, and values for optimal prediction of local ablation were computed. Differences between groups in terms of predicting local lesioning were assessed as stated in 3.2.6. The effect of saline infusion was further analyzed to determine the relevance of previous trials without saline infusion in the determination of a final control threshold.

3.2.8 Control threshold determination

The final feedback control parameter was informed through a combination of local ablation predictive ability and full volume predictive ability. A decorrelation threshold which predicted local tissue lesioning with 90% specificity, to ensure a high likelihood of targeted tissue being ablated, was desired. In addition to the analysis of local tissue ablation, further analysis was completed to determine the likelihood of a given decorrelation threshold resulting in 80% and 90% of the targeted region being ablated. The proposed

control parameter, $\hat{\Delta}_{\mathrm{avg}}$, was computed for all feedback-controlled and uncontrolled trials and used as a predictor of 90% and 80% ablation of the targeted region. Trials that resulted in 80% of the targeted region being ablated were assigned a value of 1, and trials that did not were assigned a value of 0; the spatial mean of the cumulative decorrelation map within the targeted 3 cm diameter sphere centered at the needle tip was then used as a predictor for 80% ablation of the targeted region. Sensitivity and specificity values were computed for the mean decorrelation within the ROI as a predictor of a proportion of the volume being ablated, and a threshold value was selected that achieved high specificity in the prediction of 80% ablation of the targeted region. This analysis was repeated for 90% ablation as well.

The final chosen value for the decorrelation threshold was selected to achieve high specificity and reasonable sensitivity for prediction of both local lesioning and the total ablation volume, as well as through general observations on lesioning in the preliminary set of trials.

3.2.9 Final feedback controlled trials

After determining an appropriate control threshold through the process described in the previous section, a set of final feedback-controlled ($N = 11$) and uncontrolled ($N = 11$) trials were performed. Each liver sample was prepared as outlined in Section 3.2.5 and divided into a feedback-controlled and uncontrolled group in roughly equal proportion. Uncontrolled trials were completed in a nearly identical manner to the preliminary uncontrolled trials with saline infusion, with the same probe placement, transducer placement, imaging settings and RF exposure conditions. The control threshold was held constant at $\log_{10} \Delta_{\mathrm{thresh}}/\mathrm{ms} = -2.2$, which was determined from analysis of the preliminary set of trials.

Post-hoc analysis on local ablation, as well as full ablation of the targeted region, was completed in a manner identical to the preliminary trials. Additional analysis was completed on control performance with a constant threshold, which will be outlined in detail in the next section.

3.2.10 Analysis of feedback control performance

3.2.10.a Ablation volume

Ablation volume was computed as the summed volume of all ablated voxels within the segmented 3D binary masks generated from the scanned tissue histology, as described in section 3.2.5. The mean ablation volume in the feedback-controlled and uncontrolled groups was assessed to determine the efficacy of echo decorrelation feedback in optimizing for the desired ablation volume. Additionally, the variance of the volume between these groups was assessed to determine if echo-decorrelation feedback results in a more consistent ablation volume. The difference in means was assessed via a two-sided Student's t-test, where the null hypothesis (that the two groups have equal means) is rejected if $p < .05$. Similarly, differences in variance are assessed via the F-test of equal variance, and the null hypothesis is rejected if $p < .05$.

The F-test and t-test are only valid if the samples are normally distributed [89], as the sample size in this study ($N = 11$ for each group) is not sufficiently large to assume normality under the central limit theorem. Alternative non-parametric tests would be used if the population did not display normality. Normality was assessed via the Shapiro-Wilk normality test, which is an effective normality test for smaller sample sizes ($N < 50$) [90]. For the Shapiro-Wilk test, the null hypothesis (that the population is non-normal) was rejected if $p < .05$. The two groups were assessed separately to determine if they follow a normal distribution and can be analyzed via standard statistical tests. Pending affirmation of normality, the average volume between the two groups was assessed for statistical significance using the two-sided Student's t-test. Contingently, if the groups were non-normal, the non-parametric Smirnov test would be used to determine statistical significance between the two sets.

We hypothesized that an increase in the mean decorrelation within the targeted region, equivalent to the control parameter for controlled trials ($\hat{\Delta}_{\mathrm{avg}}$), would be associated with greater thermal lesioning. This was tested with linear regression of the total ablation size vs. mean decorrelation within the targeted region. Significance was assessed via the

48

F-statistic vs. a constant model; the null hypothesis (that the observed fit is no better than a constant model) would be considered rejected if $p < .05$.

The ablation rate was assessed to evaluate if feedback control resulted in more efficient lesioning. Ablation rate is computed as the bulk ablation volume per second of treatment time. The sum of all ablated voxels was divided by the total duration of ablation provided by the RF generator's serial interface data output. Total ablation time between the two groups was compared using a two-sided Student's t-test to determine if there was a significant difference in treatment efficiency between the two groups. The variance in ablation rate was also assessed using the F-test.

3.2.10.b   Ablation geometry

Geometric conformance to the desired ablation zone was measured via the Sorenson-Dice coefficient. The Dice coefficient provides a score for the similarity between two sets of binary points and is defined as:

$$\text{DSC} = \frac{2|X \cap Y|}{|X| + |Y|} \tag{3.14}$$

where X and Y are two sets of binary classifiers; in our case, this refers to voxels within a targeted region and the 3D binary mask generated from tissue histology.

The score takes values between 0 and 1, where 1 denotes an identical set and 0 denotes a mutually exclusive set. Observed ablation maps are compared to an ideal 15 mm radius sphere centered on the end of the needle track. The voxels within a 25 mm radius sphere surrounding the ablation needle tip were used for evaluation of the Dice coefficient. For our purposes, the Dice coefficient was computed as

$$\text{DSC} = \frac{2 \cdot \text{TP}}{2 \cdot \text{TP} + \text{FP} + \text{FN}} \tag{3.15}$$

where TP is the number of voxels in the targeted ROI which were successfully ablated, FP is the number of voxels outside of the targeted region that were ablated (overabla-

tion), and FN is the number of voxels within the targeted region that were not ablated (underablation).

The Dice coefficient was analyzed similarly to ablation volume, with normality being assessed with the Shapiro-Wilk normality test and the difference in means assessed by the 2-sided student's t-test. The variance between the two groups was then compared via the F-test to determine if the ablation geometry was more uniform in either group.

Following the hypothesis that total thermal lesioning would generally increase with the mean-decorrelation within the targeted region, a larger mean-decorrelation value would be associated with greater lesioning outside of the targeted region (false positives). A smaller mean-decorrelation value would be associated with unablated tissue within the targeted region (false negatives). Thus, we hypothesized that the Dice coefficient would be optimized near the targeted ablation threshold and lower at thresholds above and below this optimal threshold. To test this hypothesis, quadratic regression was performed on the Dice coefficient vs. mean decorrelation value within the targeted region.

3.3   Results

3.3.1   Preliminary trials

3.3.1.a   Initial uncontrolled trials

ROC curves for the prediction of local ablation via echo decorrelation imaging for the first set of preliminary uncontrolled trials ($N = 9$) can be seen in figure 3.11a. The area under the curve was found to be .785 ($p < 10^{-16}$), indicating significantly better predictive power than chance (AUC=.5, $p < 10^{-16}$). The minimal log10-scaled decorrelation per ms threshold achieving 90% ($\Delta_{90\%}$) specificity was found to be –2.43, with a corresponding sensitivity of 30.2%. The optimal point of the ROC curve for prediction of local ablation (Δ_{opt}) was found to be –3.07, and resulted in specificity and sensitivity of 67.2% and 76.2% respectively. Figure 3.11b shows the odds plot of the same ROC curve with vertical lines representing $\Delta_{90\%}$ and Δ_{opt}.
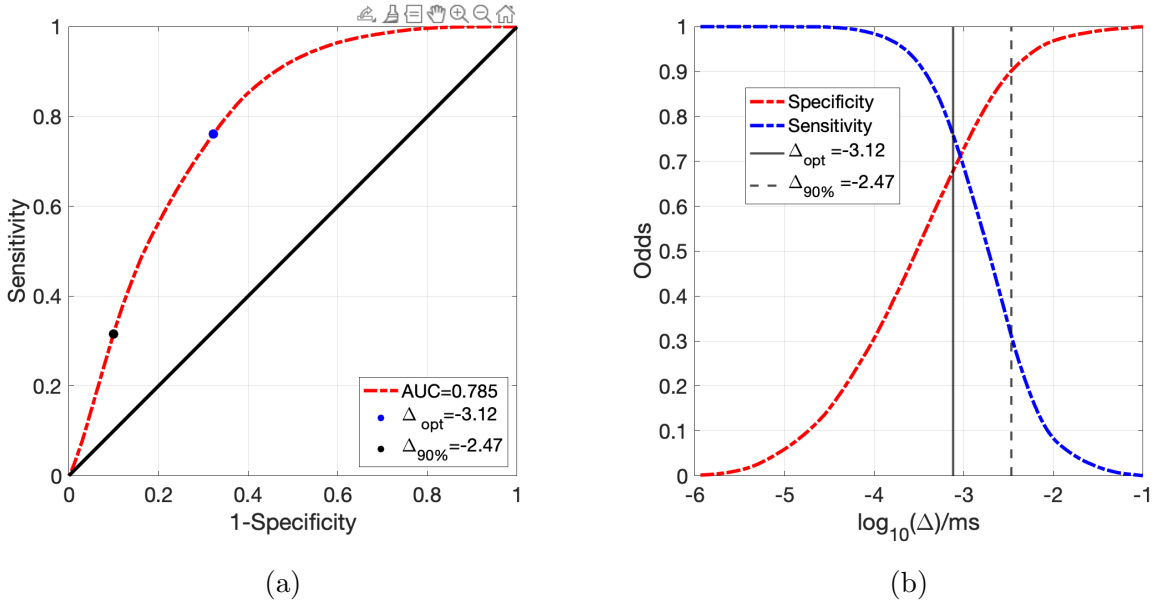
Figure 3.11: Results for prediction of local ablation in the initial set of preliminary uncontrolled trials ($N = 9$). (a) ROC curve for prediction of local tissue ablation across all initial trials, with the optimal point for prediction of local ablation ($\Delta_{\mathrm{opt}} = -3.08$) shown in blue and the minimum threshold achieving 90% specificity ($\Delta_{90\%} = -2.41$) shown in black. (b) Odds plots of sensitivity and specificity per $\log_{10}$ decorrelation threshold with Δ_{opt} and $\Delta_{90\%}$ marked with a solid and dashed vertical line respectively.

The mean ablated region in the initial group of uncontrolled trials was found to be 16.76 ± 5.04 mL (mean $\pm$ standard deviation). Figure 3.12a and 3.12b show the total ablation volume and Dice coefficient plotted against the log10-scaled spatial average decorrelation within the targeted ablation zone. A slight but insignificant correlation was found between the spatial average decorrelation within the targeted ablation zone and total ablated volume (R^2=.101, $p = .406$). Similarly, a scatter plot of log10-scaled spatial average decorrelation vs. Dice coefficient between segmented tissue histology and an ideal 15 mm radius sphere centered at the needle tip can be seen in Figure 3.12b, which showed no clear relationship between the two quantities.
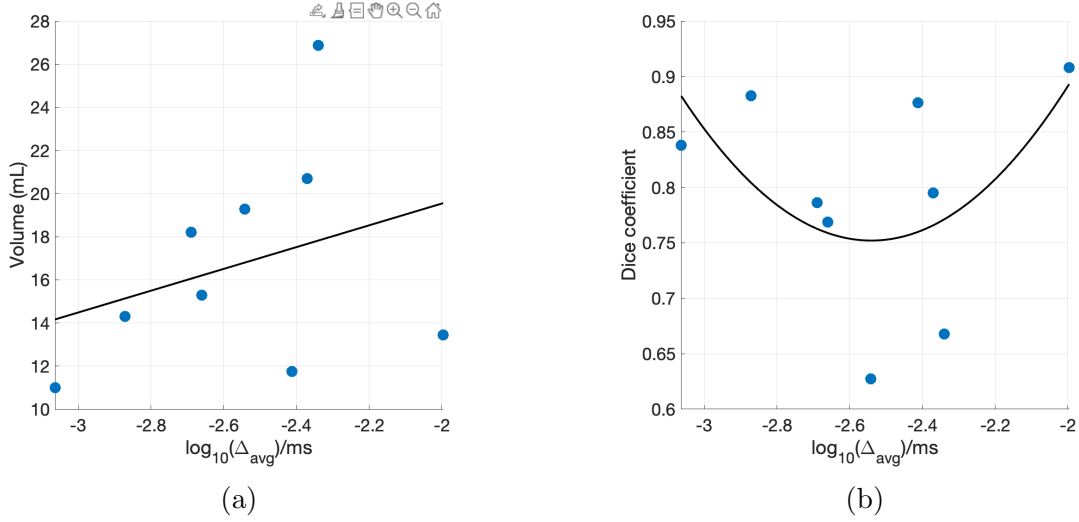
Figure 3.12: Scatter plots of log10-scaled average decorrelation within a targeted 15 mm radius ablation zone centered at the needle tip vs. (a) total ablation volume and (b) Dice coefficient between segmented and targeted ablation zones.

The minimum $\log_{10}$-scaled spatial average decorrelation per millisecond within the ROI, $\hat{\Delta}$, in the initial group was found to be –3.08. This informed the thresholds to be used in subsequent preliminary feedback-controlled trials. The threshold was selected to be significantly below the minimum observed mean decorrelation value within the targeted region in order to maximize the likelihood of successful control. The initial value for the log10-scaled control criterion was chosen as $\Delta_{\text{thresh}} = -3.5$; subsequent values were selected to be between $\Delta_{\text{thresh}} = -3.25$ and $\Delta_{\text{thresh}} = -2.2$, which covered the majority of the observed values ($\log_{10} \hat{\Delta} = -3.08$ to -1.9) in the initial set of trials without echo decorrelation feedback. The lower chosen threshold ($\Delta_{\text{thresh}} = -3.5$) roughly corresponded

to a local lesioning prediction with 50% specificity and 95% sensitivity, while the higher value ($\Delta_{\text{thresh}} = -2.2$) corresponds to 90% specificity and 50% sensitivity.

3.3.1.b Preliminary feedback-controlled and uncontrolled trials without saline infusion

All ($N = 8$) preliminary feedback-controlled trials without saline infusion were successfully controlled. A trial was considered 'successfully controlled' if the average decorrelation within the ROI, $\hat{\Delta}_{\text{avg}}$, exceeded a set threshold and the treatment was stopped early. The distribution of thresholds in these trials was: $\log_{10} \Delta_{\text{thresh}} = -3.5$ ($N = 1$), -3.25 ($N = 1$) and -3 ($N = 6$). The uncontrolled group of preliminary trials without saline infusion ($N = 19$) had a significantly larger ablation volume of 12.75 ± 6.17 mL (mean $\pm$ std) compared to 4.91 ± 2.31 mL for the controlled group ($p = .013$). Additionally, total ablation volume within the feedback-controlled group had a significantly smaller variance than the uncontrolled group ($p = .013$), providing some preliminary evidence for feedback control resulting in a more consistent thermal lesion.

A scatter plot of log10-scaled mean decorrelation within the targeted region vs. ablation volume can be seen in Figure 3.13a. A slight correlation was found between the spatial mean of decorrelation within the targeted ablation zone and the total ablation volume computed from sectioned tissue histology which was found to be significant ($R^2 = .203$, $p = .021$), suggesting a moderate relationship between the spatial average decorrelation and ablation volume.

The mean Dice coefficient in the uncontrolled group without saline infusion was found to be $.717 \pm .133$, while the mean in the feedback-controlled group was $.477 \pm .169$. The difference in Dice coefficients between the uncontrolled and feedback-controlled trials and the difference in variance between those groups reached statistical significance under the t-test ($p = .63$) and F-test ($p = .59$), respectively. A scatter plot of the Dice coefficient vs. log scaled spatial mean decorrelation within the ablation zone is shown in Figure 3.14a. As most trials resulted in little ablation outside the ablation zone, the Dice coefficient vs. spatial mean decorrelation resembles the relationship between volume and spatial

(a)   (b)
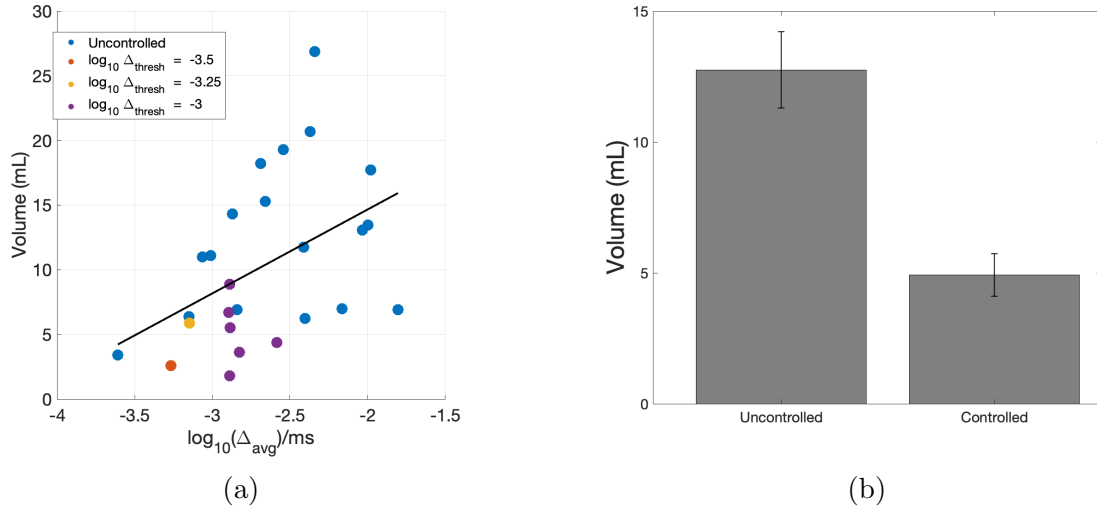
Figure 3.13: Results for total ablation volume in the preliminary group of feedback-controlled ($N = 8$) and uncontrolled trials ($N = 19$) without saline infusion. (a) Scatter plot of log10-scaled average decorrelation within a targeted 15 mm radius ablation zone centered at the needle tip vs. total ablation volume with overlaid least-squares optimized linear fit. (b) Bar plot of mean volumes in the feedback-controlled and uncontrolled groups, with error bars showing standard error.

mean decorrelation. A quadratic regression was performed on the Dice coefficient vs. spatially averaged decorrelation within the targeted ablation zone, which was found to have not reached statistical significance ($p = .135$). The relatively poor performance in the feedback-controlled group in terms of the Dice coefficient suggested that the trials were stopped too early and that our control threshold was too low. Both groups had a mean total ablation volume less than the volume of the targeted ablation volume, which for a 15 mm radius sphere would be 14.14 mL. This informed our decision to use saline infusion in the subsequent set of preliminary trials.

ROC curves for prediction of local ablation in the preliminary controlled and uncontrolled group can be seen in figure 3.15. The AUC of the ROC curve in the feedback-controlled group was found to be .804 ($p < 10^{-16}$), and in the uncontrolled group was found to be .800 ($p < 10^{-16}$). The difference between these was not found to be statistically significant ($p = .868$). ROC curves for the uncontrolled and feedback-controlled groups can be seen in Figure 3.15a and ROC curves for the feedback-controlled group broken down by control threshold can be seen in Figure 3.15b. AUC values within each threshold varied between .874 and .798, and all were found to be significantly different

54

(a)   (b)
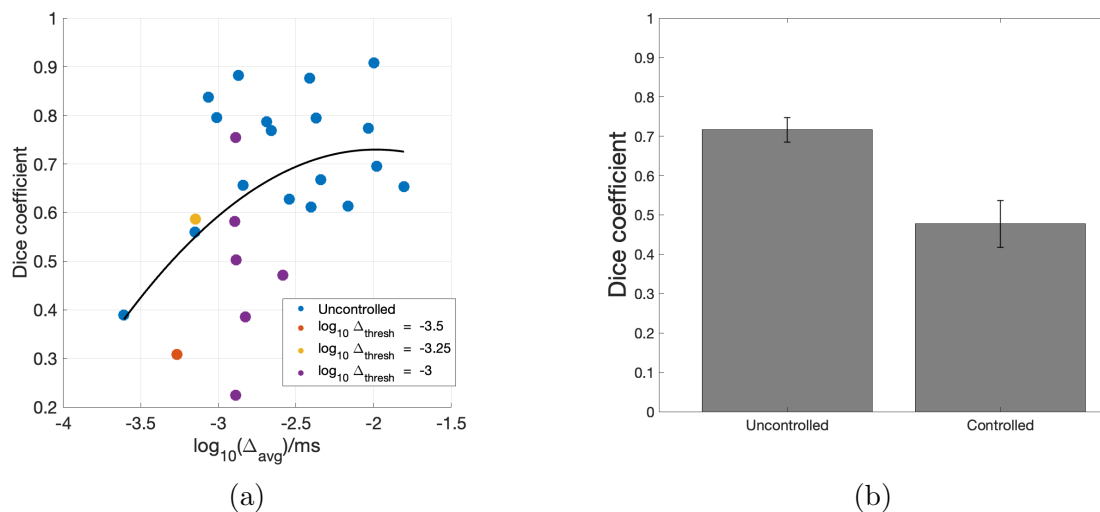
Figure 3.14: Results for Dice coefficients in the preliminary group of feedback-controlled and uncontrolled trials without saline infusion. (a) Scatter plot of log10-scaled average decorrelation within a targeted 15 mm radius ablation zone centered at the needle tip vs. Dice coefficient with overlaid least-squares optimized quadratic fit. (b) Bar plot of mean Dice coefficients in the feedback-controlled and uncontrolled groups, with error bars showing standard error.

(a)   (b)
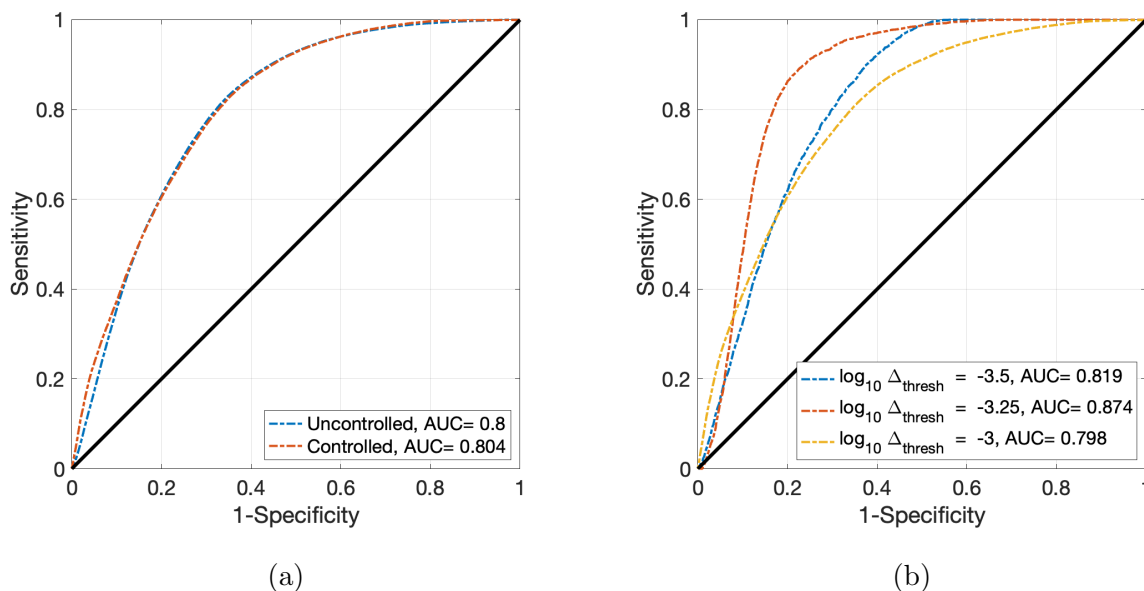
Figure 3.15: Results for prediction of local ablation in preliminary trials without saline infusion ($N = 24$). (a) ROC curve for prediction of local tissue ablation across all uncontrolled ($N = 19$) and feedback-controlled ($N = 8$) trials (b) ROC curves for preliminary trials without saline infusion per control threshold ($\Delta_{\text{thresh}} = -3.5, -3.25, -3$).

from random chance (AUC= .5). A summary of ROC analysis, including the AUC and its associated significance value, across all groups in the preliminary uncontrolled set of trials without saline infusion can be seen in Table 3.1.

	Uncontrolled	Controlled				Combined
Δ_{thresh}	—	–3.5	–3.25	–3	all	—
# Trials	19	1	1	6	8	27
AUC	.800	.819	.874	.798	.801	.813
Z-score	30.39	3.91	7.89	12.94	13.62	37.37
p-value	$< 10^{-16}$	$8.45 \cdot 10^{-5}$	$3.11 \cdot 10^{-15}$	$< 10^{-16}$	$< 10^{-16}$	$< 10^{-16}$

AUC for preliminary uncontrolled and feedback-controlled trials without saline

Table 3.1: Area under the curve for all preliminary uncontrolled ($N = 17$) and controlled trials without saline infusion, with thresholds Δ_{thresh} set to –3.5 ($N = 1$), –3.25 ($N = 1$) and –3 ($N = 6$). Significance is determined by $p < .05$, where p is determined by a sample size adjusted Z-score.

The optimal point of the ROC curve (Δ_{opt}), defined as the point nearest to the upper left corner of the ROC curve, was found to be –3.38 in the feedback-controlled group and –3.15 in the uncontrolled group. The threshold achieving 90% specificity was found to be –2.91 in the feedback-controlled group and –2.45 in the uncontrolled group, with a corresponding sensitivity of 30% and 34%, respectively. Odds plots of sensitivity and specificity vs. decorrelation threshold can be seen in Figure 3.16a for the feedback-controlled group and Figure 3.16b for the feedback-controlled group, where the optimal point and threshold achieving 90% sensitivity are marked with vertical lines.

Tissue sections of a characteristic controlled and uncontrolled trial with corresponding decibel-scaled azimuth-depth B-mode slices with overlaid cumulative $\log_{10} \Delta$/ms maps can be seen in Figure 3.17. Column 1 shows the 4 slices of sectioned tissue histology nearest to the center of ablation for a characteristic uncontrolled trial, and figures in column 2 are the corresponding azimuth-depth B-mode ultrasound slices with overlaid log10-scaled decorrelation for each histology section in column 1. Decorrelation values are shown for values between $\log_{10} \Delta$/ms $= –4$ and $\log_{10} \Delta$/ms $= –1$. Columns 3 and 4 show tissue histology and corresponding B-mode with decorrelation overlaid for a characteristic controlled trial ($\Delta_{\text{thresh}} = –3$). As was typically the case, the uncontrolled

| (a) Uncontrolled trials | (b) Controlled trials |
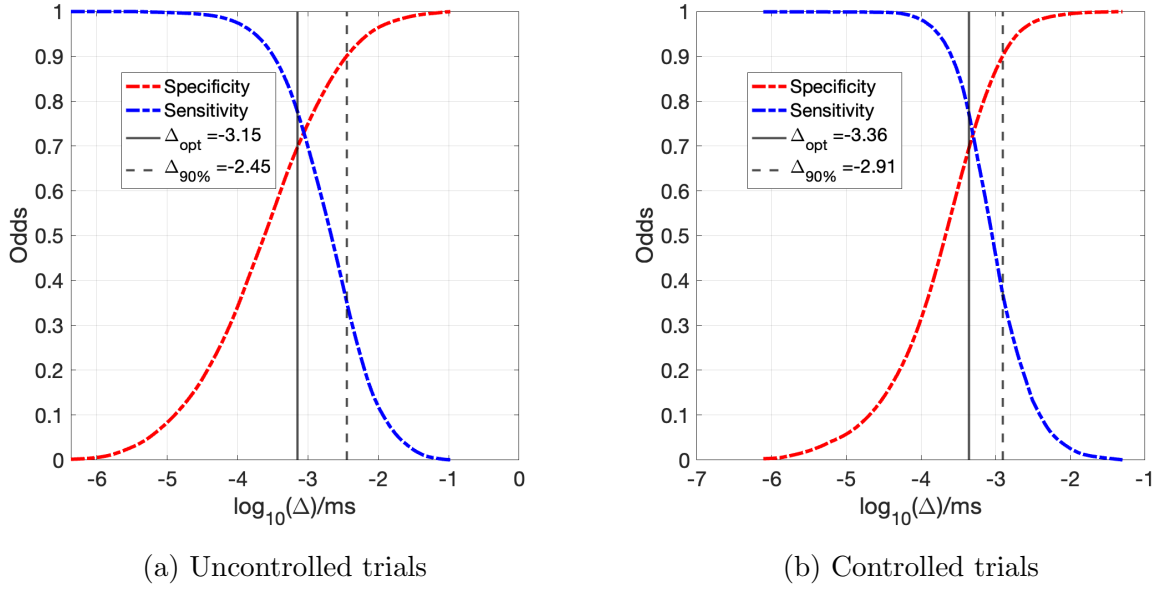
Figure 3.16: Odds plots for (a) uncontrolled and (b) controlled groups in the preliminary set of trials without saline infusion. The solid black vertical line shows the optimal decorrelation value for prediction of local ablation, while the dashed vertical line shows the threshold which achieved 90% sensitivity.

trial had significantly greater decorrelation within the targeted region as well as a much greater ablation volume. Similarly, the conformance between local thermal lesioning and decorrelation magnitude can be seen in these slices.

3.3.1.c   Preliminary feedback-controlled and uncontrolled trials with saline infusion

All ($N = 7$) preliminary feedback-controlled trials with saline infusion were successfully controlled. The log10-scaled control thresholds used in these trials were: $\Delta_{\text{thresh}} = -2.8$ ($N = 2$), -2.5 ($N = 2$), -2.4 ($N = 2$) and -2.2 ($N = 1$). The mean volume within the uncontrolled group with saline infusion ($N = 4$) was found to be 20.705 ± 4.947 (mean $\pm$ standard deviation), which was significantly larger than the mean volume in the feedback-controlled group, which was 8.375 ± 1.383 ($p = 1.24 \cdot 10^{-4}$).

The correlation between log10-scaled spatial average decorrelation within the ablation zone and ablation volume in trials with saline infusion was found to be similar to those without saline infusion, but did not reach statistical significance ($R^2 = .194$,
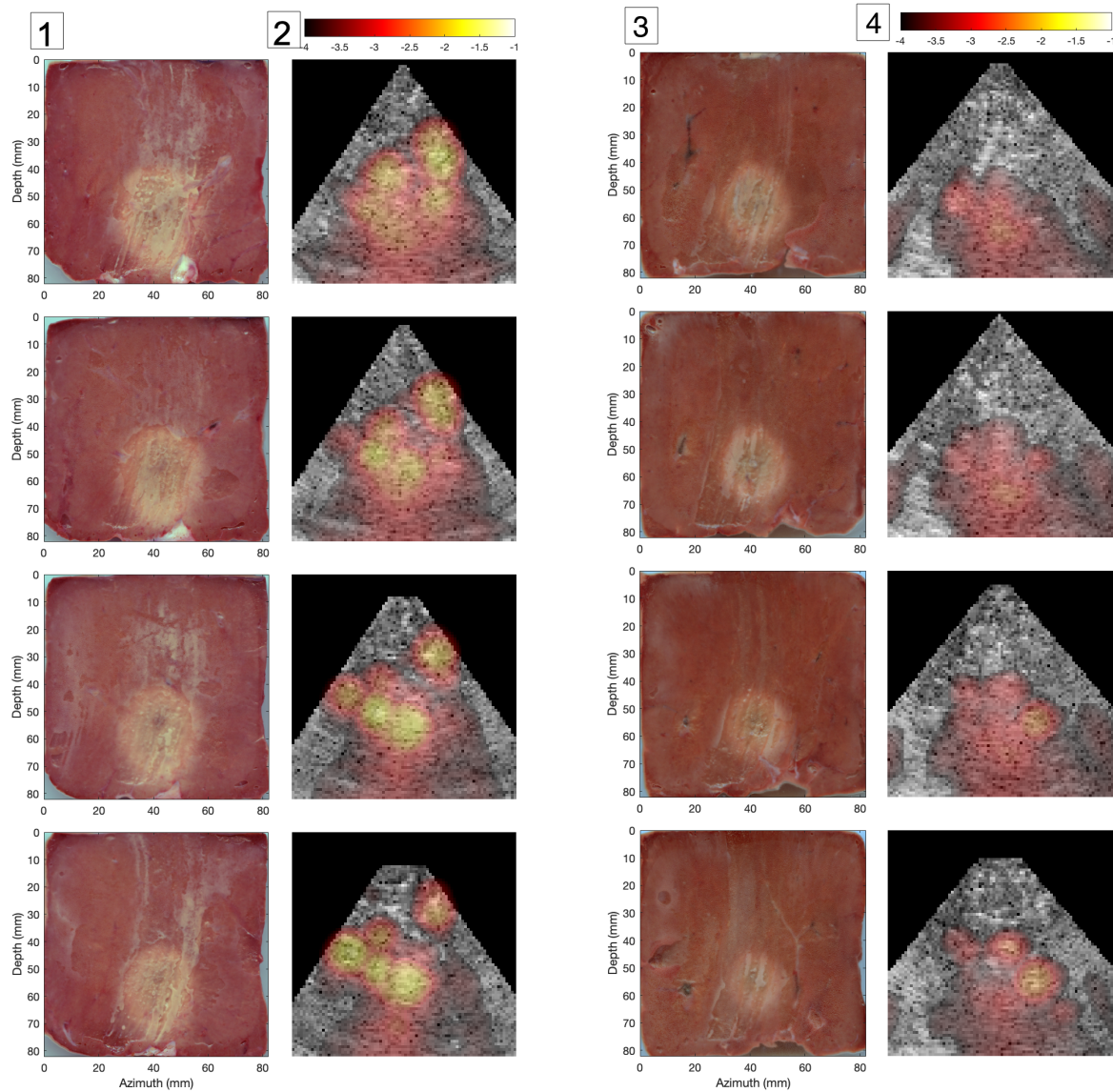
Figure 3.17: Example of tissue histology with corresponding decibel-scaled B-mode slices with overlaid $\log_{10}$-scaled decorrelation per ms. The column marked (1) shows tissue histology for the four tissue slices closest to the needle tip for a characteristic uncontrolled trial in the preliminary uncontrolled group without saline infusion, and the column marked (2) shows an azimuth-depth B-mode plane at the same elevation as each tissue slice in column 1 with overlaid log10-scaled decorrelation maps. Columns (3) and (4) show the same information for a characteristic controlled trial ($\Delta_{\mathrm{thresh}} = -3$).

$p = .176$). A scatter plot of log10-scaled average decorrelation vs. ablation volume with an MSE-optimized linear regression line can be seen in Figure 3.18a.

(a) (b)
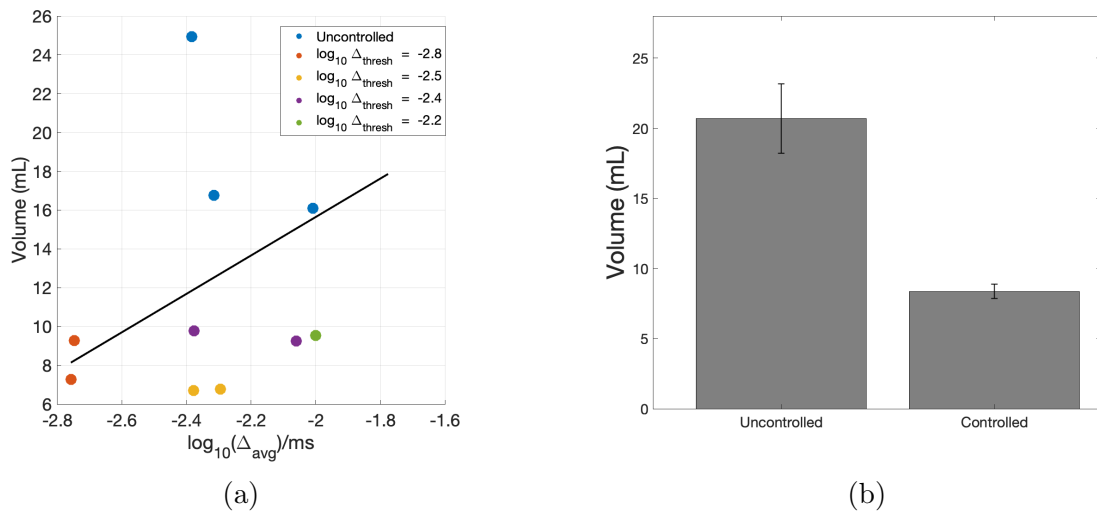
Figure 3.18: Results for total ablation volume in the preliminary group of feedback-controlled and uncontrolled trials with saline infusion. (a) Scatter plot of log10-scaled average decorrelation within a targeted 15 mm radius ablation zone centered at the needle tip vs. total ablation volume with overlaid least-squares optimized linear fit. (b) Bar plot of mean volumes in the feedback-controlled and uncontrolled groups, with error bars showing standard error.

The mean Dice coefficient in the uncontrolled group was $.738 \pm .081$, while the mean in the feedback-controlled group was $.717 \pm .060$. The difference in the mean of the feedback-controlled and uncontrolled groups was not found to be significant ($p = .54$), and the variance under the F-test was also not found to be significant ($p = 63$). A scatter plot of the Dice coefficient vs. log scaled spatial mean decorrelation within the ablation zone is shown in Figure 3.19a.

ROC analysis completed on preliminary trials with saline infusion is summarized in table 3.2. All groups predicted local thermal lesioning significantly more effectively than chance, with AUC values between .795–.879 ($p < 10^{-16}$, all cases).
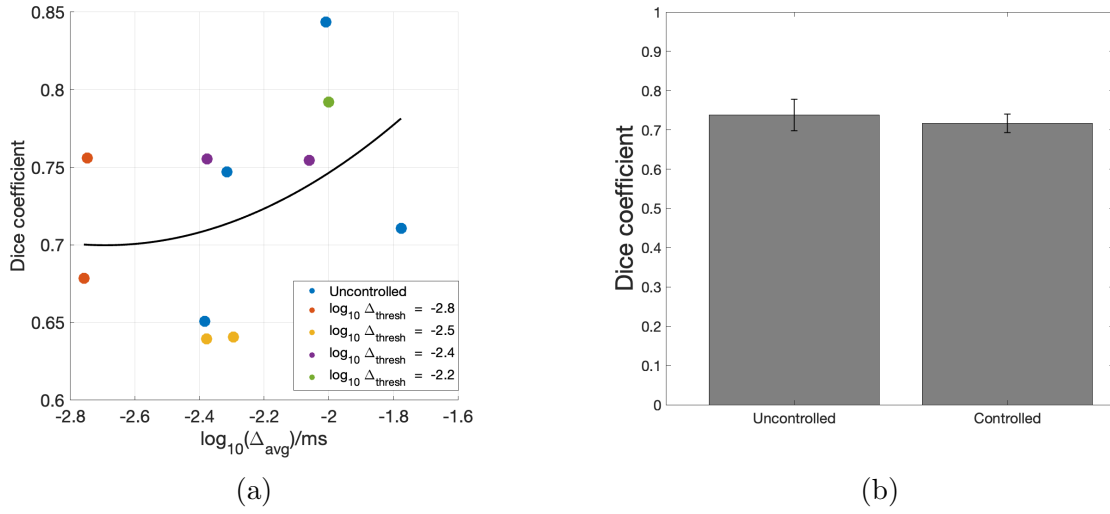
Figure 3.19: Results for Dice coefficients in the preliminary group of feedback-controlled ($N = 7$) and uncontrolled ($N = 4$) trials with saline infusion. (a) Scatter plot of log10-scaled average decorrelation within a targeted 15 mm radius ablation zone centered at the needle tip vs. Dice coefficient with overlaid least-squares optimized quadratic fit. (b) Bar plot of mean Dice coefficients in the feedback-controlled and uncontrolled groups with error bars showing standard error.
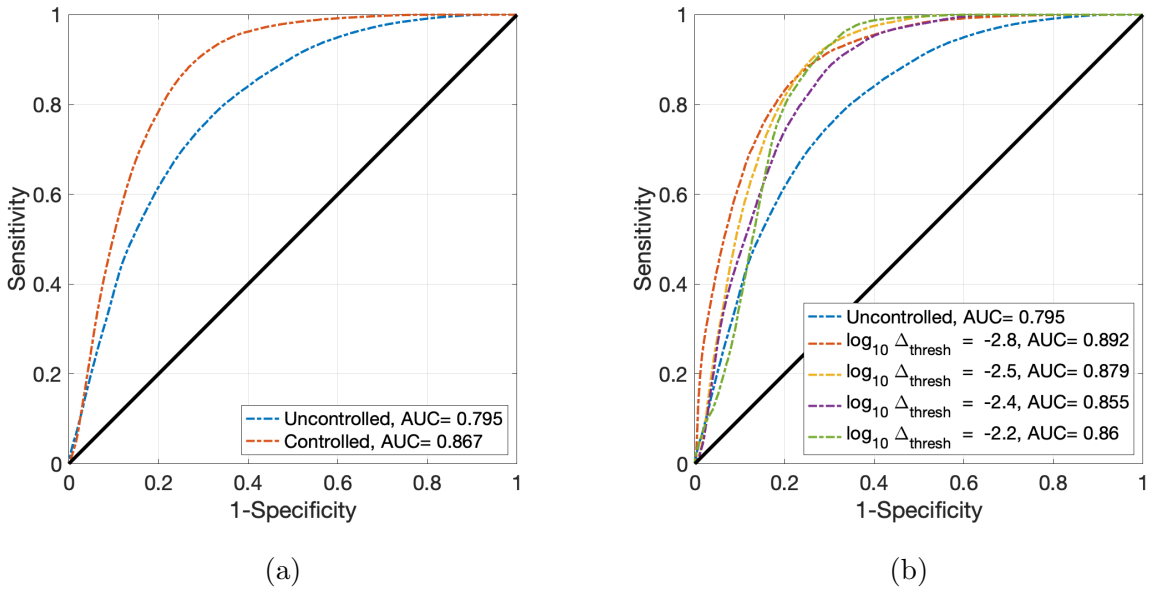
Figure 3.20: Results for prediction of local ablation in preliminary trials with saline infusion ($N = 10$). (a) ROC curve for prediction of local tissue ablation across all uncontrolled ($N = 3$) and feedback-controlled ($N = 7$) trials, with the optimal point for prediction of local ablation ($\Delta_{\text{opt}} = -2.9$) shown in blue and the minimum threshold achieving 90% specificity ($\Delta_{90\%} = -2.3$) shown in black. (b) ROC curves for preliminary trials with saline infusion per control threshold ($\Delta_{\text{thresh}} = -2.8, -2.5, -2.4, -2.2$).

AUC statistics for preliminary trials with saline infusion					
Uncontrolled	Controlled				
Δ_{thresh} —	–2.8	–2.5	–2.4	–2.2	all
# Trials 4	2	2	2	1	7
AUC .795	.892	.879	.855	.859	.867
Z-score 18.39	14.73	12.31	12.66	9.21	32.81
p-value $p < 10^{-16}$	$p < 10^{-16}$	$p < 10^{-16}$	$p < 10^{-16}$	$p < 10^{-16}$	$p < 10^{-16}$

Table 3.2: Area under the curve for all trials with saline infusion. Uncontrolled ($N = 14$) and controlled trials ($N = 18$) with threshold Δ_{thresh} set to –3 ($N = 2$), –2.5 ($N = 2$), –2.4 ($N = 2$) –2.2 ($N = 1$). Statistical significance of the AUC values was determined via a 2-tailed sample size adjusted Z-score.

3.3.2   Analysis of all preliminary trials and control parameter determination

3.3.2.a   Summary

Mean ablation volume in the feedback-controlled and uncontrolled trials with and without saline infusion can be seen in Figure 3.21a. A combined scatter plot of log10-scaled spatial decorrelation within the ROI vs. ablation volume can be seen in Figure 3.21b. These variables had a moderate and statistically significant correlation ($R^2 = .219$, $p = .003$). Uncontrolled trials with saline infusion had a significantly greater ablation volume than those without saline infusion ($p = .026$), as did feedback-controlled trials ($p = .004$), however these were controlled at a range of thresholds between $\log_{10} \Delta_{\text{thresh}} =$ –2.8 and –2.2. The mean spatial decorrelation in the uncontrolled groups, which was $\log_{10} \Delta_{\text{avg}} = -2.11$ for the group with saline infusion and $\log_{10} \Delta_{\text{avg}} = -2.88$ without saline infusion, was also found to be significantly different under a two-sided t-test ($p = .006$).

Similarly, a bar plot for Dice coefficients between trials with and without saline infusion can be seen in Figures 3.22a. The increase in conformance in the saline group is likely due to generally increased ablation volumes arising from more consistent thermal lesioning. A scatter plot of spatial average decorrelation in the ROI vs. Dice coefficient with an MSE optimized quadratic fit can be seen in Figure 3.21b. The quadratic model was found to be significant ($R^2 = .243$, $p = .009$), and shows generally low Dice coefficient values for lower mean decorrelation values, particularly in the feedback-controlled group.
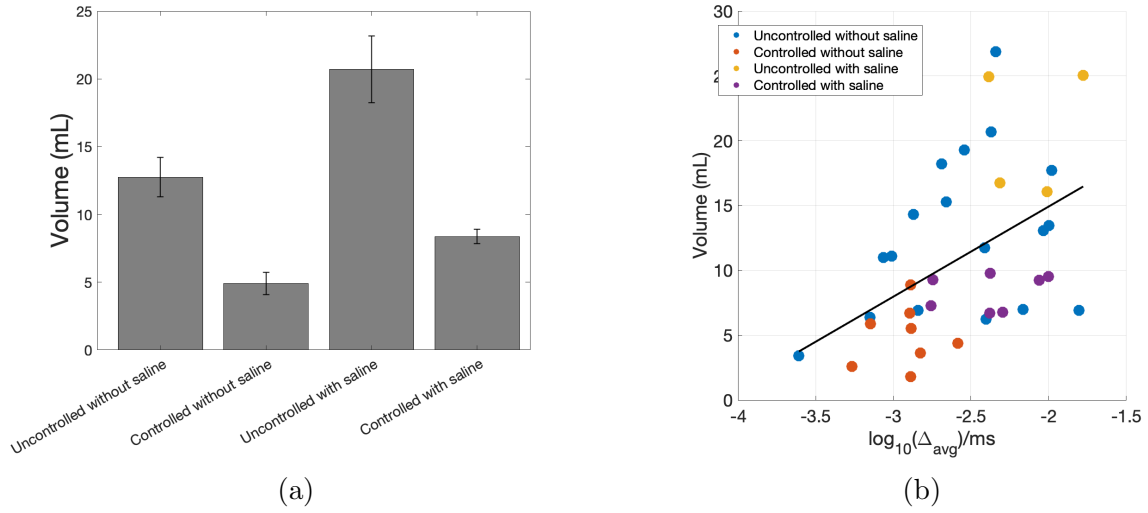
Figure 3.21: Comparison of ablation volumes for feedback-controlled and uncontrolled trials with and without saline infusion. Subfigure (a) shows mean volume across each group and Subfigure (b) shows mean ablation volume for feedback-controlled trials per decorrelation control threshold.
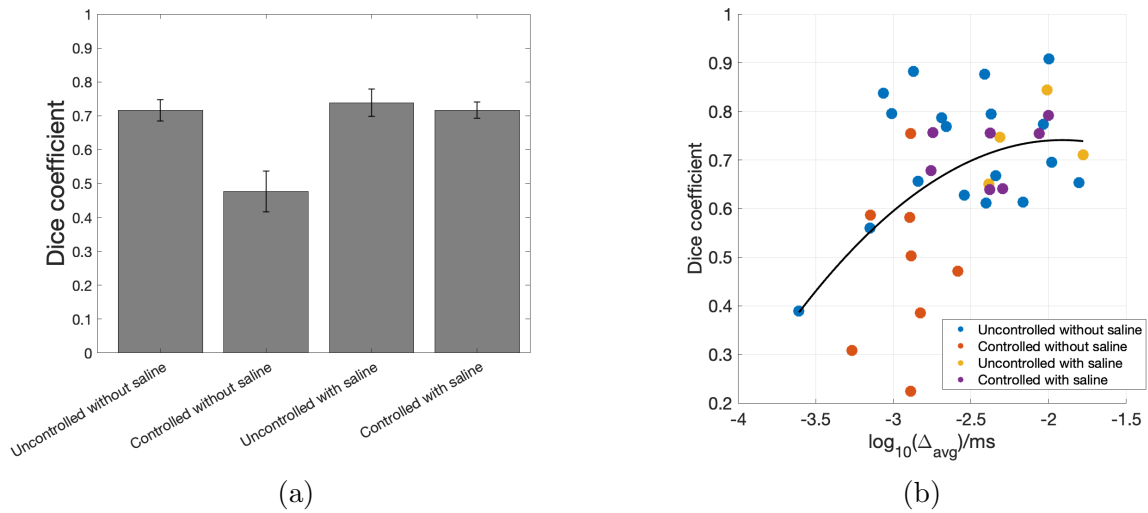
Figure 3.22: Comparison of Dice coefficients for feedback-controlled and uncontrolled trials with and without saline infusion. Subfigure (a) shows mean volume across each group and Subfigure (b) shows mean ablation volume for feedback-controlled trials per decorrelation control threshold.

Considering the significant difference between trials with and without saline infusion, the results within the trials with saline infusion were considered more relevant for threshold determination for the final set of feedback-controlled trials.

3.3.2.b Prediction of local ablation

Across all trials, the optimal threshold for local prediction was found to be –2.49. The ROC curve for all preliminary controlled trials can be seen in figure 3.23a, where the AUC of the ROC curve was found to be .80 ($p < 10^{-16}$).

(a)   (b)
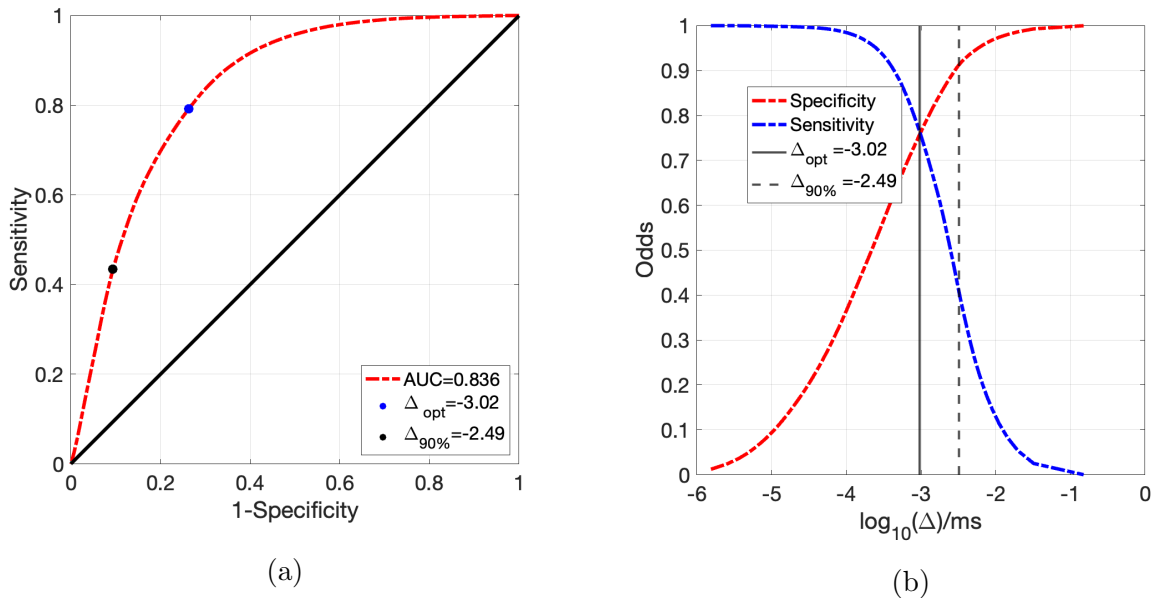
Figure 3.23: Results for prediction of local ablation in all preliminary trials combined ($N = 34$). (a) ROC curve for prediction of local tissue ablation across all preliminary trials, with the optimal point for prediction of local ablation ($\Delta_{\mathrm{opt}} = -3.02$) shown in blue and the minimum threshold achieving 90% specificity ($\Delta_{90\%} = -2.49$) shown in black. (b) Odds plots of sensitivity and specificity per $\log_{10}$ decorrelation threshold with Δ_{opt} and $\Delta_{90\%}$ marked with a solid and dashed vertical line respectively.

Decorrelation values that achieved high specificity and reasonable sensitivity for prediction of local ablation were considered a reasonable starting point for a final feedback control threshold. Odds plots for all preliminary trials in both the feedback-controlled and uncontrolled groups can be seen in Figures 3.24a and 3.24b, where a threshold of –2.41 was found to achieve 90% sensitivity in the uncontrolled group and –2.75 in the controlled group. These had corresponding sensitivites of 37.3% and 50.7% respectively.

(a) Uncontrolled trials · · · · · · · · · · · · (b) Controlled trials
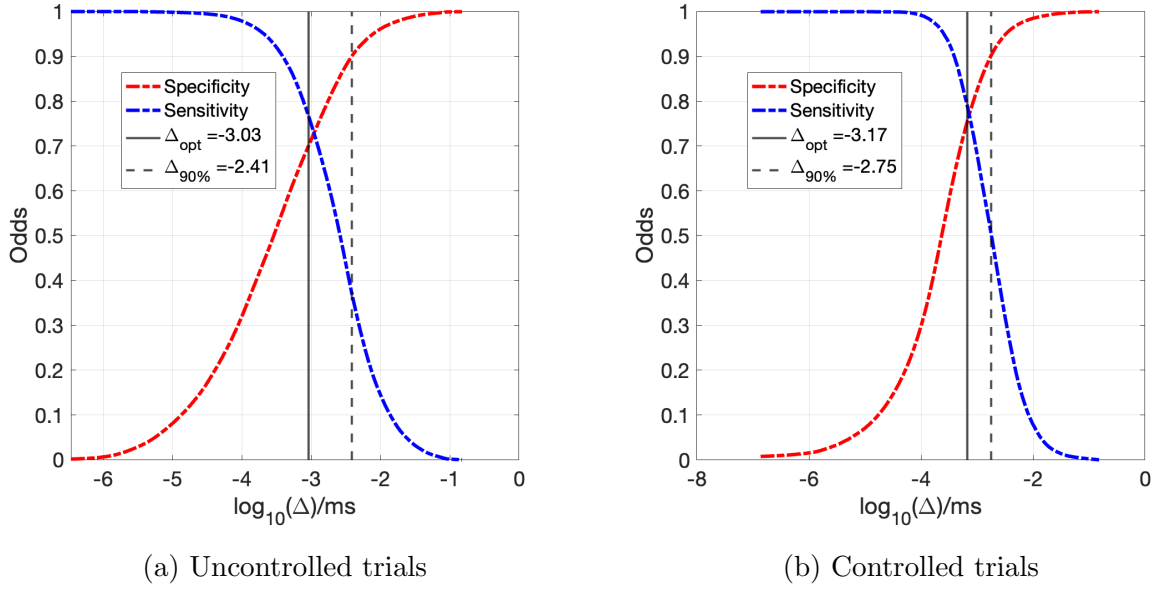
Figure 3.24: Odds plots for (a) uncontrolled and (b) controlled groups in all preliminary trials (both with and without saline infusion). The solid black vertical line shows the optimal decorrelation value for prediction of local ablation, while the dashed vertical line shows the threshold which achieved 90% specificity.

The value for local prediction across all trials was determined to be less relevant to our final controlled trials by the statistically significant difference in thermal lesioning between trials with saline infusion and trials without saline infusion. Instead, local predictive power within the saline trials was considered more relevant for final determination of a control threshold.

Figures 3.25a and 3.25b show the odds plots for only trials with saline infusion, where the threshold achieving 90% specificity in the uncontrolled group was found to be –2.28 and in the feedback-controlled group was –2.56. These had a corresponding sensitivity of 38.2% and 50.4% respectively.

Computed sensitivity and specificity values at Δ_{opt}, $\Delta_{90\%}$, and at the final chosen threshold $\Delta_{\text{thresh}} = -2.2$ for prediction of local ablation via ROC analysis in the uncontrolled, feedback-controlled and combined groups can be seen in table 3.3 for trials without saline infusion, table 3.4 for trials with saline infusion and table 3.5 for all trials combined. As feedback control affected the observed value for $\Delta_{90\%}$, which will be discussed further in section 3.4, the most relevant parameter was the result for uncontrolled

(a) Uncontrolled trials   (b) Controlled trials
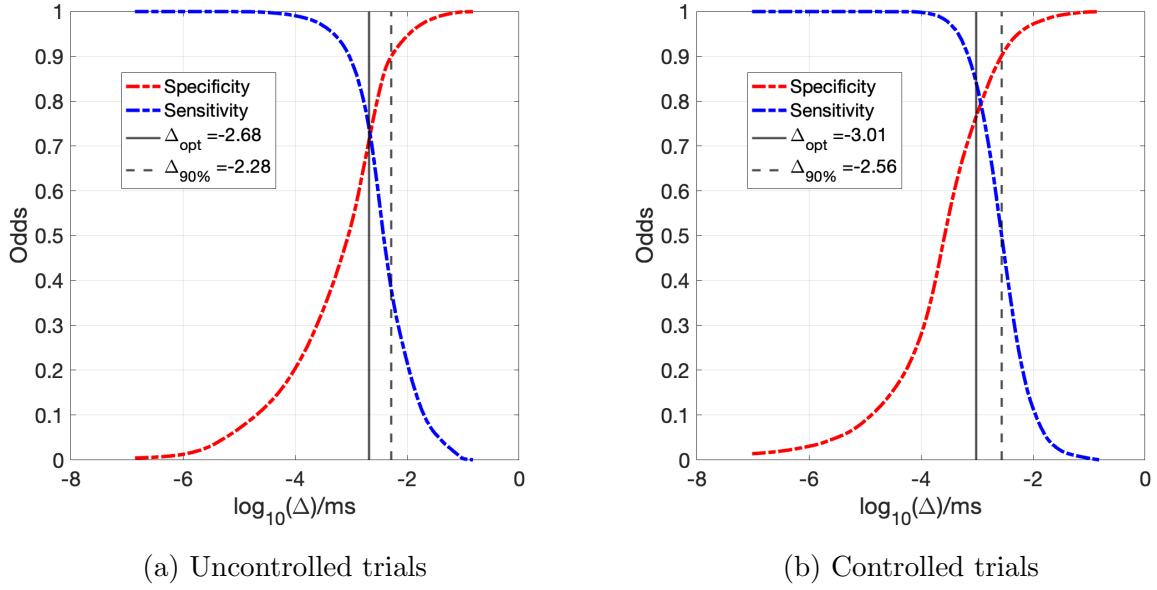
Figure 3.25: Odds plots for (a) uncontrolled and (b) controlled groups in the preliminary set of trials with saline infusion. The solid black vertical line shows the optimal decorrelation value for prediction of local ablation, while the dashed vertical line shows the threshold which achieved 90% specificity.

trials with saline infusion, which was found to have a value of $\Delta_{90\%} = -2.28$, with a corresponding sensitivity of 38.2%.

	Sensitivity and specificity values for preliminary trials without saline infusion								
	Uncontrolled			Controlled			Combined		
	Δ_{opt}	$\Delta_{90\%}$	Δ_{thresh}	Δ_{opt}	$\Delta_{90\%}$	Δ_{thresh}	Δ_{opt}	$\Delta_{90\%}$	Δ_{thresh}
$\log_{10}(\Delta)$	-3.15	-2.45	-2.20	-3.36	-2.91	-2.20	-3.18	-2.60	-2.20
Spec.(%)	69.7	90.0	94.2	69.5	90.0	99.0	71.7	90.0	95.8
Sens.(%)	78.3	35.4	20.5	77.3	37.2	5.3	77.2	41.6	18.2

Table 3.3: Sensitivity and specificity values for preliminary trials without saline infusion. Values are shown for the optimal threshold (Δ_{opt}), minimal threshold achieving 90% specificity ($\Delta_{90\%}$) and threshold chosen for final trials (Δ_{thresh}) for uncontrolled trials, feedback-controlled trials and all trials combined.

3.3.2.c   Prediction of total ablation volume

Sensitivity and specificity values for the prediction of lesion volume via the mean decorrelation within the targeted ROI were computed to further refine the control threshold choice. In all preliminary trials, a threshold of $\Delta_{\mathrm{thresh}} = -2.2$ resulted in a specificity

Sensitivity and specificity values for preliminary trials with saline infusion								
	Uncontrolled			Controlled			Combined		
	Δ_{opt}	$\Delta_{90\%}$	Δ_{thresh}	Δ_{opt}	$\Delta_{90\%}$	Δ_{thresh}	Δ_{opt}	$\Delta_{90\%}$	Δ_{thresh}
$\log_{10}(\Delta)$	–2.68	–2.28	–2.20	–3.01	–2.56	–2.20	–2.85	–2.44	–2.20
Spec.(%)	70.9	90.0	91.5	76.3	90.0	95.7	75.0	90.0	94.4
Sens.(%)	74.5	38.2	32.6	84.3	50.4	21.3	80.3	47.3	28

Table 3.4: Sensitivity and specificity values for preliminary trials without saline infusion. Values are shown for the optimal threshold (Δ_{opt}), minimal threshold achieving 90% specificity ($\Delta_{90\%}$) and threshold chosen for final trials (Δ_{thresh}) for uncontrolled trials, feedback-controlled trials and all trials combined.

Sensitivity and specificity values for all preliminary trials								
	Uncontrolled			Controlled			Combined		
	Δ_{opt}	$\Delta_{90\%}$	Δ_{thresh}	Δ_{opt}	$\Delta_{90\%}$	Δ_{thresh}	Δ_{opt}	$\Delta_{90\%}$	Δ_{thresh}
$\log_{10}(\Delta)$	–3.03	–2.41	–2.20	–3.17	–2.75	–2.20	–3.09	–2.53	–2.20
Spec.(%)	70.0	90.0	93.7	75.3	90.0	97.5	72.8	90.0	95.4
Sens.(%)	76.8	37.3	23.8	79.1	50.7	15.1	78.0	44.2	21.6

Table 3.5: Sensitivity and specificity values for preliminary trials without saline infusion. Values. are shown for the optimal threshold (Δ_{opt}), minimal threshold achieving 90% specificity ($\Delta_{90\%}$) and threshold chosen for final trials (Δ_{thresh}) for uncontrolled trials, feedback-controlled trials and all trials combined.

for prediction of 80% of the targeted ablation zone of 78% and a sensitivity of 50%. The same analysis was completed on preliminary trials with saline infusion only, as these are the conditions which would be used in the final set of feedback-controlled trials. For the group of preliminary trials with saline infusion, a threshold of $\Delta_{\text{thresh}} = -2.2$ resulted in a specificity of 77% and sensitivity of 100%.

3.3.2.d Threshold selection

Results within the preliminary group of trials were used to determine a range of reasonable values for the final selected control threshold. Analysis was completed on all trials together, as well as separately for trials with and without saline infusion, as well as with or without feedback control. Trials with saline infusion were considered more relevant for our final control parameter determination, as there was a significant difference in lesioning characteristics and decorrelation maps in trials with saline infusion compared to those without. Prediction of local ablation in the feedback-controlled groups was also affected by the choice of control threshold, and was thus considered less relevant for parameter selection based on local ablation prediction.

Among all uncontrolled preliminary trials, a threshold value of $\log_{10} \Delta_{\text{thresh}} = -2.2$ resulted in prediction of local ablation with specificity 93.7% and sensitivity 23.8%. For full volume ablation, using both feedback-controlled and uncontrolled trials, a threshold of –2.2 resulted in a 90% ablation volume specificity of 79% and sensitivity of 30%, and for 80% ablation had a specificity of 78% and sensitivity of 50%.

In the uncontrolled group with saline infusion, a threshold of –2.2 resulted in a local ablation prediction specificity of 91.5% and sensitivity of 32.6%. For 80% ablation, a value of –2.2 had a specificity of 72% and a sensitivity of 50%. For 90% ablation specificity at -2.2 was 77% and sensitivity was 100%.

A threshold of –2.2 thus provided a high specificity for prediction of local ablation and total volume ablation, with reasonable sensitivity.

3.3.3 Final feedback-controlled trials

3.3.3.a Analysis of tissue lesioning in final trials

Results for final uncontrolled ($N = 11$) and controlled ($N = 11$) trials were analyzed to determine the efficacy of 3D echo-decorrelation based feedback control. All 11 trials in the controlled group were successfully controlled, with an average total treatment time of 5.36 minutes (maximum of 7.19 minutes and minimum of 3.55 minutes, $\sigma = 1.23$). Treatment followed a similar course in most procedures, with generally rapidly increasing cumulative decorrelation occurring within 30–40 seconds of reaching the target temperature. The target temperature was reached in 1.28 ± 0.046 minutes in the uncontrolled group and 1.26 ± 0.031 in the controlled group. In some cases, a high level of decorrelation was registered early on, possibly caused by air bubbles within the tissue. A plot showing cumulative and instantaneous decorrelation in the 30 mm diameter ROI, along with temperature and impedance readings from the RF generator, of a representative controlled and uncontrolled trial can be seen in Figures 3.26b and 3.26a respectively.

The mean ablation volume in the uncontrolled group was 26.08 ± 5.03mL (mean±standard deviation), while the mean ablation volume in the controlled group was 10.26 ± 3.14mL. Volume was found to be normally distributed under the Shapiro-Wilk test for the uncontrolled group (W=0.93, p=.42) and controlled group (W=0.94, p=0.39), indicating the validity of non-parametric statistical tests. The difference in the mean volume between the two groups was found to be statistically significant ($p < .05$) under the two-sided Student's t-test ($p < 10^{-16}$). However, the difference in variance between the two groups was not found to be significant ($p < .05$) under the two-sample F-test ($p = 2.6 \cdot 10^{-2}$).

Geometric conformance to the ideal targeted volume, as measured by the Sorenson-Dice coefficient between the segmented mask and an ideal sphere centered at the needle tip, was found to be 0.674 ± 0.09 for the uncontrolled group and 0.752 ± 0.06 for the controlled group. Both groups were found to be normally distributed under the Shapiro-Wilk test. Under a two-sided Student's t-test the mean was found to be significantly

(a) Example uncontrolled trial
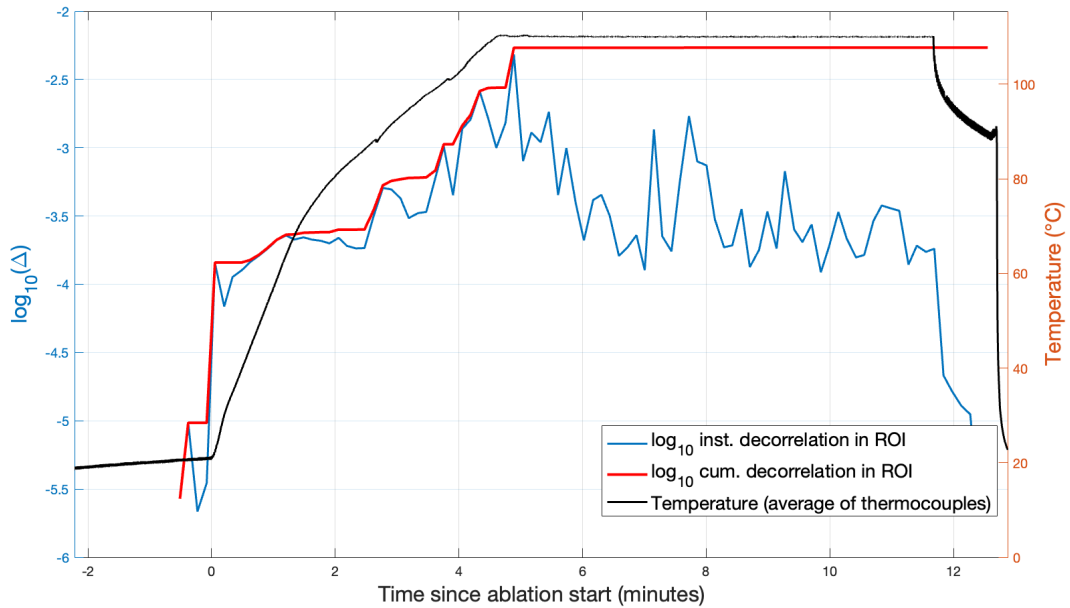
(b) Example controlled trial
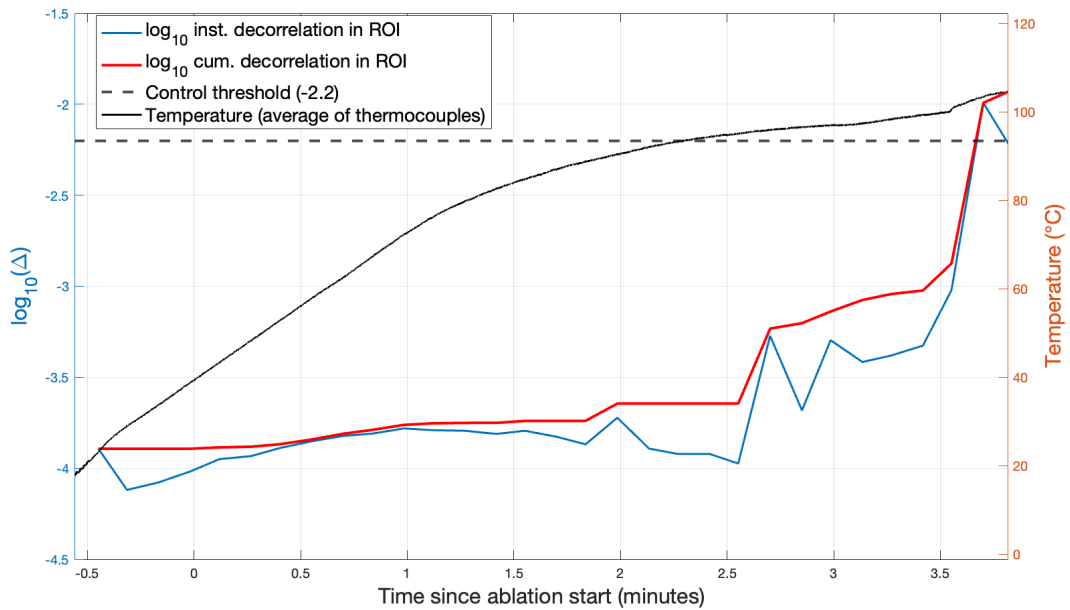
Figure 3.26: Time series of the spatial average instantaneous and cumulative decorrelation within the targeted 15 mm radius spherical ROI with the mean temperature recorded at the RF probe's thermocouples. The x axis shows time since RF treatment started in minutes. Subfigure (a) shows a representative uncontrolled trial, where the RF generator was set to ablate for a 7 minute ablation time at the targeted temperature (110 °C). Subfigure (b) shows a representative feedback-controlled trial, where the treatment was stopped early upon the spatial average cumulative decorrelation reaching the control threshold $\Delta_{\text{thresh}} = -2.2$.

greater in the controlled group ($p = .024$), but the variance under the F-test was not found to be statistically significant ($p = .196$).

Ablation rate was likewise found to be normal under the Shapiro-Wilk test for both the uncontrolled ($W = 0.874$, $p = 0.067$) and controlled groups ($W = 0.947$, $p = 0.610$). The mean value for ablation rate was negligibly different between each group, with the uncontrolled trials having a rate of 1.86 ± 0.535 mL/minute and the uncontrolled trials having a rate of 2.04 ± 0.411 ml/minute. The difference in means as measured by a two-sided t-test was not found to be significantly different ($p = .359$), likewise under the two sample F-test the variance was also not significantly different ($p = .252$). Bar plots of mean ablation volume, Dice coefficient and ablation rate with error bars shown as standard error can be seen in Figure 3.27, and the related statistics can be seen in Table 3.6.

Ablation statistics for the final group of feedback-controlled and uncontrolled trials				
	Uncontrolled	Controlled	t-test	F-test
Volume (mL)	26.8 ± 5.026	10.256 ± 3.140	$4.2 \cdot 10^{-9}$	.138
Dice coefficient	$.674 \pm .09$	$.752 \pm .060$	.024	.196
Ablation rate (mL/min)	$2.044 \pm .369$	$1.8632 \pm .535$	.359	.252

Table 3.6: Statistics for volume, Dice coefficient and ablation rate (mean $\pm$ standard deviation) with corresponding p-values for two sided t-test for equivalence of mean and F-test for equivalence of variance between groups. For both the t-test and F-test the null hypothesis was rejected if $p < .05$.

The relationship between average decorrelation within the ROI and resultant ablation volume and Dice coefficient was analyzed via linear regression. Figure 3.28.a shows a scatter plot of log10-scaled spatial average decorrelation within the ROI vs. the ablated volume in the final set of trials. A modest, but statistically significant, correlation between the spatial mean decorrelation and volume was observed ($R^2 = .26$, $p = .0124$). Feedback-controlled trials showed a less significant relationship between spatial average decorrelation and ablation volume, with higher decorrelation values being associated with

(a) Volume

(b) Dice coefficient
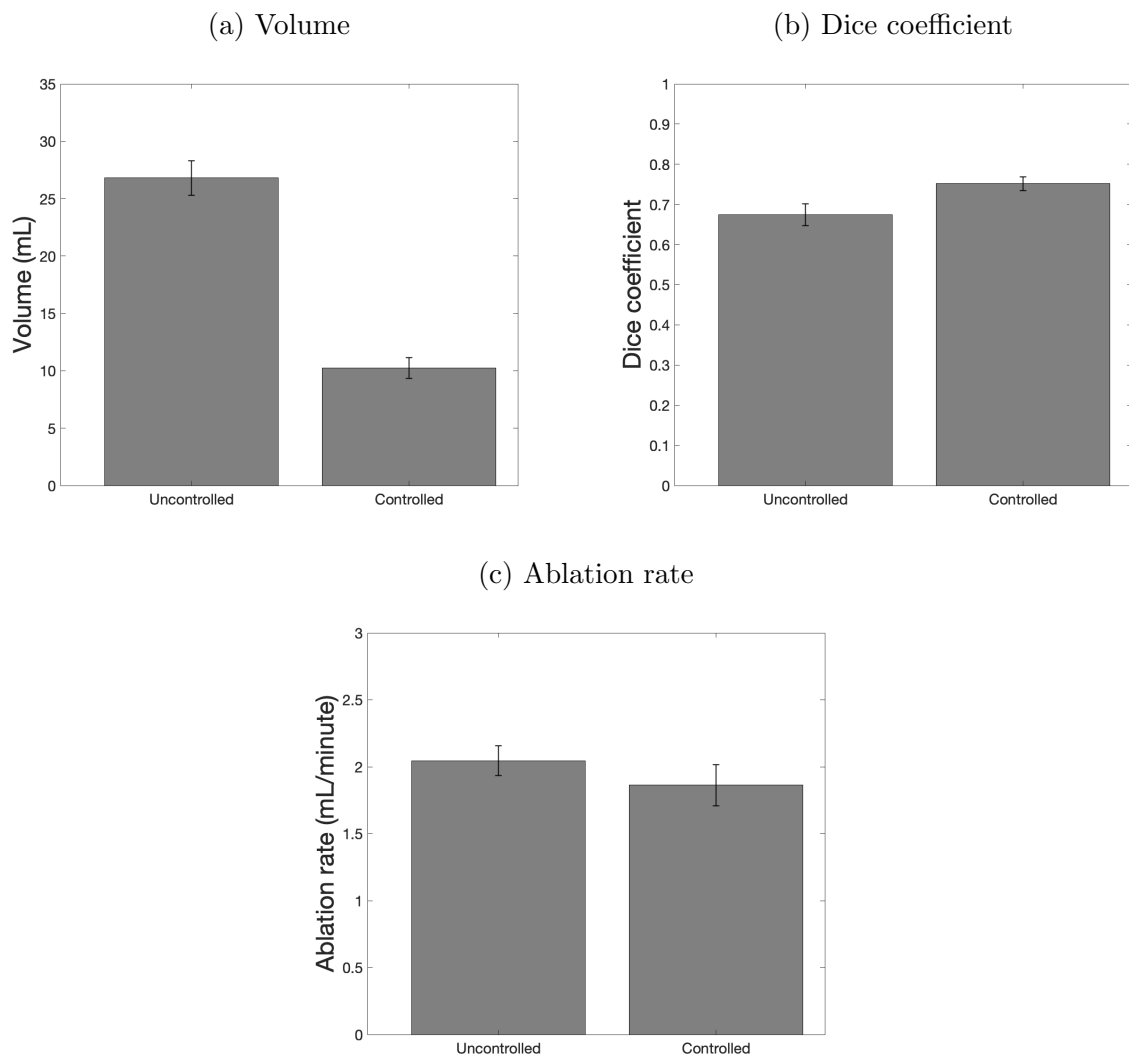
(c) Ablation rate

Figure 3.27: Bar plots of lesioning results in the final group of feedback-controlled and uncontrolled trials. Bars show the mean and standard error of (a) ablation volume, (b) Dice coefficient and (c) ablation rate for controlled and uncontrolled trials.

lower volumes. This effect likely arose as a result of high localized decorrelation events triggering early cessation of treatment in some controlled trials.

3.3.3.b Prediction of local ablation in the final set of trials

ROC curves for the prediction of local ablation via echo decorrelation in the feedback-controlled and uncontrolled groups can be seen in Figure 3.29. Cumulative echo decorrelation predicted ablation significantly better than chance (AUC=.5) in both groups, with an AUC of 0.807 ($p < 10^{-16}$) in the uncontrolled group and 0.836 ($p < 10^{-16}$) in the feedback-controlled group. The difference between the two groups was found to be significantly different under the sample-size adjusted z-test ($z = 2.04$, $p = .041$), indicating a slightly improved predictive ability of local decorrelation for the controlled group. A summary of statistical results for the AUC, sample size adjusted Z-score and p-values can be seen in Table 3.7.

Post-hoc analysis was completed on the $\Delta_{90\%}$, Δ_{opt} and Δ_{thresh} for the final set of trials. The optimal threshold for 90% sensitivity across all final trials was found to be –2.19, which was very close to the selected control threshold of –2.2. In uncontrolled trials, the threshold achieving 90% specificity was found to be –2.13, which had a corresponding sensitivity of 39%. In controlled trials, the threshold achieving 90% specificity was –2.26, with a corresponding sensitivity of 45.2%. A summary of these results can be seen in Table 3.8.
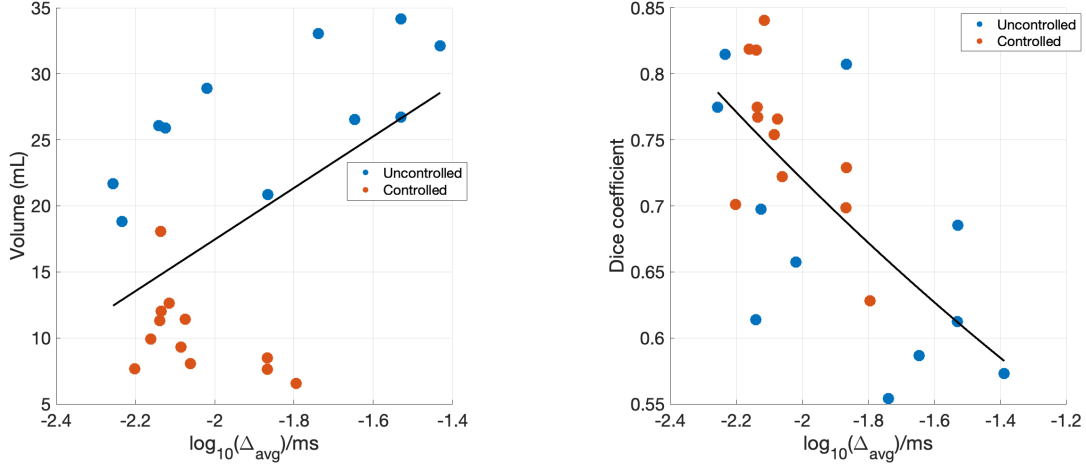
Figure 3.28: Scatter plots of spatial average decorrelation vs. ablation geometry values with MSE-optimized regression lines. Subfigure (a) shows results of linear regression of the spatial average decorrelation within the targeted ROI vs. ablation volume. Subfigure (b) shows results of quadratic regression on Dice coefficient vs. decorrelation.

AUC in final controlled and uncontrolled groups		
	Uncontrolled	Controlled
# Trials	11	11
AUC	.807	.836
Z-score	35.03	29.12
p-value	$p < 10^{-16}$	$p < 10^{-16}$
	Between groups	
Z-score, p-value	2.04, $p = .041$	

Table 3.7: Computed area under the curve values for all trials in the final controlled ($N = 11$) and uncontrolled ($N = 11$) groups. Values for significance testing of the AUC vs. chance (AUC=.5) are shown as the sample size adjusted Z-score with its corresponding p-value. Significance testing between the AUCs of both groups is shown in the bottom column.

	Sensitivity and specificity values for final trials								
	Uncontrolled			Controlled			Combined		
	Δ_{opt}	$\Delta_{90\%}$	Δ_{thresh}	Δ_{opt}	$\Delta_{90\%}$	Δ_{thresh}	Δ_{opt}	$\Delta_{90\%}$	Δ_{thresh}
$\log_{10}(\Delta)$	−2.51	−2.13	−2.20	−2.91	−2.26	−2.20	−2.74	−2.19	−2.20
Spec.(%)	73.3	90.0	88.0	74.5	90.0	90.1	73.1	90.0	89.8
Sens.(%)	70.9	45.4	50.7	79.1	45.2	41.9	77.8	47.9	44.3

Table 3.8: Sensitivity and specificity values for uncontrolled ($N = 11$) and controlled ($N = 11$) final trials. Values are shown for the optimal threshold (Δ_{opt}), minimal threshold achieving 90% specificity ($\Delta_{90\%}$) and threshold chosen for final trials (Δ_{thresh}) for the uncontrolled and feedback-controlled groups as well as both groups combined.

(a) Controlled

(b) Uncontrolled
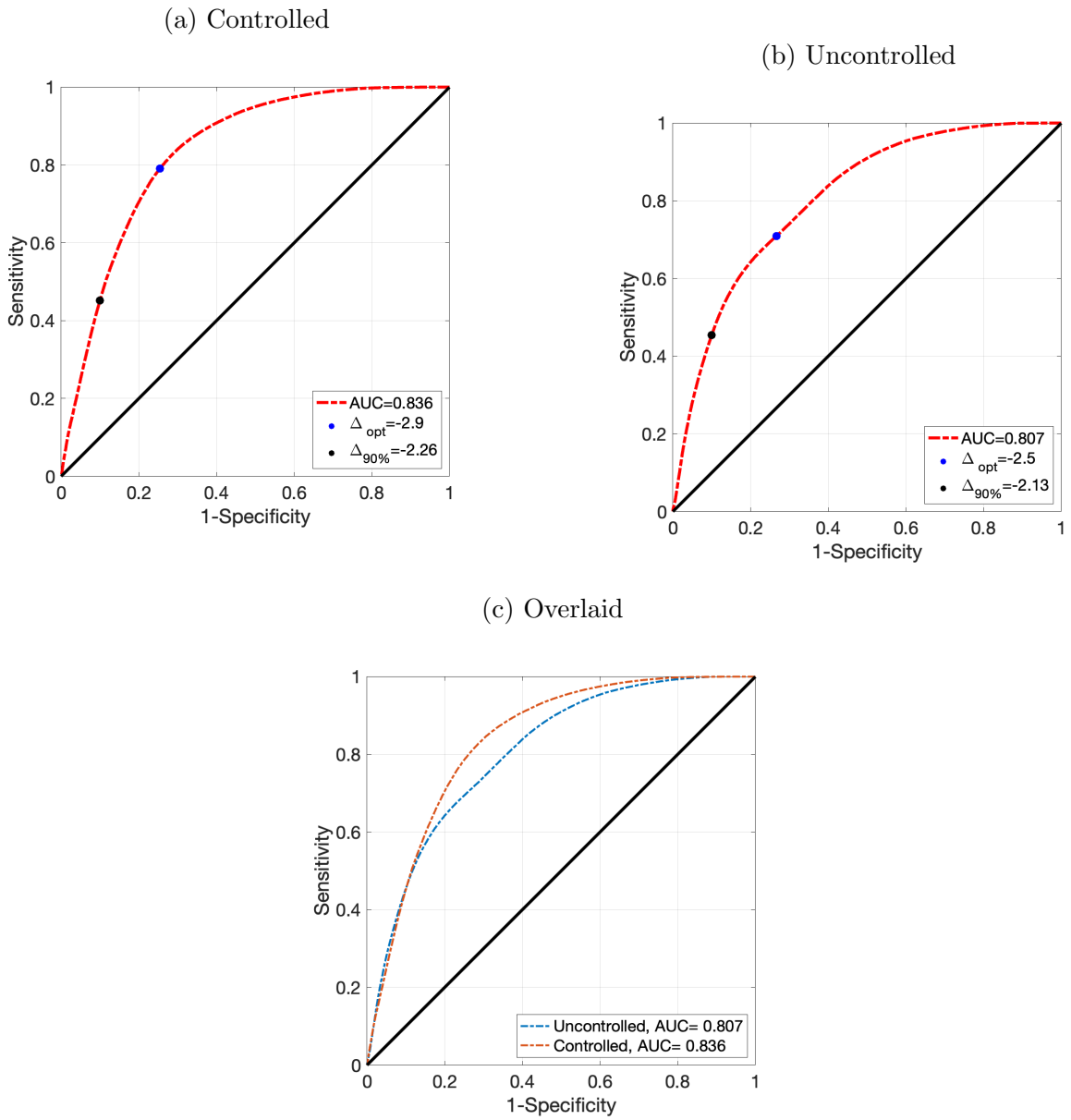
(c) Overlaid

Figure 3.29: ROC curves for (a) uncontrolled trials, (b) controlled trials and (c) both sets overlaid. Optimal thresholds for local ablation, as well as the threshold used in controlled trials, are shown in subfigures (a) and (b). (*$p < 10^{-16}$, **$p < 10^{-16}$)

| (a) Uncontrolled | (b) Controlled |
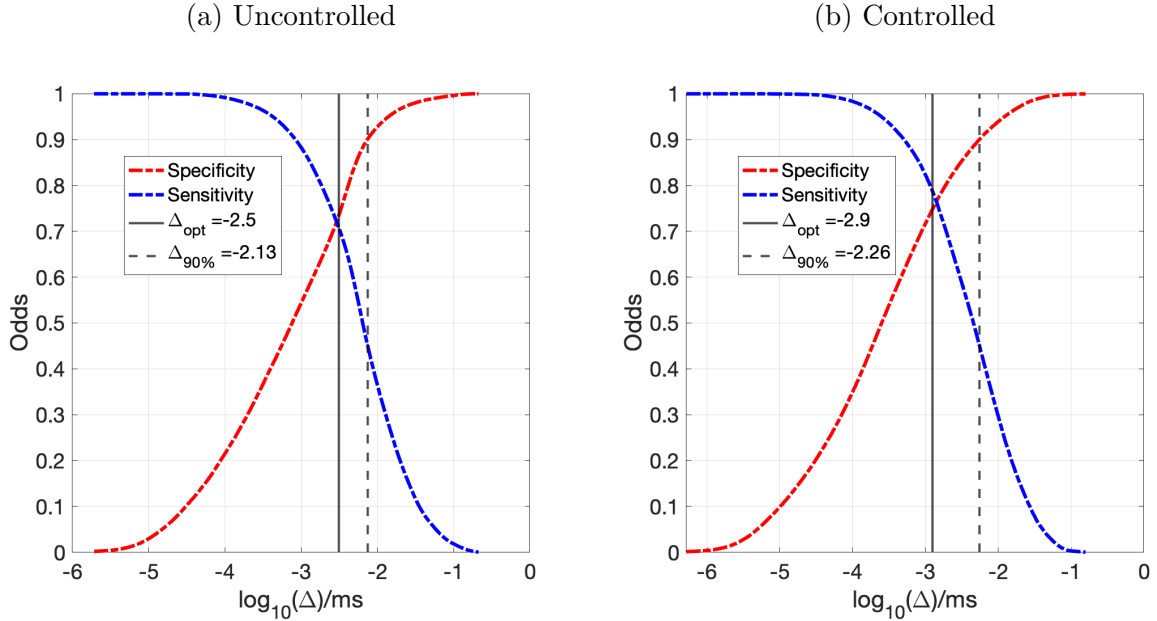
Figure 3.30: Odds plots for uncontrolled (a) and controlled (b) groups in the final group. The solid black vertical line shows the optimal decorrelation value for prediction of local ablation, while the dashed vertical line shows the threshold chosen for controlled trials (-2.2).

3.4   Discussion

This chapter detailed our efforts to create a real-time feedback control methodology to optimize RF thermal lesioning in *ex vivo* bovine liver based on 3D echo decorrelation imaging. Our method was to create a bang-bang type controller which stops the thermal treatment when the spatial mean of the cumulative decorrelation map within our targeted region exceeded a set threshold. All feedback-controlled trials $(N = 27)$, including both the preliminary $(N = 16)$ and final groups $(N = 11)$, were successfully controlled. That is, in all feedback-controlled trials, the spatial average decorrelation, $\hat{\Delta}_{\mathrm{avg}}$, within the ROI exceeded the control threshold, Δ_{thresh}, and the procedure was stopped early relative to the device's default temperature-controlled behavior. Performance in the prediction of local ablation and total thermal lesioning was then evaluated by creating a 3D binary mask of tissue ablation. This mask was used to assess the relationship between local decorrelation at a particular voxel, the relationship between the spatial mean decorrelation within the targeted ROI and the total ablation volume, and the differences between

feedback-controlled and uncontrolled trials in terms of lesion volume, ablation rate and the Dice coefficient between the observed ablation geometry and the targeted ROI.

In our final set of feedback-controlled trials with a constant control threshold ($\log_{10} \Delta_{\mathrm{thresh}} = -2.2$), we found that feedback control resulted in thermal lesions that more closely matched the targeted ablation zone, as measured by the Sorenson-Dice coefficient ($.752\pm.06$ vs. $.674\pm.09$, $p = .024$). Ablated volumes were also significantly smaller in the feedback-controlled group compared to the uncontrolled group (10.25 ± 3.14 mL vs 26.80 ± 5.03 mL, $p = 4.2 \cdot 10^{-9}$). However, we did not find a significant difference in the ablation rate ($p = .359$), the variance in ablation volume ($p = .138$) or the variance in Dice coefficient ($p = .196$). The greater Dice coefficient can be attributed to less ablated tissue outside of the targeted region in the feedback-controlled group, as the uncontrolled group often resulted in substantial treatment outside of the ROI.

In contrast with the final set of trials, the preliminary group of feedback-controlled trials showed worse conformance to the targeted ablation zone when compared to the uncontrolled group ($.589 \pm .18$ vs. $.721 \pm .124$). This difference was found to be more substantial for the trials without saline infusion ($.477 \pm .17$ vs. $.717 \pm .133$) than those with saline infusion ($.717 \pm .06$ vs. $.738 \pm .081$). The poorer Dice coefficient in the trials without saline infusion was the result of lower overall lesion volumes compared to those with saline infusion (4.92 ± 2.31 mL vs. 8.37 ± 1.38 mL). The smaller lesion volumes likely arose out of both a lower control threshold (log10-decorrelation per ms thresholds were between -3.5 and -3 for the group without saline infusion, and between -2.8 and -2.2 for the group with saline infusion), and the effect of saline infusion itself. Considering only the uncontrolled trials in both the preliminary and final groups, which would not be affected by the difference in control thresholds, thermal lesion volume was significantly greater in the group with saline infusion compared to that without (25.18 ± 5.58 mL vs. 12.75 ± 6.17 mL, $p = 1.18 \cdot 10^{-6}$), and the trials with saline infusion also had a greater mean decorrelation within the ROI ($\Delta_{\mathrm{avg}} = -2.34$ vs. -1.83). A figure showing lesion volume vs. average decorrelation per ms within the targeted ROI is shown in figure 3.31. There was a significantly stronger correlation between $\hat{\Delta}_{\mathrm{avg}}$ and lesion volume in the

group with saline infusion ($R^2 = .417$, $p = .009$) than the group without ($R^2 = .097$, $p = .208$).
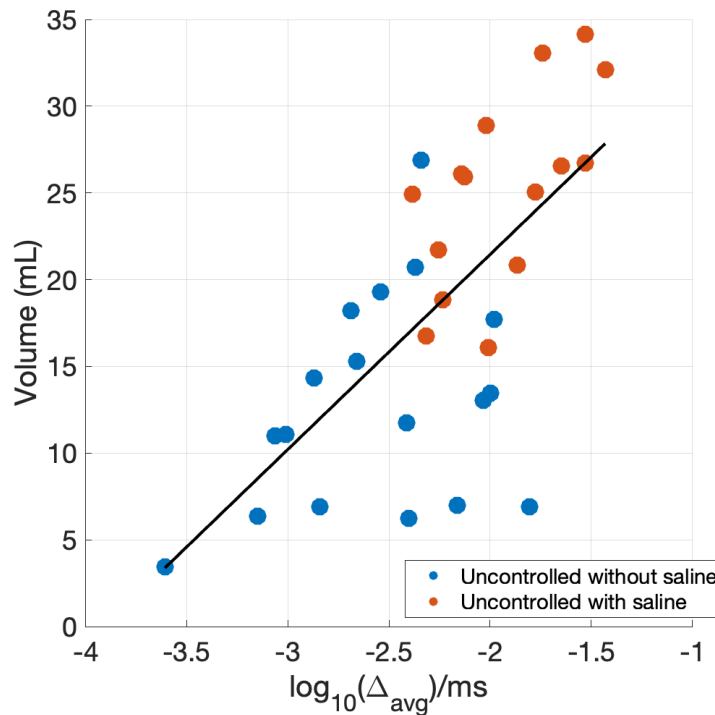
Figure 3.31: Lesion volume vs. mean log10-decorrelation per ms within the targeted ROI for all uncontrolled trials with and without saline infusion.

Differences in thermal lesioning and decorrelation between the groups with and without saline infusion can be partially explained by differences in the observed electrical impedance behavior during those trials. Figure 3.32a shows electrical impedance measured by the RFA needle over time for a characteristic uncontrolled trial without saline infusion, while figure 3.32b shows a trial with saline infusion. In the saline group, nearly all trials showed monotonically decreasing electrical impedance, while in the group without saline, impedance often increased as the trial progressed. This is consistent with clinical recommendations for the use of saline infusion, which is meant to offset the effect of impedance spikes from charred regions of tissue. This effect could have been the limiting factor for lesion size in the trials without saline infusion, which tended to be much smaller.

The small average lesion volume in the feedback-controlled group suggested that the chosen threshold in those trials was too low. As a result, subsequent trials with
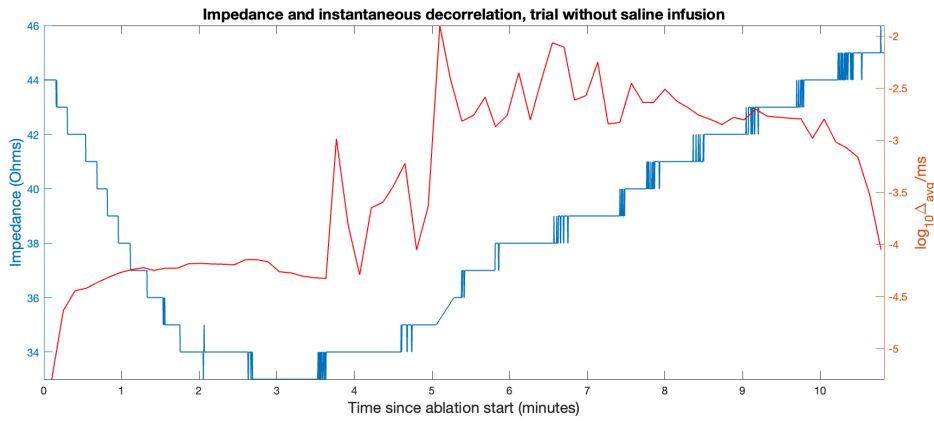
(a)
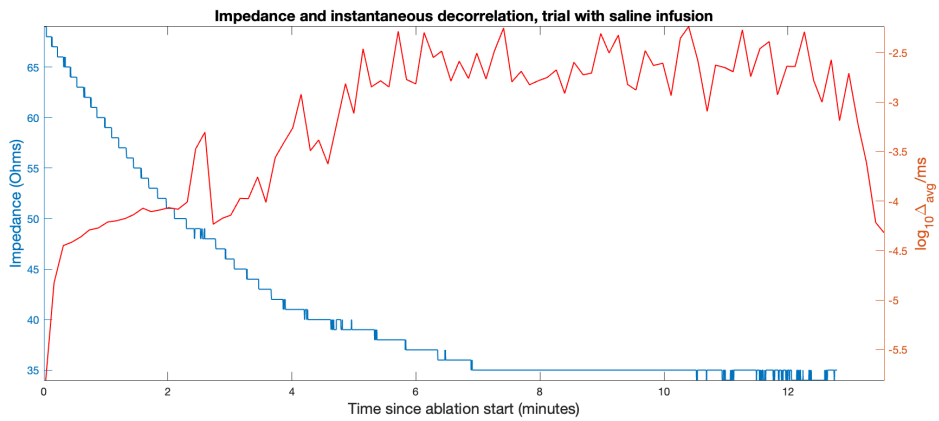
(b)

Figure 3.32: Impedance measured at the ablation needle plotted with mean log10 scaled instantaneous decorrelation for characteristic uncontrolled trials without saline infusion (a) and with saline infusion (b).

saline infusion used a higher control threshold. The threshold was continuously increased throughout the preliminary trials to allow for a greater lesion size, as lesion volumes were substantially smaller than the targeted ROI at lower control thresholds.

The trials with saline infusion had a much greater volume of treated tissue outside of the targeted ablation zone when compared to the feedback-controlled trials, which resulted in a lower Dice coefficient for that group.

All groups within this study showed favorable performance in the prediction of local lesioning, with AUCs between .73 and .84, all of which were determined to be significant. These results are similar to those found in previous studies of *ex vivo* RFA ablation monitoring, such as a study by Mast *et al.* [74] ($N = 9$) which reported a value of .85 and a study by Subramanian *et al.* which reported a value of .919 ($N = 15$) [91]. This is notable because our study did not use ensemble averaging and had a much lower spatial resolution. The effective number of samples within the tested points (25 mm radius sphere centered at the needle tip) was on the order of 120. These results were similar to those found by Ghahramani *et al.* on 3D echo decorrelation based RFA monitoring in ex-vivo bovine liver, where they found an AUROC of .837 for prediction of local ablation using the globally normalized variant of echo decorrelation imaging [81].

The threshold achieving 90% specificity ($\Delta_{90\%}$) for prediction of local ablation tended to vary with the control threshold, this is shown in Figure 3.33a, which shows a bar plot with mean $\Delta_{90\%}$ per each control threshold. This also coincided with an improvement in the prediction of local ablation in the feedback-controlled trials, as shown in Figure 3.33b. As trials with feedback control are stopped when the spatial mean decorrelation exceeds the threshold, it would be expected that local decorrelation values would be close to the control threshold. This is true only if high decorrelation events occur consistently throughout the ROI. If high decorrelation events were limited to a small subregion, then the mean could exceed the control threshold while the local decorrelation values were significantly higher than the threshold. The improvement in the AUC of the ROC curve likely arose for similar reasons as the change in $\Delta_{90\%}$, control stopped the procedure

early and limited the effect of decorrelation events which might have occurred without correspondence to thermal lesioning.
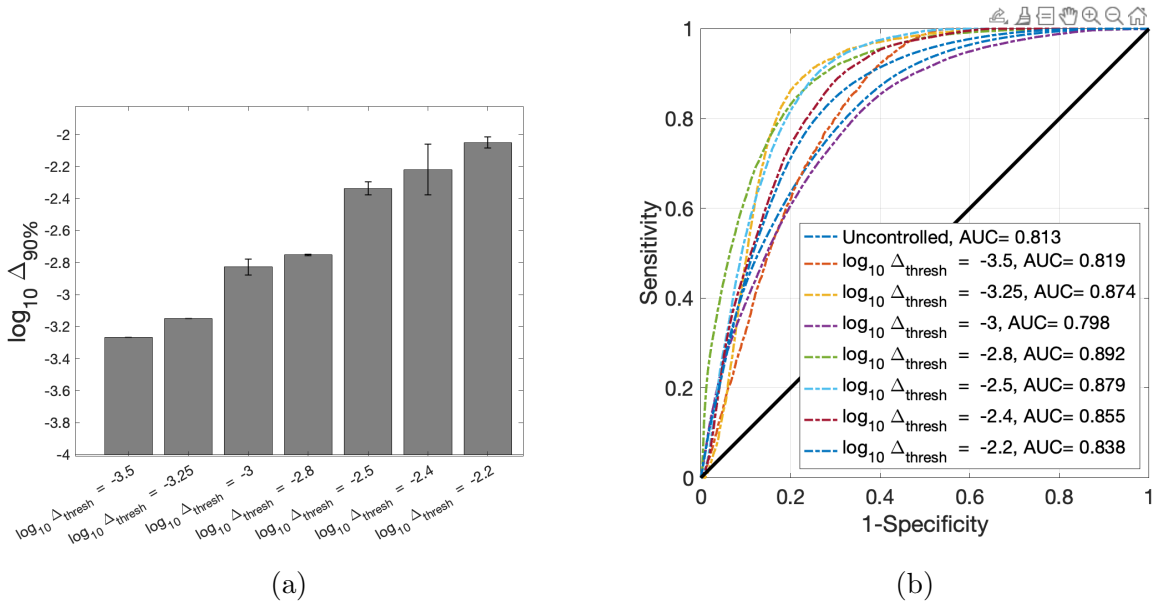
Figure 3.33: Effect of feedback control on computed 90% specificity thresholds for prediction of local ablation. Subfigure (a) shows feedback control threshold vs. threshold achieving 90% specificity, and subfigure (b) shows ROC curves separated by control threshold.

Inhomogeneities within the tissue had a substantial effect on decorrelation maps; for trials with large blood vessels near the ablation needle, decorrelation tended to be higher than in trials without. For some feedback-controlled trials, this resulted in worse performance in terms of targeting the entire ablation margin. The effect of vaporization is widely described in the literature on RFA [26], and a similar effect was observed in studies on HIFU-based control [92]. Figure 3.34 shows an example from the preliminary saline group. In these trials, the procedure was stopped earlier than would have been optimal, as local decorrelation around these inhomogeneities resulted in a higher mean decorrelation which was not indicative of full ablation of the targeted region.

In a related study completed before this thesis, 3D echo decorrelation was compared to integrated backscatter mapping, as well as to two different variants of decorrelation imaging with different normalizations. The three variants of decorrelation compared were: globally-normalized decorrelation, which is normalized only by the global spatial mean backscatter, locally-normalized, which is normalized by local backscatter, and combined
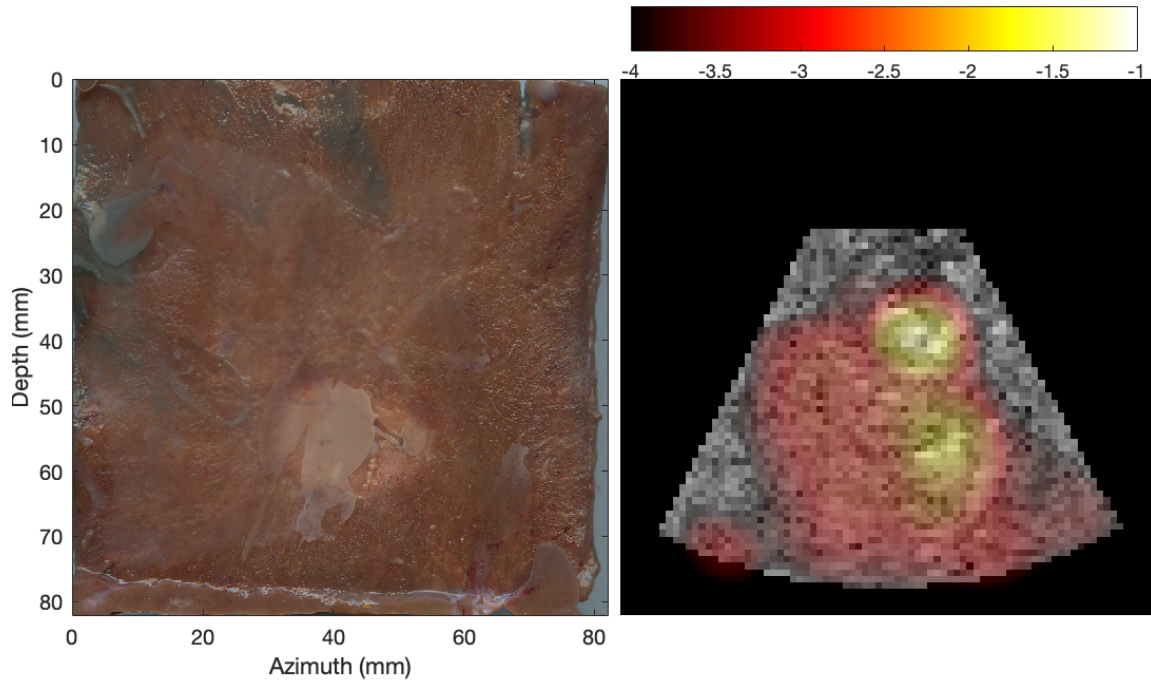
Figure 3.34: Example of increased local decorrelation arising from a blood vessel within the ablation zone. (a) 2D azimuth-depth plane at an elevation of 50 mm from the bottom of the cuvette. (b) Corresponding dB-scaled B-mode plane with overlaid log10-scaled decorrelation.

normalization which is normalized by both global and local backscatter (and is the definition used in this study) [81]. The methodology employed in that study was very similar to that which was employed for the 'uncontrolled' set of trials in this study, except for exposure conditions, which were set to a 2 cm diameter sphere, 150 W power target, a 5-minute ablation time and without saline infusion. Imaging settings also differed; for that study, echo-frames with a larger size of 110 mm × 79° × 79° were used. AUC values for the prediction of tissue lesioning ranged from .726 − .837, a very similar range to what was presented in this thesis. Preliminary results from a study completed by Ghahramani *et al.* were used to inform changes to this study. Power was reduced to 50 W to increase the number of samples taken and reduce any impedance spikes from tissue charring. For similar purposes, the imaging volume was lowered to 80 mm × 56° ×56°, the absolute minimum to encompass our desired region to increase the number of samples during each trial. A larger ablation diameter was selected to increase the number of sampled points within the targeted ablation zone relative to the previous study. Additionally, clinical efficacy of thermal ablation tends to be worse with larger targeted regions, and for lesions

with an ablation margin of 2 cm or less, ablation already has comparable performance to hepatic resection [13]. A larger ablation margin of 3 cm or greater is generally associated with worse performance in RFA procedures and thus is a better test case for the efficacy of feedback control.

The controlled results can be compared to studies completed by Abbass *et al.* on *ex vivo* bovine liver and *in vivo* rabbit liver with HIFU and bulk ultrasound ablation [85] using 2D echo decorrelation based control. They used a control criterion based on the minimum echo decorrelation within the targeted region and mean decorrelation in the targeted region. They found no significant difference in ablation rate or lesion widths between the controlled and uncontrolled groups under any tested control parameters. Our results were similar in finding no significant effect of echo decorrelation-based control on ablation rate and lesion uniformity, but our study showed an increase in conformance to the targeted ablation zone as measured by the Dice coefficient.

This study was limited by a very low temporal resolution due to the time the scanner takes to record and export a pair of echo volumes, which was approximately 7 seconds per volume. Additionally, the amount of time needed for exporting volumes from a single set was roughly linear with the number of volumes recorded; as such, we opted to use only two echo-frames for our calculations, favoring more samples during the treatment over temporal smoothing. This suggests that our computed decorrelation maps were subject to significantly greater random variation than prior studies which used temporal smoothing. Considering we were constrained to using a single echo-frame pair, it is encouraging that the performance of echo decorrelation in predicting local ablation was similar to previous studies using linear arrays. This limitation is not inherent to the method but resulted from the device's slow I/O operations. Theoretically, decorrelation maps could be computed at nearly the device's frame rate, as the additional convolution and multiplication operations are not computationally demanding. Similar algorithms, such as Doppler mode, are already available for these devices.

Overall, the results suggest that 3D echo decorrelation based control can provide some utility in optimizing for a particular lesion geometry. In a clinical setting, better

conformance to the targeted ablation margin could reduce negative clinical outcomes associated with ablated healthy tissue, particularly for patients with impaired hepatic functioning.

Chapter IV

Conclusion

4.0.1 Summary

This thesis explored using 3D echo decorrelation imaging for real-time monitoring and control of radiofrequency thermal ablation in ex-vivo bovine liver. We hypothesized that 3D echo decorrelation imaging's promising performance as a predictor of local thermal lesioning could be utilized as a control parameter for thermal ablation procedures and that this method would result in more uniform thermal lesions that more closely match the desired ablation geometry. To test this hypothesis, we developed a closed-loop feedback control methodology that stopped the procedure early if the spatial average decorrelation within our targeted ablation zone exceeds a set threshold.

Chapter 1 explored the epidemiology, etiology and treatment of liver cancer, as well as an overview of existing monitoring and control methods for thermal ablation treatments. The primary impetus for creating a real-time control method for these procedures is that clinicians do not have a standard, portable and effective way to control the geometry of thermal lesioning in real-time. The ability to automatically control an ablation procedure with real-time feedback could reduce the incidence of local tumor recurrence due to under-treatment and reduce complications from over-treatment.

In Chapter 2, the echo-decorrelation imaging method was described, and previous research on its utility in monitoring and control was outlined. In studies of 2D echo-decorrelation, the technique improved the uniformity of ablated regions compared to

standard temperature-controlled RFA. The previous methodologies were also explored to control HIFU and bulk ultrasound in both *in vivo* and *ex vivo* trials.

Chapter 3 explored the methods we employed to evaluate 3D-echo decorrelation's utility as a predictor of local thermal ablation and our efforts to create an automated feedback-controlled algorithm for optimizing thermal ablation. To assess the hypothesis that 3D echo decorrelation-based feedback control would result in a more uniform lesion volume and geometry, we completed a series of echo decorrelation feedback-controlled and uncontrolled ablation trials at a set control threshold, which was determined via an optimization process based on testing different control criteria in a preliminary group of feedback-controlled trials. The optimization process considered the performance in predicting local tissue lesioning and the full ablation volume. A threshold was selected to achieve high specificity and a reasonable sensitivity in predicting both local thermal lesioning and complete ablation of a proportion of the targeted region.

All trials in our final group of feedback-controlled trials were successfully controlled; that is, the procedure was stopped early due to the spatial average decorrelation exceeding our control threshold. Through analysis of the thermal lesions generated during the RFA procedure, we found that the mean conformance to the desired ablation zone, as measured by the Dice coefficient between the ablation region and the targeted ablation zone, was superior in the feedback-controlled group. We, however, did not find a significant change in variance in the total ablated volume or the ablation rate.

We found that 3D echo decorrelation imaging strongly predicted local tissue lesioning and that echo-decorrelation-based control resulted in smaller lesions with significantly greater conformance to an idealized ablation zone. We also found a moderate but statistically significant correlation between the spatial mean decorrelation within the targeted ablation zone and thermal lesion volume. However, the variance in lesion volume and conformance was not significantly different between the controlled and uncontrolled groups. The central hypothesis of this study was that echo decorrelation feedback control would result in more consistent ablation volumes and better conformance to the desired ablation zone. Of these, only the difference in the mean of the Dice coefficient reached statistical

significance. Variance in the ablated volume was reduced, but this did not meet statistical significance. Overall, we have presented some preliminary evidence that 3D echo decorrelation-based control of RFA procedures can result in greater conformance to a targeted ROI. We however did not show that this control methodology can improve the consistency of RFA induced lesions.

4.0.2 Future directions

This research aims to establish a method for real-time control of clinical RFA procedures using ultrasound imaging. To this end, this work offers some positive results, despite many significant limitations. Feedback control was found to have resulted in better conformance to the targeted ablation zone, but in some cases, a very high decorrelation event occurring within the ROI resulted in ablation being stopped too early.

Both the control criterion and the control methodology could be further improved. Lesions were found to be on average smaller than the targeted 3 cm diameter sphere, possibly suggesting a higher control threshold would be optimal for this particular geometry. We found that decorrelation-feedback control based on the mean within the targeted ROI was susceptible to localized high decorrelation-events arising from tissue inhomogeneity and vaporization. Methods that can account for multiple regions within the tissue independently could potentially offset this but would likely require an increase in spatial resolution to accurately localize different subsections of the ROI to a meaningful degree of accuracy. One potential subregion scheme could be to divide the targeted ROI into concentric semi-spherical subregions. As voxels near the needle tip are nearly always ablated, these points are less relevant for a monitoring and control scheme. Instead, areas where it is less certain that the tissue will be ablated, generally along the outer edge of the treatment margin, should be monitored for successful ablation. Therefore, selecting a subregion that roughly conforms to the shape of the outer edge of the ablation margin might result in a more useful control algorithm for clinical purposes. These regions could then be subdivided into multiple semi-spherical regions to account for local high decorrelation events. Some other ways to account for local high-decorrelation events affecting

the mean within the targeted region could include manual or automatic B-mode image segmentation that could be used to identify regions where localized decorrelation spikes are likely to occur, such as near arteries. An adjustment scheme could then be used to offset these effects.

Alternative control schemes might offer some advantages over the bang-bang type controller used in this study. Control was limited to a single binary decision of whether or not to stop the treatment, a more dynamic control scheme, such as one which modulates delivered power based on observed decorrelation values, might offer some performance benefits. The temperature control functionality of standard RFA equipment, as used in this study, modulates delivered power to maintain a linear increase in temperature measured at its thermocouples. These temperature readings have limited accuracy as they are only able to measure temperature at the location in which they are heating, which does not necessarily reflect tissue temperature in the rest of the targeted lesion. Dynamic control based on a combination of observations such as measured temperature, electrical impedance and decorrelation might improve performance beyond temperature control the decorrelation based bang-bang controller used in this study. Further improvements might involve the use of multiple RFA needles, all of which could be toggled or modulated separately to target a particular geometry using decorrelation imaging.

We found that the method performed similarly in the prediction of local ablation to 2D studies of echo decorrelation imaging, but did so without ensemble-averaging and at a substantially lower spatial and temporal resolution. An implementation with a much greater temporal and spatial resolution is technically feasible and could theoretically improve echo decorrelation's efficacy in predicting thermal lesioning.

As the end goal is clinical use, future research should be focused on ensuring the efficacy of the method in *in-vivo* models of liver cancer. 2D studies of echo decorrelation imaging have shown promise in monitoring and control of *in vivo* radiofrequency ablation, where it was found to significantly outperform backscatter mapping for monitoring thermal lesions under the influence of motion-induced noise [84, 85]. Verification of this

performance in 3D is an essential step to the full implementation of echo decorrelation-based control in true clinical procedures.

Appendix A

Table of trials

Day	Trial	Group	Type	Saline?	Δ_{thresh}	Dice	Vol	Rate	Exclude reason
6/16/20	1	Prelim	Uncont.	No	NA	NA	NA	NA	Probe placement
6/16/20	2	Prelim	Uncont.	No	NA	0.786	18.216	2.181	
7/23/20	1	Prelim	Uncont.	No	NA	0.795	20.699	1.993	
7/23/20	2	Prelim	Uncont.	No	NA	0.882	14.31	1.363	
8/5/20	1	Prelim	Uncont.	No	NA	0.877	11.746	0.91	
8/5/20	2	Prelim	Uncont.	No	NA	0.908	13.454	1.012	
8/5/20	3	Prelim	Uncont.	No	NA	0.668	26.869	2.483	
8/26/20	1	Prelim	Uncont.	No	NA	0.627	19.279	2.102	
8/26/20	2	Prelim	Uncont.	No	NA	0.769	15.279	1.559	
8/26/20	3	Prelim	Uncont.	No	NA	0.838	10.997	1.059	
9/9/20	1	Prelim	Uncont.	No	NA	NA	NA	NA	US data output error
9/9/20	2	Prelim	Cont.	No	-3.5	0.308	2.575	0.742	
9/23/20	1	Prelim	Uncont.	No	NA	0.56	6.379	1.815	
9/23/20	2	Prelim	Uncont.	No	NA	0.795	11.09	1.137	
9/30/20	1	Prelim	Uncont.	No	NA	0.695	17.709	2.823	
9/30/20	2	Prelim	Uncont.	No	NA	0.774	13.052	2.081	
9/30/20	3	Prelim	Cont.	No	-3	0.754	8.872	1.811	
10/7/20	1	Prelim	Uncont.	No	NA	0.39	3.423	0.382	
10/7/20	2	Prelim	Cont.	No	-3.25	0.587	5.88	0.657	
10/7/20	3	Prelim	Cont.	No	-3	NA	NA	NA	Control misconfigured
10/7/20	4	Prelim	Uncont.	No	NA	0.612	6.231	0.712	
10/21/20	1	Prelim	Uncont.	No	NA	0.613	6.982	0.798	
10/21/20	2	Prelim	Cont.	No	-3	0.503	5.522	1.269	
10/21/20	3	Prelim	Cont.	No	-3	0.582	6.709	1.398	
11/4/20	1	Prelim	Uncont.	No	NA	0.656	6.906	0.663	
11/4/20	2	Prelim	Uncont.	No	NA	0.654	6.914	0.672	
11/4/20	3	Prelim	Cont.	No	-3	0.386	3.64	1.308	
11/4/20	4	Prelim	Cont.	No	-3	0.472	4.367	0.794	
11/4/20	5	Prelim	Cont.	No	-3	0.225	1.789	0.475	
11/18/20	1	Prelim	Uncont.	Yes	NA	0.747	16.769	2.004	
11/18/20	2	Prelim	Cont.	Yes	-2.8	0.756	9.286	1.53	
11/18/20	3	Prelim	Cont.	Yes	-2.8	0.678	7.284	0.936	
12/2/20	1	Prelim	Uncont.	Yes	NA	0.844	16.087	1.863	
12/2/20	2	Prelim	Cont.	Yes	-2.4	0.755	9.255	2.136	
12/2/20	3	Prelim	Cont.	Yes	-2.2	0.792	9.542	1.794	
12/16/20	1	Prelim	Uncont.	Yes	NA	0.651	24.929	2.299	
12/16/20	2	Prelim	Cont.	Yes	-2.5	0.641	6.771	1.634	
12/16/20	3	Prelim	Cont.	Yes	-2.5	0.639	6.71	1.697	
12/16/20	4	Prelim	Cont.	Yes	-2.4	0.755	9.777	3.397	
2/3/21	1	Prelim	Uncont.	Yes	NA	0.711	25.035	2.217	

Table A.1: Table of trials in the preliminary group of thermal ablation experiments. Columns shown include the date the trial was performed, the number of the trial in each day, whether or not it used feedback control, whether or not it used saline infusion, the control threshold (if applicable), the Dice coefficient, volume, ablation rate and exclusion reason (if the trial was excluded).

Day	Trial	Group	Type	Saline?	Δ_{thresh}	Dice	Vol	Rate	Exclude reason
2/10/21	1	Final	Uncont.	Yes	NA	0.815	18.818	1.353	
2/10/21	2	Final	Cont.	Yes	-2.2	0.701	7.679	1.443	
2/10/21	3	Final	Cont.	Yes	-2.2	0.819	9.899	1.86	
3/3/21	1	Final	Uncont.	Yes	NA	0.613	34.164	2.456	
3/17/21	1	Final	Uncont.	Yes	NA	0.554	33.064	2.44	
3/17/21	2	Final	Uncont.	Yes	NA	0.611	32.111	1.977	
3/17/21	3	Final	Cont.	Yes	-2.2	0.722	8.059	1.266	
3/31/21	1	Final	Uncont.	Yes	NA	0.775	21.694	1.481	
3/31/21	2	Final	Cont.	Yes	-2.2	0.84	12.639	1.76	
3/31/21	3	Final	Cont.	Yes	-2.2	0.818	11.305	1.976	
4/14/21	1	Final	Uncont.	Yes	NA	0.685	26.713	2.222	
4/14/21	2	Final	Cont.	Yes	-2.2	NA	NA	NA	Tissue sections unusable
4/28/21	1	Final	Uncont.	Yes	NA	NA	NA	NA	Corrupted data output
4/28/21	2	Final	Uncont.	Yes	-2.2	NA	NA	NA	Tissue sections unusable
5/5/21	2	Final	Uncont.	Yes	NA	0.698	25.909	2.012	
5/5/21	3	Final	Cont.	Yes	-2.2	0.775	18.062	2.511	
5/12/21	1	Final	Uncont.	Yes	NA	0.657	28.889	2.274	
5/12/21	2	Final	Cont.	Yes	-2.2	0.729	8.499	1.937	
5/12/21	3	Final	Cont.	Yes	-2.2	0.699	7.644	1.164	
5/19/21	1	Final	Uncont.	Yes	NA	0.587	26.548	2.248	
5/26/21	1	Final	Uncont.	Yes	NA	0.614	26.073	2.242	
5/26/21	2	Final	Cont.	Yes	-2.2	0.628	6.538	1.842	
5/26/21	3	Final	Cont.	Yes	-2.2	0.754	9.304	2.052	
6/16/21	1	Final	Uncont.	Yes	NA	0.807	20.849	1.782	
6/16/21	2	Final	Cont.	Yes	-2.2	0.766	11.412	2.292	
6/16/21	3	Final	Cont.	Yes	-2.2	0.767	12.032	2.683	

Table A.2: Table of trials in the final group of thermal ablation experiments. Columns shown include the date the trial was performed, the number of the trial in each day, whether or not it used feedback control, whether or not it used saline infusion, the control threshold (if applicable), the Dice coefficient, volume, ablation rate and exclusion reason (if the trial was excluded).

Appendix B

Code listings

B.0.1 LUT generation

MEX C function that generates a look-up table of coefficients for scan conversion as described in Equation 3.4. These coefficients can be pre-computed per a particular geometry setting, which lowers the number of FLOPs necessary for scan converting each volume.

```
1       #include "mex.h"
2       #include <math.h>
3   void generatePyramidalCoordinates(const mxArray * p,const mxArray * Lmu, const mxArray * Lnu, const
            mxArray * LR, double dmu, double dnu, double dr, long int pSize, mxArray * out){
4     const double * pArr, * LmuArr, * LnuArr, * LRArr;
5     double * outArr;
6     pArr = mxGetPr(p);
7     LmuArr = mxGetPr(Lmu);
8     LnuArr = mxGetPr(Lnu);
9     LRArr = mxGetPr(LR);
10    outArr = mxGetPr(out);
11    int q = 0;
12    double dmumLmu = 0;
13    double dnumLnu = 0;
14    double drmLR = 0;
15    for(int ip = 0; ip < pSize; ip++){
16      q = pArr[ip];
17      drmLR = dr - LRArr[q-1];
18      dmumLmu = dmu - LmuArr[q-1];
19      dnumLnu = dnu - LnuArr[q-1];
20      outArr[ip*8] = drmLR * dmumLmu * dnumLnu;
21      outArr[ip*8 + 1] = LRArr[q-1] * dmumLmu * dnumLnu;
22      outArr[ip*8 + 2] = drmLR * LmuArr[q-1] * dnumLnu;
23      outArr[ip*8 + 3] = drmLR * dmumLmu * LnuArr[q-1];
24      outArr[ip*8 + 4] = LRArr[q-1] * dmumLmu * LnuArr[q-1];
25      outArr[ip*8 + 5] = drmLR * LmuArr[q-1] * LnuArr[q-1];
26      outArr[ip*8 + 6] = LRArr[q-1] * LmuArr[q-1] * dnumLnu;
27      outArr[ip*8 + 7] = LRArr[q-1] * LmuArr[q-1] * LnuArr[q-1];
28    }
29  }
30  /* The gateway function */
```

```
31  void mexFunction(int nlhs, mxArray *plhs[],
32                   int nrhs, const mxArray *prhs[])
33  {
34    /* variable declarations here */
35    if(nrhs != 8) {
36      mexErrMsgIdAndTxt("MyToolbox:arrayProduct:nrhs",
37                        "One input required.");
38    }
39    if(nlhs != 1) {
40      mexErrMsgIdAndTxt("MyToolbox:arrayProduct:nlhs",
41                        "One output required.");
42    }
43    //mxArray * p,mxArray * Lmu, mxArray * Lnu, mxArray * LR, double dmu, double dnu, double dr, double
              pSize,
44    double dmu = mxGetScalar(prhs[4]);
45    double dnu = mxGetScalar(prhs[5]);
46    double dr = mxGetScalar(prhs[6]);
47    long int pSize = (int)mxGetScalar(prhs[7]);
48    plhs[0] = mxCreateDoubleMatrix(1,pSize * 8,mxREAL);
49    generatePyramidalCoordinates(prhs[0],prhs[1],prhs[2], prhs[3], dmu, dnu, dr, pSize, plhs[0]);
50    return;
51  }
```

B.0.2 Scan conversion

MEX C function that scan converts pyramidal ultrasound data to Cartesian coordinates. Applies the scan conversion coefficients computed in the 'LUT generation' code to the serialized echo data output from the scanner.

```
1   #include "mex.h"
2   #include <math.h>
3   void generateData(const mxArray * pData, const mxArray * inputData, const mxArray * mapIn,
4                     const mxArray * iRIn, const mxArray * inuIn, const mxArray * imuIn, int pSize,
5                     int xSize, int ySize, int zSize, const mxArray * sphSize, mxArray * out){
6     // MXArray pointers
7     const double * inDataReal, * inDataImag, * iR, * inu, * imu;
8     double * outDataReal, * outDataImag;
9     double * mapArr;
10    double * p;
11    double * dimPtr;
12    int rSize,thetaSize,phiSize;
13    int q;
14    int mapInd[8] = {0,0,0,0,0,0,0,0}; //index into map matrix
15    double ptVal[8] = {0,0,0,0,0,0,0,0}; // corresponding value in map matrix
16    int p1,p2,p3,p4,p5,p6,p7,p8; // data index, corresponds to mapInd values
17    // get ptrs to matlab mem
18    mapArr = mxGetPr(mapIn);
19    outDataReal = mxGetPr(out);
20    outDataImag = mxGetPi(out);
21    inDataReal = mxGetPr(inputData);
22    inDataImag = mxGetPi(inputData);
23    imu = mxGetPr(imuIn);
24    inu = mxGetPr(inuIn);
25    iR = mxGetPr(iRIn);
26    p = mxGetPr(pData);
```

92

```
27      dimPtr = mxGetPr(sphSize);
28      rSize = dimPtr[0];
29      thetaSize = dimPtr[1];
30      phiSize = dimPtr[2];
31      double wtCoef = thetaSize*rSize;
32      //loop through points
33      for(int ip = 0; ip < pSize; ip++){
34        // get current point
35        q = (int)p[ip];
36        // index into 1D array as 3D array
37        // combined to save operations
38        //p1 = iR[q-1] + thetaSize * (imu[q-1] + phiSize * inu[q-1]);
39        p1 = iR[q-1]-1 + (imu[q-1]-1)*rSize + (inu[q-1]-1)*wtCoef;
40        p2 = p1 + 1;
41        p3 = p1 + rSize;
42        p4 = p1 + wtCoef;
43        p5 = p4 + 1;
44        p6 = p4 + rSize;
45        p7 = p3 + 1;
46        p8 = p4 + 1;
47        //get index into point*8 map matrix
48        mapInd[0] = ip*8;
49        ptVal[0] = mapArr[mapInd[0]];
50        for(int j = 1; j < 8; j++){
51          mapInd[j] = mapInd[j-1] + 1;
52          ptVal[j] = mapArr[mapInd[j]];
53        }
54        outDataReal[q-1] = p7;
55        outDataImag[q-1] = p8;
56        outDataReal[q-1] = inDataReal[p1] * ptVal[0] + inDataReal[p2] * ptVal[1] +
57          inDataReal[p3] * ptVal[2] + inDataReal[p4] * ptVal[3] +
58          inDataReal[p5] * ptVal[4] + inDataReal[p6] * ptVal[5] +
59          inDataReal[p7] * ptVal[6] + inDataReal[p8] * ptVal[7];
60        outDataImag[q-1] = inDataImag[p1] * ptVal[0] + inDataImag[p2] * ptVal[1] +
61          inDataImag[p3] * ptVal[2] + inDataImag[p4] * ptVal[3] +
62          inDataImag[p5] * ptVal[4] + inDataImag[p6] * ptVal[5] +
63          inDataImag[p7] * ptVal[6] + inDataImag[p8] * ptVal[7];
64      }
65    }
66    /*
67    The gateway function */
68    void mexFunction(int nlhs, mxArray *plhs[],
69                     int nrhs, const mxArray *prhs[])
70    {
71      /* variable declarations here */
72      if(nrhs != 11) {
73        mexErrMsgIdAndTxt("MyToolbox:arrayProduct:nrhs",
74                          "One input required.");
75      }
76      if(nlhs != 1) {
77        mexErrMsgIdAndTxt("MyToolbox:arrayProduct:nlhs",
78                          "One output required.");
79      }
80
81      long int pSize = (int)mxGetScalar(prhs[6]);
82      long int xSize = (int)mxGetScalar(prhs[7]);
83      long int ySize = (int)mxGetScalar(prhs[8]);
84      long int zSize = (int)mxGetScalar(prhs[9]);
85      plhs[0] = mxCreateDoubleMatrix(1,xSize*ySize*zSize,mxCOMPLEX);
```

```
86        generateData ( prhs [ 0 ] , prhs [ 1 ] , prhs [ 2 ] , prhs [ 3 ] , prhs [ 4 ] , prhs [ 5 ] , pSize , xSize , ySize , zSize , prhs [ 1 0 ] ,
              plhs [ 0 ] ) ;
87        return ;
88    }
```

B.1   Echo decorrelation

MATLAB implementation of echo decorrelation using frequency domain-based convolution as defined in equation 2.6.

```
1         function compute3DDecorr_Freq ( obj )
2         % Pad for FFT convolution
3         for currVol = 1:size(obj.rawData_cart ,4)
4             paddedData (:,:,:, currVol ) = padarray ( volData (:,:,:, currVol ) , padImArr , 'both ' ) ;
5         end
6         % *compute windowed ibs and autocorr01*
7         %compute ibs and autocorr before windowing
8         ibsPadded = abs ( paddedData ) .^2;
9         autocorr01Padded = paddedData (:,:,:, 1:( end−1)) .* conj ( paddedData (:,:,:, 2: end ) ) ;
10        % set NaN values to 0
11        ibsPadded ( find ( isnan ( ibsPadded ) ) ) = 0;
12        autocorr01Padded ( find ( isnan ( autocorr01Padded ) ) ) = 0;
13        %compute windowed ibs
14
15        for currVolume = 1:size ( ibsPadded ,4)
16          ibsPadded (:,:,:, currVolume ) = ( ifftshift ( ifftn ( fftn ( ibsPadded (:,:,:, currVolume )) .* kernelFreq ) ) ) ;
17        end
18        %compute autcorrelation and decorrelation
19        for currVolume = 1:( size ( ibsPadded ,4) −1)
20            autocorr01Padded (:,:,:, currVolume ) = abs ( ifftshift ( ifftn ( fftn ( autocorr01Padded (:,:,:,
                  currVolume )) .* kernelFreq ) ) ) ;
21        end
22
23        obj.ibs = ibsPadded (1+padImArr (1): end−padImArr (1)−padToOdd (1) ,1+padImArr (2): end−padImArr (2)−
              padToOdd (2) ,1+padImArr (3): end−padImArr (3)−padToOdd (3) ,:) ;
24        obj.autocorr01= autocorr01Padded (1+padImArr (1): end−padImArr (1)−padToOdd (1) ,1+padImArr (2): end−
              padImArr (2)−padToOdd (2) ,1+padImArr (3): end−padImArr (3)−padToOdd (3) ,:) ;
25        for currVolume = 1:( size ( obj.ibs ,4) −1)
26            R00 = obj.ibs (:,:,:, currVolume ) ;
27            R11 = obj.ibs (:,:,:, currVolume+1);
28            B2 = R00.*R11;
29            B2ValidIBS = B2 ( validRange , validAz , validEl ) ;
30            BMean=mean ( B2ValidIBS (:) ) ;
31            R01 = ( obj.autocorr01 (:,:,:, currVolume )) .^2;
32
33            obj.decorr (:,:,:, currVolume ) = 2*(B2−R01) ./( B2 + BMean ) / obj.interFrameTime ;
34
35        end
36    end
```

B.2 Serial interface

B.2.1 Arduino code

Code for microcontroller circuit responsible for actuating the pneumatic switch on the RF generator. Polls for a control signal over a serial connection and activates pump and solenoid valve in rapid succession.

```
1      bool pressureCharged = false;
2   unsigned long currTime;
3   char data;
4   void setup() {
5     Serial.begin(115200);
6     pinMode(22,OUTPUT);
7     pinMode(24,OUTPUT);
8     Serial.setTimeout(50);
9   }
10
11  void loop() {
12    //Serial.print("test");
13    delay(50);
14    if(!pressureCharged){
15      digitalWrite(24,HIGH);
16      currTime = millis();
17      while(millis()-currTime<1000);
18      digitalWrite(24,LOW);
19      pressureCharged = true;
20      delay(50);
21    }
22
23    while(Serial.available() > 0){
24      if(Serial.available() > 0){
25        data = Serial.read();
26        if(data == 'S'){
27          delay(50);
28          Serial.print(F("\n \n **Acitvated** \n \n"));
29          digitalWrite(22,HIGH);
30          currTime = millis();
31          while(millis()-currTime<500);
32          digitalWrite(22,LOW);
33          pressureCharged = false;
34          delay(100);
35        }
36        data = "";
37        delay(50);
38      }
39    }
40    currTime = millis();
41    while(millis()-currTime<100);
42    delay(50);
43
44  }
```

B.2.2 Function for converting fixed point data to floating point

C function which converts non-standard fixed point numbers output from the scanner to standard floating point numbers using bitwise operations.

```
1   #include "mex.h"
2   #include <string>
3   #include <math.h>
4   float fixed2float_17(char * strIn){
5       /* fixed2float_17
6           converts a 17-bit signed fixed point (2^-1) number to a 32 bit float
7
8           standard floats are of the form 1.b1b2..., output must be corrected to account for this
9       */
10      unsigned int signedFloatMask = 0b0011110010000000000000000000000;
11      /* Signed float mask: When XOR'd with the input 32 bit unsigned twos compliment int forms a float
               with exponent -1 and a 1 sign bit, also reverses shifted sign bit eg in decimal[1][126-8][bits
               ][padded to end] *\
12          unsigned int unsignedFloatMask = 0b0011111100000000000000000000000;
13      /*
14       Unsigned float mask: When XOR'd with the input forms a float with exponent -1
15       and a 0 sign bit
16       *\
17      float floatCorrection = .5; // Mantissa is of the form 1.b1b2b3... so when exponent = -1 there is
               an additional 2^-1 (.5) term in the float, which must be subtracted/added depending on sign
18      //get input int
19      unsigned int num = strtol(hexString, nullptr,16); //convert hex string to int
20      //  Bitwise manipulation
21      if (num >> 17){ // check if signed bit is 1
22          num = (((~num)+1) << 7) ^ signedFloatMask;
23          return *(float*)(&num) + floatCorrection; // dereference num, cast what the address points to
                   as a float and add correction
24      }
25      else{
26          num = (num<<7) ^ unsignedFloatMask; // same as above, but don't take two's compliment
27          return *(float*)(&num) - floatCorrection; // .5 is here because mantissa in a float is of the
                   form 1.b1b2b3..., with an exponent of -1, .5 must is left over
28      }
29  }
```

96

Bibliography

[1]H. Sung, J. Ferlay, R. L. Siegel, M. Laversanne, I. Soerjomataram, A. Jemal, and F. Bray, "Global cancer statistics 2020: Globocan estimates of incidence and mortality worldwide for 36 cancers in 185 countries," CA: A Cancer Journal for Clinicians **71**, 209–249 (2021).

[2]R. L. Siegel, K. D. Miller, and A. Jemal, "Cancer statistics, 2020," CA: A Cancer Journal for Clinicians **70**, 7–30 (2020).

[3]K. A. McGlynn, J. L. Petrick, and H. B. El-Serag, "Epidemiology of hepatocellular carcinoma," Hepatology **73**, 4–13 (2021).

[4]M Mohammadian, N Mahdavifar, A Mohammadian-Hafshejani, and H Salehiniya, "Liver cancer in the world - epidemiology, incidence, mortality and risk factors," World Cancer Research Journal **5**, 8 (2018).

[5]A. B. Benson, M. I. D'Angelica, D. E. Abbott, T. A. Abrams, S. R. Alberts, D. A. Anaya, C. Are, D. B. Brown, D. T. Chang, A. M. Covey, W. Hawkins, R. Iyer, R. Jacob, A. Karachristos, R. K. Kelley, R. Kim, M. Palta, J. O. Park, V. Sahai, T. Schefter, C. Schmidt, J. K. Sicklick, G. Singh, D. Sohal, S. Stein, G. G. Tian, J.-N. Vauthey, A. P. Venook, A. X. Zhu, K. G. Hoffmann, and S. Darlow, "NCCN Guidelines Insights: Hepatobiliary Cancers, Version 1.2017," Journal of the National Comprehensive Cancer Network **15**, 563–573 (2017).

[6]J. K. Heimbach, L. M. Kulik, R. S. Finn, C. B. Sirlin, M. M. Abecassis, L. R. Roberts, A. X. Zhu, M. H. Murad, and J. A. Marrero, "AASLD guidelines for the treatment of hepatocellular carcinoma: Heimbach et al.," Hepatology **67**, 358–380 (2018).

[7]Z. Chen, H. Xie, M. Hu, T. Huang, Y. Hu, N. Sang, and Y. Zhao, "Recent progress in treatment of hepatocellular carcinoma," American Journal of Cancer Research **10**, 2993–3036 (2020).

[8]P. C. Valery, M. Laversanne, P. J. Clark, J. L. Petrick, K. A. McGlynn, and F. Bray, "Projections of primary liver cancer to 2030 in 30 countries worldwide," Hepatology **67**, 600–611 (2018).

[9]S. R. Horn, K. C. Stoltzfus, E. J. Lehrer, L. A. Dawson, L. Tchelebi, N. J. Gusani, N. K. Sharma, H. Chen, D. M. Trifiletti, and N. G. Zaorsky, "Epidemiology of liver metastases," Cancer Epidemiology **67**, 101760 (2020).

[10]A. Forner, M. Gilabert, J. Bruix, and J.-L. Raoul, "Treatment of intermediate-stage hepatocellular carcinoma," Nature Reviews Clinical Oncology **11**, 525–535 (2014).

[11]W. Tan, Q. Deng, S. Lin, Y. Wang, and G. Xu, "Comparison of microwave ablation and radiofrequency ablation for hepatocellular carcinoma: a systematic review and meta-analysis," International Journal of Hyperthermia **36**, 263–271 (2019).

[12]J. A. Marrero, L. M. Kulik, C. B. Sirlin, A. X. Zhu, R. S. Finn, M. M. Abecassis, L. R. Roberts, and J. K. Heimbach, "Diagnosis, staging, and management of hepatocellular carcinoma: 2018 practice guidance by the American Association for the Study of Liver Diseases," Hepatology **68**, 723–750 (2018).

[13]A. Ayav, A. Germain, F. Marchal, I. Tierris, V. Laurent, C. Bazin, Y. Yuan, L. Robert, L. Brunaud, and L. Bresler, "Radiofrequency ablation of unresectable liver tumors: factors associated with incomplete ablation or local recurrence," The American Journal of Surgery **200**, 435–439 (2010).

[14]M. A. Chinnaratha, M.-y. A. Chuang, R. J. Fraser, R. J. Woodman, and A. J. Wigg, "Percutaneous thermal ablation for primary hepatocellular carcinoma: a systematic review and meta-analysis: thermal ablation-hepatocellular carcinoma," Journal of Gastroenterology and Hepatology **31**, 294–301 (2016).

[15]Y. Seyama and N. Kokudo, "Assessment of liver function for safe hepatic resection," Hepatology Research **39**, 107–116 (2009).

[16]M. J. Swierz, D. Storman, R. P. Riemsma, R. Wolff, J. W. Mitus, M. Pedziwiatr, J. Kleijnen, and M. M. Bala, "Percutaneous ethanol injection for liver metastases," The Cochrane Database of Systematic Reviews **2**, CD008717 (2020).

[17]R. Lencioni and L. Crocetti, "Radiofrequency ablation of liver cancer," Techniques in Vascular and Interventional Radiology **10**, 38–46 (2007).

[18]P.-S. Yi, M. Huang, M. Zhang, L. Xu, and M.-Q. Xu, "Comparison of transarterial chemoembolization combined with radiofrequency ablation therapy versus surgical sesection for early hepatocellular carcinoma," The American Surgeon **84**, 282–288 (2018).

[19]J. P. McWilliams, E. W. Lee, S. Yamamoto, C. T. Loh, and S. T. Kee, "Image-guided tumor ablation: emerging technologies and future directions," Seminars in Interventional Radiology **27**, 302–313 (2010).

[20]T. T. Cheung, K. W. Ma, and W. H. She, "A review on radiofrequency, microwave and high-intensity focused ultrasound ablations for hepatocellular carcinoma with cirrhosis," Hepatobiliary Surgery and Nutrition **10**, 193–209 (2021).

[21]K. B. Gala, N. S. Shetty, P. Patel, and S. S. Kulkarni, "Microwave ablation: how we do it?," The Indian Journal of Radiology & Imaging **30**, 206–213 (2020).

[22]Z. Jia, H. Zhang, and N. Li, "Evaluation of clinical outcomes of radiofrequency ablation and surgical resection for hepatocellular carcinoma conforming to the Milan criteria: a systematic review and meta-analysis of recent randomized controlled trials," Journal of Gastroenterology and Hepatology **36**, 1769–1777 (2021).

[23]I. S. Yoon, J. H. Shin, K. Han, P. N. Kim, K. H. Kim, Y.-K. Kang, and H. K. Ko, "Ultrasound-guided intraoperative radiofrequency ablation and surgical resection for liver metastasis from malignant gastrointestinal stromal tumors," Korean Journal of Radiology **19**, 54–62 (2018).

[24]Y.-S. Kim, W. J. Lee, H. Rhim, H. K. Lim, D. Choi, and J. Y. Lee, "The minimal ablative margin of radiofrequency ablation of hepatocellular carcinoma (> 2 and < 5

cm) needed to prevent local tumor progression: 3D quantitative assessment using CT image fusion," AJR. American Journal of Roentgenology **195**, 758–765 (2010).

[25]J. W. Kim, S. S. Shin, S. H. Heo, J. H. Hong, H. S. Lim, H. J. Seon, Y. H. Hur, C. H. Park, Y. Y. Jeong, and H. K. Kang, "Ultrasound-guided percutaneous radiofrequency ablation of liver tumors: how we do it safely and completely," Korean Journal of Radiology **16**, 1226–1239 (2015).

[26]T. Wake, R. Tateishi, R. Nakagomi, N. Fujiwara, M. N. Kinoshita, T. Nakatsuka, M. Sato, T. Minami, K. Uchino, K. Enooku, H. Nakagawa, Y. Asaoka, Y. Tanaka, S. Shiina, and K. Koike, "Ischemic complications after percutaneous radiofrequency ablation of liver tumors: liver volume loss and recovery," Hepatology Research **49**, 453–461 (2019).

[27]W.-T. Kong, W.-W. Zhang, Y.-D. Qiu, T. Zhou, J.-L. Qiu, W. Zhang, and Y.-T. Ding, "Major complications after radiofrequency ablation for liver tumors: analysis of 255 patients," World Journal of Gastroenterology: WJG **15**, 2651–2656 (2009).

[28]C. Kim, "Understanding the nuances of microwave ablation for more accurate post-treatment assessment," Future Oncology **14**, 1755–1764 (2018).

[29]J. W. Kim, S. S. Shin, J. K. Kim, S. K. Choi, S. H. Heo, H. S. Lim, Y. H. Hur, C. K. Cho, Y. Y. Jeong, and H. K. Kang, "Radiofrequency ablation combined with transcatheter arterial chemoembolization for the treatment of single hepatocellular carcinoma of 2 to 5 cm in diameter: comparison with surgical resection," Korean Journal of Radiology **14**, 626–635 (2013).

[30]H. Takahashi, M. Akyuz, E. Aksoy, K. Karabulut, and E. Berber, "Local recurrence after laparoscopic radiofrequency ablation of malignant liver tumors: results of a contemporary series," Journal of Surgical Oncology **115**, 830–834 (2017).

[31]E. Goto, R. Tateishi, S. Shiina, R. Masuzaki, K. Enooku, T. Sato, T. Ohki, Y. Kondo, T. Goto, H. Yoshida, and M. Omata, "Hemorrhagic complications of percutaneous radiofrequency ablation for liver tumors," Journal of Clinical Gastroenterology **44**, 374–380 (2010).

[32] A. A. J. M. van Tilborg, H. J. Scheffer, M. C. de Jong, L. G. P. H. Vroomen, K. Nielsen, C. van Kuijk, P. M. P. van den Tol, and M. R. Meijerink, "MWA Versus RFA for perivascular and peribiliary CRLM: a retrospective patient- and lesion-based analysis of two historical cohorts," CardioVascular and Interventional Radiology **39**, 1438–1446 (2016).

[33] Y.-F. Zhou, "High intensity focused ultrasound in clinical tumor ablation," World Journal of Clinical Oncology **2**, 8–27 (2011).

[34] C. M. C. Tempany, N. J. McDannold, K. Hynynen, and F. A. Jolesz, "Focused ultrasound surgery in oncology: overview and principles," Radiology **259**, 39 (2011).

[35] A. Dupre, D. Melodelima, D. Perol, Y. Chen, J. Vincenot, J.-Y. Chapelon, and M. Rivoire, "Evaluation of the feasibility, safety, and accuracy of an intraoperative high-intensity focused ultrasound device for treating liver metastases," Journal of Visualized Experiments: JoVE **143**, e57964 (2019).

[36] D. Gianfelice, A. Khiat, M. Amara, A. Belblidia, and Y. Boulanger, "MR imaging-guided focused US ablation of breast cancer: histopathologic assessment of effectiveness–initial experience," Radiology **227**, 849–855 (2003).

[37] M. Marinova, H. Feradova, M. A. Gonzalez-Carmona, R. Conrad, T. Tonguc, M. Thudium, M. U. Becher, Z. Kun, G. Gorchev, S. Tomov, C. P. Strassburg, U. Attenberger, H. H. Schild, D. Dimitrov, and H. M. Strunk, "Improving quality of life in pancreatic cancer patients following high-intensity focused ultrasound (HIFU) in two European centers," European Radiology **31**, 5818–5829 (2021).

[38] N. T. Sanghvi, W.-H. Chen, R. Carlson, C. Weis, R. Seip, T. Uchida, and M. Marberger, "Clinical validation of real-time tissue change monitoring during prostate tissue ablation with high intensity focused ultrasound," Journal of Therapeutic Ultrasound **5**, 24 (2017).

[39] S. Thüroff, C. Chaussy, G. Vallancien, W. Wieland, H. J. Kiel, A. Le Duc, F. Desgrandchamps, J. J. M. C. H. De La Rosette, and A. Gelet, "High-intensity focused ultrasound

and localized prostate cancer: efficacy results from the European multicentric study," Journal of Endourology **17**, 673–677 (2003).

[40]N. McDannold, G. T. Clement, P. Black, F. Jolesz, and K. Hynynen, "Transcranial magnetic resonance imaging-guided focused ultrasound surgery of brain tumors: initial findings in 3 patients," Neurosurgery **66**, 323–332 (2010).

[41]G. Foltz, "Image-guided percutaneous ablation of hepatic malignancies," Seminars in Interventional Radiology **31**, 180–186 (2014).

[42]R. Lencioni, T. de Baere, R. C. Martin, C. W. Nutting, and G. Narayanan, "Image-guided ablation of malignant liver tumors: recommendations for clinical validation of novel thermal and non-thermal technologies – a western perspective," Liver Cancer **4**, 208–214 (2015).

[43]Y.-B. Wang, R. Ma, Z.-B. Wang, Q.-L. Shi, L. Zhang, W.-Z. Chen, J.-P. Gong, and J. Bai, "Transcatheter arterial chemoembolization in combination with high-intensity focused ultrasound for intermediate and advanced hepatocellular carcinoma: a meta-analysis," Frontiers in Oncology **12**, 797349 (2022).

[44]J.-Y. Ni, S.-S. Liu, L.-F. Xu, H.-L. Sun, and Y.-T. Chen, "Meta-analysis of radiofrequency ablation in combination with transarterial chemoembolization for hepatocellular carcinoma," World Journal of Gastroenterology: WJG **19**, 3872 (2013).

[45]Z.-W. Peng, Y.-J. Zhang, M.-S. Chen, L. Xu, H.-H. Liang, X.-J. Lin, R.-P. Guo, Y.-Q. Zhang, and W. Y. Lau, "Radiofrequency ablation with or without transcatheter arterial chemoembolization in the treatment of hepatocellular carcinoma: a prospective randomized trial," Journal of Clinical Oncology **31**, 426–432 (2013).

[46]F. Wu, Z.-B. Wang, W.-Z. Chen, J.-Z. Zou, J. Bai, H. Zhu, K.-Q. Li, C.-B. Jin, F.-L. Xie, and H.-B. Su, "Advanced hepatocellular carcinoma: treatment with high-intensity focused ultrasound ablation combined with transcatheter arterial embolization," Radiology **235**, 659–667 (2005).

[47]R. S. Puijk, A. H. Ruarus, H. J. Scheffer, L. G. Vroomen, A. A. van Tilborg, J. J. de Vries, F. H. Berger, P. M. van den Tol, and M. R. Meijerink, "Percutaneous liver tumour ablation: image guidance, endpoint assessment, and quality control," Canadian Association of Radiologists Journal **69**, 51–62 (2018).

[48]Z. Zhou, Y. Wang, S. Song, W. Wu, S. Wu, and P.-H. Tsui, "Monitoring microwave ablation using ultrasound echo decorrelation imaging: an ex vivo study," Sensors **19**, 977 (2019).

[49]G. Francica, M. F. Meloni, I. De Sio, M. Pompili, F. Terracciano, and E. Caturelli, "P.12.2: ablation treatment of primary and secondary liver tumors under contrast-enhanced ultrasound (CEUS) guidance. a multicenter italian study," Digestive and Liver Disease, Abstracts 23rd National Congress of Digestive Diseases, Italian Federation of Societies of Digestive Diseases – FISMAD **49**, e211–e212 (2017).

[50]B. Sharma, A. Martin, and I. Zerizer, "Positron emission tomography-computed tomography in liver imaging," Seminars in Ultrasound, CT and MRI, Hepatobiliary Radiology **34**, 66–80 (2013).

[51]A. H. Mahnken, P. L. Pereira, and T. de Baère, "Interventional oncologic approaches to liver metastases," Radiology **266**, 407–430 (2013).

[52]H. Laumonier, J.-F. Blanc, B. Quesson, O. Seror, C. Laurent, P. Bioulac-Sage, C. Balabaud, and H. Trillaud, "Real-time monitoring of hepatocellular carcinoma radiofrequency ablation by quantitative temperature MRI," Seminars in Liver Disease **26**, 391–397 (2006).

[53]J. Dong, X. Geng, Y. Yang, X. Cai, P. Hu, L. Xia, B. Zhang, and P. Wu, "Dynamic imaging and pathological changes in pig liver after MR-guided microwave ablation," BMC Cancer **18**, 397 (2018).

[54]Y.-K. Hue, A. R. Guimaraes, O. Cohen, E. Nevo, A. Roth, and J. L. Ackerman, "Magnetic resonance mediated radiofrequency ablation," IEEE Transactions on Medical Imaging **37**, 417–427 (2018).

[55] C. Maleke and E. E. Konofagou, "Harmonic motion imaging for focused ultrasound (HMIFU): a fully integrated technique for sonication and monitoring of thermal ablation in tissues," Physics in Medicine and Biology **53**, 1773–1793 (2008).

[56] S.-Y. Chiou, J.-B. Liu, and L. Needleman, "Current status of sonographically guided radiofrequency ablation techniques," Journal of Ultrasound in Medicine **26**, 487–499 (2007).

[57] M. Peller, V. Kurze, R. Loeffler, S. Pahernik, M. Dellian, A. E. Goetz, R. Issels, and M. Reiser, "Hyperthermia induces t1 relaxation and blood flow changes in tumors. a MRI thermometry study in vivo," Magnetic Resonance Imaging **21**, 545–551 (2003).

[58] C. Weidensteiner, B. Quesson, B. Caire-Gana, N. Kerioui, A. Rullier, H. Trillaud, and C. T. W. Moonen, "Real-time MR temperature mapping of rabbit liver in vivo during thermal ablation," Magnetic Resonance in Medicine **50**, 322–330 (2003).

[59] M. Lepetit-Coiffé, H. Laumonier, O. Seror, B. Quesson, M.-B. Sesay, C. T. W. Moonen, N. Grenier, and H. Trillaud, "Real-time monitoring of radiofrequency ablation of liver tumors using thermal-dose calculation by MR temperature imaging: initial results in nine patients, including follow-up," European Radiology **20**, 193–201 (2010).

[60] E. J. Stein, N. R. Perkons, J. C. Wildenberg, S. K. Iyer, S. J. Hunt, G. J. Nadolski, W. R. Witschey, and T. P. Gade, "MR imaging enables real-time monitoring of in vitro electrolytic ablation of hepatocellular carcinoma," Journal of Vascular and Interventional Radiology **31**, 352–361 (2020).

[61] V. Rieke and K. B. Pauly, "MR thermometry," Journal of Magnetic Resonance Imaging: JMRI **27**, 376–390 (2008).

[62] Y. Ishihara, A. Calderon, H. Watanabe, K. Okamoto, Y. Suzuki, K. Kuroda, and Y. Suzuki, "A precise and fast temperature mapping using water proton chemical shift," Magnetic Resonance in Medicine **34**, 814–823 (1995).

[63] S. Clasen and P. L. Pereira, "Magnetic resonance guidance for radiofrequency ablation of liver tumors," Journal of Magnetic Resonance Imaging **27**, 421–433 (2008).

[64] A. Darkazanli, K. Hynynen, E. C. Unger, and J. F. Schenck, "On-line monitoring of ultrasonic surgery with MR imaging," Journal of Magnetic Resonance Imaging: JMRI **3**, 509–514 (1993).

[65] L. Su, W. Tian, M. Xu, M. Lin, B. Zhuang, T. Huang, J. Ye, M. Lv, and X. Xie, "Performance of shear wave elastography in delineating the radiofrequency ablation boundary: an in vivo experiment," Ultrasound in Medicine & Biology **45**, 1324–1330 (2019).

[66] K. Samimi, J. K. White, C. L. Brace, and T. Varghese, "Monitoring microwave ablation of ex-vivo bovine liver using ultrasonic attenuation imaging," Ultrasound in Medicine & Biology **43**, 1441–1451 (2017).

[67] S. Zhang, R. Xu, S. Shang, Y. Han, S. Liu, T. Xu, C. Gu, X. Zhu, G. Niu, and M. Wan, "In vivo monitoring of microwave ablation in a porcine model using ultrasonic differential attenuation coefficient intercept imaging," International Journal of Hyperthermia **34**, 1157–1170 (2018).

[68] F.-Y. Liu, X.-L. Yu, P. Liang, Z.-G. Cheng, Z.-Y. Han, B.-W. Dong, and X.-H. Zhang, "Microwave ablation assisted by a real-time virtual navigation system for hepatocellular carcinoma undetectable by conventional ultrasonography," European Journal of Radiology **81**, 1455–1459 (2012).

[69] J. Civale, I. Rivens, G. Ter Haar, H. Morris, C. Coussios, P. Friend, and J. Bamber, "Calibration of ultrasound backscatter temperature imaging for high-intensity focused ultrasound treatment planning," Ultrasound in Medicine & Biology **39**, 1596–1612 (2013).

[70] B. J. Fahey, R. C. Nelson, S. J. Hsu, D. P. Bradway, D. M. Dumont, and G. E. Trahey, "In vivo guidance and assessment of liver radio-frequency ablation with acoustic radiation force elastography," Ultrasound in Medicine & Biology **34**, 1590–1603 (2008).

[71] R. Matsuzawa, T. Shishitani, S. Yoshizawa, and S. I. Umemura, "Monitoring of lesion induced by high-intensity focused ultrasound using correlation method based on block

matching," Japanese Journal of Applied Physics, Part 1: Regular Papers & Short Notes **51** (2012).

[72]E. E. Konofagou, C. Maleke, and J. Vappou, "Harmonic motion imaging (HMI) for tumor imaging and treatment monitoring," Current Medical Imaging Reviews **8**, 16–26 (2012).

[73]F. M. Hooi, A. Nagle, S. Subramanian, and T. Douglas Mast, "Analysis of tissue changes, measurement system effects, and motion artifacts in echo decorrelation imaging," The Journal of the Acoustical Society of America **137**, 585–597 (2015).

[74]T. D. Mast, D. P. Pucke, S. E. Subramanian, W. J. Bowlus, S. M. Rudich, and J. F. Buell, "Ultrasound monitoring of in vitro radio frequency ablation by echo decorrelation imaging," Journal of Ultrasound in Medicine **27**, 1685–1697 (2008).

[75]Q. Huang and Z. Zeng, "A review on real-time 3D ultrasound imaging technology," BioMed Research International **2017**, 1–20 (2017).

[76]A. Fenster, G. Parraga, and J. Bax, "Three-dimensional ultrasound scanning," Interface Focus **1**, 503–519 (2011).

[77]F. Taddei, L. Franceschetti, G. Farina, F. Prefumo, M. Signorelli, N. Fratelli, and C. Groli, "Matrix array transducers in fetal heart imaging," Donald School Journal of Ultrasound in Obstetrics and Gynecology **1**, 45–48 (2007).

[78]L. F. Gonçalves, J. Espinoza, J. P. Kusanovic, W. Lee, J. K. Nien, J. S.-F. J, G. Mari, M. C. Treadwell, and R. Romero, "Applications of 2D matrix array for 3D and 4D examination of the fetus: a pictorial essay," Journal of Ultrasound in Medicine **25**, 745–755 (2006).

[79]E. J. Kim, Y. S. Kim, S. K. Shin, O. S. Kwon, D. J. Choi, and J. H. Kim, "Contrast-enhanced ultrasound-guided radiofrequency ablation in inconspicuous hepatocellular carcinoma on B-mode ultrasound," The Turkish Journal of Gastroenterology **28**, 446–452 (2017).

[80]M. F. Insana, L. T. Cook, M. Bilgen, P. Chaturvedi, and Y. Zhu, "Maximum-likelihood approach to strain imaging using ultrasound," The Journal of the Acoustical Society of America **107**, 1421–1434 (2000).

[81]E. Ghahrahmani Z., P. D. Grimm, M. T. Cox, K. J. Eary, E. G. S. Dayavansha, and T. D. Mast, "Ex vivo thermal ablation monitoring using three-dimensional ultrasound echo decorrelation imaging," The Journal of the Acoustical Society of America **145**, 1862–1862 (2019).

[82]S. Subramanian, S. M. Rudich, A. Alqadah, C. P. Karunakaran, M. B. Rao, and T. D. Mast, "In vivo thermal ablation monitoring using ultrasound echo decorrelation imaging," Ultrasound in Medicine & Biology **40**, 102–114 (2014).

[83]M. T. Cox, M. A. Abbass, and T. D. Mast, "Numerical analysis of three-dimensional echo decorrelation imaging," The Journal of the Acoustical Society of America **147**, EL478–EL483 (2020).

[84]T. R. Fosnight, F. M. Hooi, R. D. Keil, A. P. Ross, S. Subramanian, T. G. Akinyi, J. K. Killin, P. G. Barthe, S. M. Rudich, S. A. Ahmad, M. B. Rao, and T. D. Mast, "Echo decorrelation imaging of rabbit liver and VX2 tumor during in vivo ultrasound ablation," Ultrasound in Medicine & Biology **43**, 176–186 (2017).

[85]M. A. Abbass, A.-J. Garbo, N. Mahalingam, J. K. Killin, and T. D. Mast, "Optimized echo decorrelation imaging feedback for bulk ultrasound ablation control," IEEE Transactions on Ultrasonics, Ferroelectrics, and Frequency Control **65**, 1743–1755 (2018).

[86]M. A. M. Abbass, "Real-time control of ultrasound thermal ablation using echo decorrelation imaging feedback," PhD thesis (University of Cincinnati, 2018), p. 181.

[87]M. A. Abbass, S. A. Ahmad, N. Mahalingam, K. S. Krothapalli, J. A. Masterson, M. B. Rao, P. G. Barthe, and T. D. Mast, "In vivo ultrasound thermal ablation control using echo decorrelation imaging in rabbit liver and VX2 tumor," PLOS ONE **14**, e0226001 (2019).

[88]J. A. Hanley and B. J. McNeil, "The meaning and use of the area under a receiver operating characteristic (ROC) curve," Radiology **143**, 29–36 (1982).

[89]A. Ghasemi and S. Zahediasl, "Normality tests for statistical analysis: a guide for non-statisticians," International Journal of Endocrinology and Metabolism **10**, 486–489 (2012).

[90]P. Mishra, C. M. Pandey, U. Singh, A. Gupta, C. Sahu, and A. Keshri, "Descriptive statistics and normality tests for statistical data," Annals of Cardiac Anaesthesia **22**, 67–72 (2019).

[91]S. Subramanian, D. T. Schmidt, M. B. Rao, and T. D. Mast, "Dependence of ultrasound echo decorrelation on local tissue temperature during ex vivo radiofrequency ablation," Physics in Medicine and Biology **61**, 2356–2371 (2016).

[92]M. A. Abbass, J. K. Killin, N. Mahalingam, F. M. Hooi, P. G. Barthe, and T. D. Mast, "Real-time spatiotemporal control of high-intensity focused ultrasound thermal ablation using echo decorrelation imaging in ex vivo bovine liver," Ultrasound in Medicine & Biology **44**, 199–213 (2018).